Capsule implosion optimization during the indirect-drive National Ignition Campaign

O. L. Landen,[1] J. Edwards,[1] S. W. Haan,[1] H. F. Robey,[1] J. Milovich,[1] B. K. Spears,[1]
S. V. Weber,[1] D. S. Clark,[1] J. D. Lindl,[1] B. J. MacGowan,[1] E. I. Moses,[1] J. Atherton,[1]
P. A. Amendt,[1] T. R. Boehly,[2] D. K. Bradley,[1] D. G. Braun,[1] D. A. Callahan,[1]
P. M. Celliers,[1] G. W. Collins,[1] E. L. Dewald,[1] L. Divol,[1] J. A. Frenje,[3] S. H. Glenzer,[1]
A. Hamza,[1] B. A. Hammel,[1] D. G. Hicks,[1] N. Hoffman,[4] N. Izumi,[1] O. S. Jones,[1]
J. D. Kilkenny,[5] R. K. Kirkwood,[1] J. L. Kline,[4] G. A. Kyrala,[4] M. M. Marinak,[1] N. Meezan,[1]
D. D. Meyerhofer,[2] P. Michel,[1] D. H. Munro,[1] R. E. Olson,[6] A. Nikroo,[5] S. P. Regan,[2]
L. J. Suter,[1] C. A. Thomas[1] and D. C. Wilson[4]

[1]*Lawrence Livermore National Laboratory, Livermore, California 94550, USA*
[2]*Laboratory for Laser Energetics, Rochester, New York, USA*
[3]*Plasma Science and Fusion Center, MIT, Cambridge, Massachusetts 02139, USA*
[4]*Los Alamos National Laboratory, Los Alamos, New Mexico, USA*
[5]*General Atomics, San Diego, California, USA*
[6]*Sandia National Laboratory, Albuquerque, New Mexico, USA*

Capsule performance optimization campaigns will be conducted at the National Ignition Facility [G. H. Miller, E. I. Moses, and C. R. Wuest, Nucl. Fusion **44,** 228 (2004)] to substantially increase the probability of ignition. The campaigns will experimentally correct for residual uncertainties in the implosion and hohlraum physics used in our radiation-hydrodynamic computational models using a variety of ignition capsule surrogates before proceeding to cryogenic-layered implosions and ignition experiments. The quantitative goals and technique options and down selections for the tuning campaigns are first explained. The computationally derived sensitivities to key laser and target parameters are compared to simple analytic models to gain further insight into the physics of the tuning techniques. The results of the validation of the tuning techniques at the OMEGA facility [J. M. Soures *et al*., Phys. Plasmas **3**, 2108 (1996)] under scaled hohlraum and capsule conditions relevant to the ignition design are shown to meet the required sensitivity and accuracy. A roll-up of all expected random and systematic uncertainties in setting the key ignition laser and target parameters due to residual measurement, calibration, cross-coupling, surrogacy, and scale-up errors has been derived that meets the required budget. Finally, we show how the tuning precision will be improved after a number of shots and iterations to meet an acceptable level of residual uncertainty. © 2011 American Institute of Physics. [doi:10.1063/1.3592170]

I. INTRODUCTION

A. Indirect-drive design

The National Ignition Facility (NIF)[1] is a 192 beam, 1.8 MJ 0.35 μm laser designed to drive inertial confinement fusion (ICF) capsules to ignition.[2] In the indirect-drive approach,[3] the laser energy is converted to thermal x-rays inside a high Z cavity (hohlraum). The x-rays then ablate the outer layers of a DT-filled capsule placed at the center of the hohlraum, causing the capsule to implode, compress, and heat the DT and ignite.

The main attributes of a representative ignition design (cryogenic hohlraum target[4] and NIF laser[5]) are shown in Fig. 1. A cm long high Z cylindrical hohlraum, currently designed with Au-lined U walls filled with 0.9 mg/cc of He tamping gas, is equipped with two laser entrance holes (LEHs) of $\approx$50%–55% the hohlraum diameter. Details of the LEH and other features of the target will be finalized to optimize performance based on the results of ongoing hohlraum energetics experiments[6] that precede the capsule tuning experiments. To provide low mode symmetry, 24 sets of beams arranged in quads of 4 beams each enter from each side in sets of 4, 4, 8, and 8 at 23.5°, 30°, 44.5°, and 50° from the hohlraum symmetry axis. The hohlraum is driven by a 1.3 MJ, 20 ns-long shaped pulse with 5 distinct phases: a 2 ns front picket to burn through the fill gas and set the initial shock, a 9 ns long trough to maintain a constant first shock velocity in the fuel, two further spikes to launch the second and third shocks, and a 4th rise to peak power for final acceleration of the shell at a peak radiation temperature T_r of 300 eV.

The current design[7] for the cryogenic capsule at hohlraum center is a graded Ge-doped[8,9] CH ablator of 918 μm inside radius and 190 μm shell thickness enclosing a 68 μm-thick layer of solid DT fuel initially held near the triple point.[10] A variety of hohlraum and capsule options[11–13] have been designed, spanning peak radiation temperatures between 270 and 310 eV, and using either Cu-doped Be,[14] Ge-doped CH,[15] or undoped or Mo-doped high density carbon[16] (HDC) capsules. A subset of these designs have a
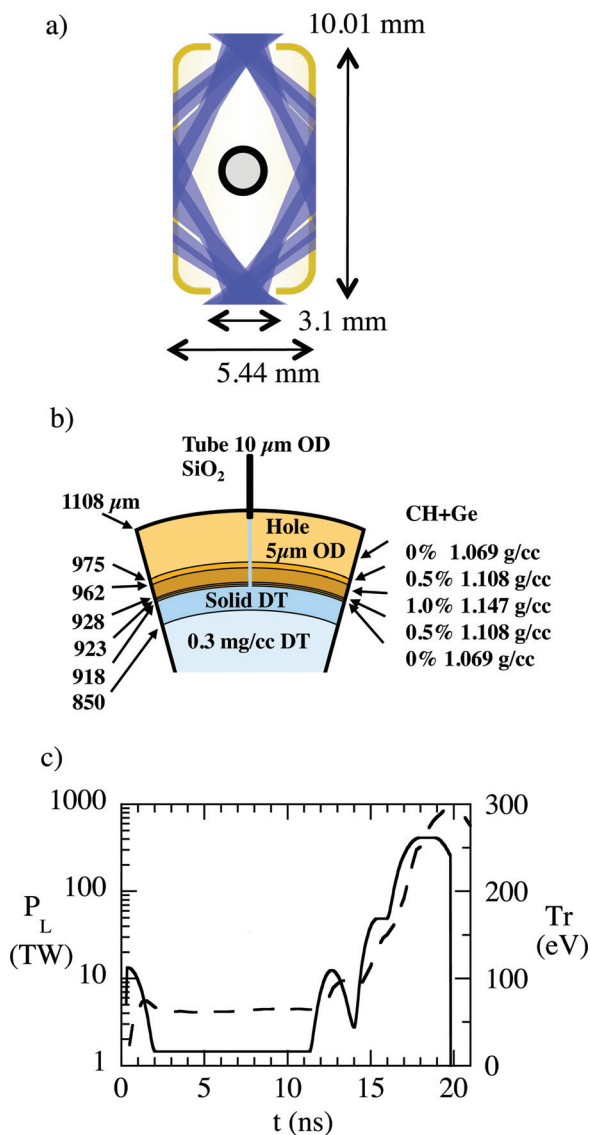
FIG. 1. (Color) (a) Schematic of the 300 eV CH indirect-drive ignition target. (b) Capsule cross-section. (c) Total laser power (solid) and radiation temperature Tr at capsule (dashed) versus time.
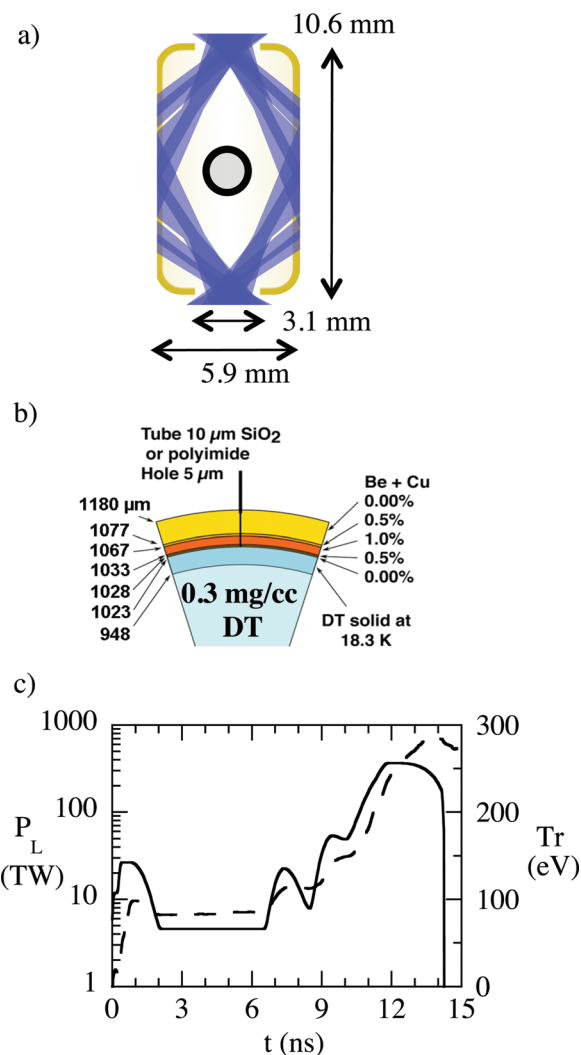

FIG. 2. (Color) (a) Schematic of the alternate 285 eV Be indirect-drive ignition target. (b) Capsule cross-section. (c) Total laser power (solid) and radiation temperature Tr at capsule (dashed) versus time.

detailed set of target and laser parameter tolerances based on 1D, 2D, and 3D[17] sensitivity simulations.[18–22] Unless otherwise noted, the tuning techniques and their required accuracy described in later sections of this paper are based on the design and sensitivity simulations for a 285 eV, 1.2 MJ graded-doped Be capsule[22] shown in Figure 2 developed during an earlier simulated campaign before the decision was made to focus on CH. Detailed sensitivity analyses for the current CH design are part of the preparations for the upcoming late 2010 campaign. In general, while the starting point target and laser parameters can vary between designs by more than the tolerable variation within a design, the sensitivity of key implosion parameters such as fuel adiabat and asymmetry to target and laser parameters variations are calculated to be similar to within a factor of 30% for both designs, within the tuning budget and simulation sensitivity uncertainty. When differences in the capsule material or laser pulseshape significantly affect details

of the tuning technique, this will be addressed on a case-by-case basis.

B. National Ignition Campaign

The first tuning campaign is preceded by hohlraum energetics campaigns to validate or change the peak Tr, hohlraum and LEH liner material, and laser spot smoothing choices. Although originally planned to initially use only the first 96 beams,[23] the energetics campaign started in 2009 is accomplishing these goals using both 83%-scale 700 kJ and full scale up to 1.3 MJ 192 beam gas-filled Au hohlraums. The campaign has so far demonstrated >90% laser-plasma absorption using backscatter[24] and near backscatter[25] optical diagnostics on a 30° and 50° beam quad, adequate (<5% peak) hot electron levels using a filter-fluorescer diagnostic,[26] peak hohlraum thermal x-ray production to at least 90% of expected using the multi-channel soft x-ray power diagnostic Dante,[27] and the ability to control imploded core symmetry diagnosed using a gated imager[28] to less than 20% out of round. These 2009 hohlraum energetics experiments

confirmed earlier 2004 20 kJ-class single-ended vacuum hohlraum x-ray drive results[29] using the first 4 beams of NIF (the NIF early light (NEL) campaign[30]). The NEL drive results in turn matched modeling validated by prior similar energy Nova[31] and OMEGA[32] facility hohlraum data[33] taken with the same type of Dante detector itself shown to agree [34] with the analogous soft x-ray power diagnostic for the LMJ facility,[35] DMX.[36] This x-ray drive consistency across facilities[37] has lent further credence to an observed improvement[38] in x-ray CE at fixed laser intensity as vacuum hohlraum scale is increased on NIF, attributed to increased volume-to-surface area ratio. Finally, gas-filled hohlraums[39,40] and tubes[41] demonstrated the efficacy of laser spot smoothing in improving radiation drive and beam propagation using phase plates,[42] polarization smoothing[43] (PS), and smoothing by spectral dispersion (SSD) for both the cases of a NIF quad geometry and the NIF-like multicone OMEGA geometry.

The overall goal of the planned capsule performance optimization campaign[44] is to empirically correct for residual uncertainties in the implosion and hohlraum physics used in our radiation-hydrodynamic computational models.[45,46] We will interleave cryogenic-layered targets[47] with the non-layered targets described below as we work toward an optimal fuel assembly before proceeding to ignition attempts. This will be accomplished using a variety of surrogate targets that will set key laser, hohlraum, and capsule parameters to maximize ignition capsule implosion velocity, while minimizing fuel adiabat, core shape asymmetry, and ablator-fuel mix. Regardless of the final scale chosen for ignition attempts (1.2–1.7 MJ), the initial tuning is planned at 1.2 MJ to reduce total laser energy requirements, representing $\approx (1.2/1.7)^{1/3} \approx 0.84$ linear scaling from a 1.7 MJ ignition design. This is followed by intentionally dudded tritium-rich but deuterium-poor cryogenically layered implosions[48] to check the efficacy of the tuning through shared observables such as core symmetry and bangtime and from implosion performance. Finally, if the chosen ignition design called for larger scale, the tuning would be checked at this scale, before proceeding to tests of alpha-heating and ignition attempts.

C. Top level tuning requirements

Extensive computational multivariable sensitivity studies[21] have shown that the probability of ignition is well correlated to five key implosion parameters: 1D peak fuel implosion velocity v, 1D burn-averaged imploded fuel adiabat α, rms asymmetry $\Delta R_{hotspot}/R_{hotspot}$ at the hotspot-main fuel interface, fraction $\Delta R_{mix}/\Delta R_{fuel}$ of fuel mixed with ablator, and a hot spot purity factor $P_{hotspot}$ to account for ^{3}He build-up due to tritium beta decay and for penetrating isolated jets of ablator material causing radiative cooling of the hotspot. The fuel adiabat is defined as the ratio of the ion + electron pressure to the electron Fermi pressure at zero temperature. As described in the companion paper by Haan et al.,[7] the product of power laws of these five parameters, for small excursions, can be used to define an ignition threshold factor (ITF) given by the following equation:

$$ITF = 5\left(\frac{v}{380 \text{ km/sec}}\right)^8 \left(\frac{\alpha}{1.46}\right)^{-4} \left(1 - 1.2\frac{\Delta R_{hotspot}}{R_{hotspot}}\right)^4$$
$$\times \left(1 - \frac{\Delta R_{mix}}{\Delta R_{fuel}}\right)^{0.5} (1 - P_{hotspot}). \tag{1}$$

The constants 380 km/s and 1.46 in the denominators are specific to a particular design (the 285 eV 1.2 MJ Be design in this case). The probability of ignition versus ITF is shown as the bold dashed line in Figure 3, where by definition, an ITF of 1 equates to 50% probability of ignition. The slope on the rise of the ignition probability curve is set by uncertainties in conduction and charged particle stopping power physics as they affect ignition and residual deviations between the ITF power law fit and individual realizations. Also shown in Figure 3 are the expected ITF distributions before tuning, after tuning with capsules having no cryogenic fuel layers (the subject of this paper), and after further tuning using cryogenically layered implosions as described in the companion paper by Edwards et al.[48] Figure 3 shows that tuning is expected to increase the mean ITF from 0.2 to 1.5. The width of the initial distribution is set by target physics model uncertainties, and the width of the intermediate and final distributions set by the quadrature sum of expected residual shot-to-shot variability in laser and target parameters and residual tuning errors.

The expected initial and final uncertainties in the first four tunable implosion parameters are given in the second and third columns in Table I. The initial uncertainties have been estimated based on a combination of level of confidence in extrapolating radiation hydrodynamics models fitting Nova, OMEGA and Z facility hohlraum energetics,[49] x-ray driven planar hydrodynamics[50,51] and gas-filled hohlraum implosion data,[40,52] and residual differences between EOS,[53,54] opacity,[55,56] and conductivity[57,58] models for the hohlraum, ablator, and DT fuel plasmas. These translate to uncertainties in the capsule ablation rate[59] affecting
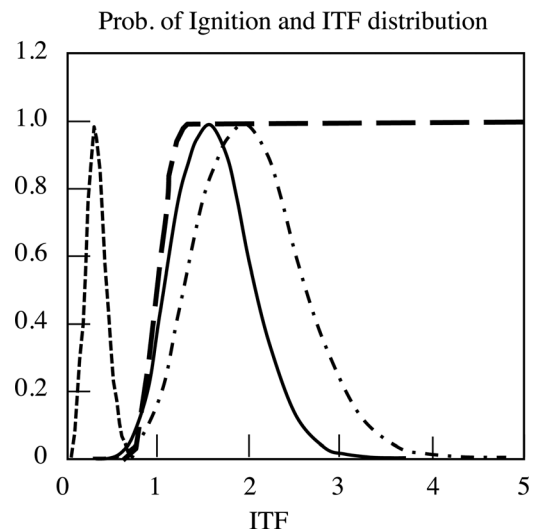

FIG. 3. Predicted probability of ignition versus ignition threshold factor (ITF) is long dashed curve. Predicted ITF distributions before and after capsule tuning experiments and after cryogenically layered capsule experiments are short dashed, solid, and dotted-dashed curves, respectively.

TABLE I. Expected initial and residual post-tune 1σ offset from optimum ignition implosion performance, associated initial and post-tune 1σ offsets in optimal laser and target parameters, and required accuracy for tuning associated observables.

Implosion offsets			Laser or target offsets			Tuning accuracy	
Parameter	Initial	Final	Parameter	Initial	Final	Observable	Value
DT fuel adiabat	+50%	+6%	1st 2 ns inner cone energy fraction	±50%	±10%	Reemit P_2 flux asymmetry	±15%
Implosion core asymmetry	50% rms	15% rms	1st 2 ns inner cone energy fraction	±50%	±10%	Reemit P_2 flux asymmetry	±15%
DT fuel adiabat	+50%	+6%	1st 2 ns laser power	±30%	±10%	1st shock velocity	±2%
DT fuel adiabat	+50%	+6%	Trough laser power	±20%	±10%	1st shock velocity	±2%
DT fuel adiabat	+50%	+6%	2nd shock laser power	±10%	±4%	2nd shock velocity	±2%
DT fuel adiabat	+50%	+6%	3rd shock laser power	±10%	±4%	3rd shock velocity	±2%
DT fuel adiabat	+50%	+6%	2nd shock launch time	±200 ps	±50 ps	2nd shock overtake point	±6 μm
DT fuel adiabat	+50%	+6%	3rd shock launch time	±200 ps	±50 ps	3rd shock overtake point	±6 μm
DT fuel adiabat	+50%	+6%	4th shock launch time	±200 ps	±100 ps	4th shock breakout time	±100 ps
DT fuel adiabat	+50%	+6%	4th rise duration	±200 ps	±100 ps	4th rise Tr slope to peak power	±5%
Ablator mass remaining	±80%	±25%	Initial ablator thickness	±30 μm	±10 μm	Symcap mass remaining	±13%
Peak implosion velocity	±10%	±2%	Peak laser power	±20%	±4%	Velocity at r = 300 μm	±2%
Peak implosion velocity	±10%	±2%	Peak laser power	±20%	±4%	Symcap bangtime	±50 ps
Implosion core asymmetry	50% rms	16% rms	Peak inner cone energy fraction	±20%	±5%	Symcap P_2 core asymmetry	±7.5%
Implosion core asymmetry	50% rms	16% rms	Hohlraum length	±400 μm	±200 μm	Symcap P_4 core asymmetry	±7.5%
Ablator-fuel mix	±40%	±15%	Mid-Z ablator dopant fraction	±0.5%	±0.1%	2−5 keV x-rays in hohlraum	±10%

implosion velocities and to uncertainties in the hohlraum x-ray conversion efficiency,[60] albedo,[61,62] and radiation hydrodynamics[63] affecting drive symmetry. They also translate to uncertainties in the hard x-ray preheat levels,[64] ablator compressibility and dopant opacity affecting fuel adiabats through shock transit time mismatches,[65,66] and affecting the level of ablator-fuel mix[67] through a non-zero ablator-fuel interface Atwood number.[68]

The tuning campaign is based on the principal that these physics uncertainties can be empirically corrected for by adjusting key laser and target parameters around their nominal values, thereby increasing the ITF by increasing implosion velocity and lowering fuel adiabat, asymmetry, and mix. Fourteen principal adjustable parameters have been

FIG. 4. (Color) Schematic of 14 laser and target parameters varied.

identified, shown schematically in Figure 4, and listed in the fourth column in Table I alongside the implosion parameters they affect. For the laser, they are the power levels for the 5 phases in the laser pulse, the launch time for the second, third, and fourth steps, the end-point in the 4th rise of laser power (when the pulse first reaches peak power), and the power balance between inner and outer cones during the first and last phase. For the target, there are three parameters; the hohlraum length, capsule ablator thickness for fixed inside diameter, and capsule ablator mid-Z dopant fraction. The fifth and sixth columns show the expected initial and final 1σ uncertainties in setting these parameters that are consistent with the uncertainties quoted for the four implosion parameters. From Figure 4, it is clear that we have chosen not to vary (at least initially) some apparently equally fundamental laser and target parameters, such as the inner cone fraction during the trough, second and third pulse, and the radii of the hohlraum and capsule. The reasons are as follows. First, simulations show that we expect the contribution to the core asymmetry to remain below 5% rms (well below the <10% rms requirement) for a maximum plausible uncertainty of ±25% in setting the optimum inner cone fraction during the second and third shock phase. Second, the symmetry of the trough is expected to mimic the tuned symmetry of the first 2 ns by virtue of the quiescent conditions in the trough consisting of nearly constant laser power and high albedo. Third, the ratio of the hohlraum to capsule radius is set to minimize the geometric transfer of any hohlraum drive P_4 asymmetry component onto the capsule.[3] Hence, varying the hohlraum radius to change the illumination pattern at the hohlraum wall would require also varying the capsule radius that in turn would strongly change (up to cubic depedence on radius) the energy coupled to the capsule. The P_4 asymmetry can be minimized in a more non-intrusive fashion (i.e., at the wall) by optimum choice of the laser pointing and the hohlraum length.
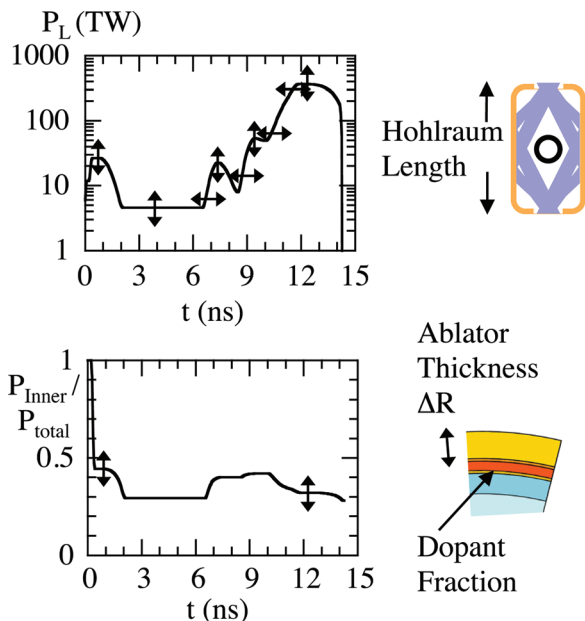
To adjust these key laser and target parameters by experimentation so as to optimize the implosion performance, we have chosen a set of non-igniting tuning shots equipped with a set of clear observables. Section II will discuss the goals, observables, expected accuracy, and experimental demonstrations of the tuning techniques. Section III will present the goals and sequencing of the tuning shots and briefly discuss further experimental techniques for isolating capsule physics issues if required based on early implosion results. Section IV will summarize the tuning accuracy, and a more detailed appendix on the tuning accuracy breakdown is included.

II. TUNING TECHNIQUES

Extensive sets of shots were completed at the Nova and OMEGA facility to demonstrate and downselect among proposed tuning techniques. The mainline tuning targets chosen are the high Z re-emission spheres[69] setting the foot cone power balance from the observed foot drive symmetry, liquid D_2-filled "keyhole" targets setting the laser power profile up to peak power from the observed shock speeds and overtake distances and times,[70] x-ray imaged imploded capsules setting the peak cone power balance and hohlraum length from observed core symmetry,[71] and streaked or gated x-ray backlit imploding capsules[72] setting the initial ablator thickness and peak laser power from the radiographically inferred ablator mass remaining[73] and implosion velocity. In addition, the Dante diagnostic will be used to set the 4th rise launch time from the 4th rise slope and to set the ablator dopant fraction from the measured hard (>1.8 keV) x-ray preheat levels. For the rest of this section, we will be discussing pulse-shapes and tuning targets appropriate for the full 1.2 MJ, 285 eV Be design scale. Unless otherwise stated, all uncertainties and errors are 1σ values assuming Gaussian distributions. The tuning accuracy requirements have been balanced in terms of their contribution to the uncertainty in mean ITF (typically set at $\pm10\%$ per term) which is referred back to in each section.

A. Drive symmetry in the first 2 ns

1. Physics basis for requirements

The NIF cylindrical hohlraum ignition design has chosen inner ($23.5°$ and $30°$) and outer cone angles ($44.5°$ and $50°$) with respect to the hohlraum axis such that the centroids of these beams pass near the center of the LEH at optimum hohlraum length and initially point at hohlraum wall positions $\approx$ subtending $\theta = 90°$ and $40°$ to the hohlraum center, representing the nodes of P_3. Hence, for an appropriate choice of inner to outer power ratio, one can simultaneously zero P_2 and P_4 (and all odd moments) at a particular value of wall albedo. Ensuring spherical symmetry of the first shock launch is important for two reasons. First, simulations show that for an initial plausible 12% P_2 incident flux asymmetry averaged over the first 2 ns, the final ignition core asymmetry could be outside the requirement of $<10\%$ rms. This level of flux asymmetry can be related to an uncertainty in setting the first 2 ns inner versus outer cone energy ratio. Defining the fraction of energy in the inner cone as CF, the change in P_2 around zero

at the capsule due to change in inner cone fraction is given by $0.5 \times 2P_2(90°)(\Delta CF/CF)/(F+1)$. The factor 2 accounts for inner and outer cones contributing equally (i.e., neglecting small residual P_2 from LEH) but of opposite sign to P_2 when P_2 about zero, and the factor 0.5 accounts for the geometric radiation transfer factor, diluted by the ratio of recirculating to spot flux[3] $F = \alpha/[(1-\alpha) + (\Omega_{LEH} + \Omega_{Caps})/\Omega_W]$. So a 12% incident P_2/P_0 for $F = 1$ given an average albedo $\alpha = 0.6$ over the first 2 ns corresponds to an initial cone fraction uncertainty $\Delta CF/CF = 50\%$, as listed in Table I. Second, since shock timing is performed as a single point measurement (at the capsule equator, $\theta = 90°$, see Sec. B), one must ensure that the measured first shock strength that sets 90% of the final compressed fuel adiabat is representative of the solid angle averaged first shock strength. In the presence of an x% P_n flux asymmetry, the offset from optimum in the solid-angle averaged first shock pressure after setting the optimum shock pressure over a narrow range of angles $90 \pm \Delta\theta$ is given by

$$\Delta P = (7/8) \int x[P_n(\theta) - P_n(90 \pm \Delta\theta)] \sin\theta d\theta / \int \sin\theta d\theta,$$

(2)

where the 7/8 factor accounts for the relationship between shock pressure and drive flux[3] and $P_n(90 \pm \Delta\theta)$ is the average value of the P_n Legendre mode over polar angles $90 \pm \Delta\theta$. So, for $\Delta\theta = \pm4°$ characteristic of the "keyhole" shock timing geometry described in Sec. B, $\Delta P = 0.44x$ and $-0.33x$ for a pure x% P_2 and P_4 asymmetry, respectively. Hence, for a plausible $x = 12\%$ initial P_2 drive asymmetry, the solid-angle averaged first shock pressure offset ΔP would be 5.3%, corresponding to a $+3\%$ increase in solid-angle averaged fuel adiabat,[7] hence a significant 12% reduction in ITF per Eq. (1). The preceding discussion ignored intrinsic azimuthal asymmetries; the plausible maximum first shock pressure offset at the capsule in the presence of an m = 4 drive asymmetry at the equator due to differences in x-ray conversion efficiency between the $23.5°$ and $30°$ subcones is a negligible 2%. Finally, while the trough drive from 2 to 6 ns will be shown in Sec. B to play an even more important role in setting the first shock velocity transiting the fuel at 8–12 ns, as mentioned earlier, the expected symmetry in the trough should change little from its measured initial state at 2 ns. Based on these two considerations, the goal is to set the first 2 ns P_2 and P_4 drive asymmetry to $0\% \pm 5\%$ and 7%, respectively.

2. Tuning technique

Since a 5% P_2 flux asymmetry over the first 2 ns would only lead to a few % ignition core asymmetry that could be masked or mistaken for other asymmetries later in the pulse, we needed a different technique to isolate the first shock asymmetry. Two of the candidates, thin capsules that implode early[74] and backlit thinshells[75] that integrate the drive over shorter periods of time were successfully tested and evaluated at OMEGA at 70% NIC-scale. Both have calculated undesirable heightened hydroinstability and shape distortion sensitivity to thickness non-uniformities since

ensuring a relevant few ns bangtime requires starting with a much thinner 10-μm-shell. The backlit thinshell symmetry is recorded earlier in its trajectory (typically having imploded 1/3 to 1/2 of its initial radius) that still allows for a sufficiently accurate measurement of the asymmetry due to having more spatial resolution elements around its larger circumference. However, both techniques only sense an average asymmetry over a time period when the P_2 asymmetry is varying strongly due to increasing hohlraum albedo and when it is most sensitive to uncertainties in differential hohlraum gas burnthrough rates of inner versus outer beam cones. Moreover both have a strong time-dependent symmetry sensitivity, being most sensitive at the onset of acceleration[75] (at typical 0.5 ns break-out times for 20 μm/ns shock speeds), and their trajectories and hence geometric smoothing factors deviate after that compared to the much thicker, higher inertia ignition capsule. Both techniques remain back-up options for studying the symmetry during the first 2 ns and primary options if we need to isolate the asymmetry between the first 2 ns and the peak of the drive.

To record the instantaneous asymmetry during the first shock launch time (the first 2 ns), we have chosen to take multiple images in time of the soft x-ray reemission from a non-imploding Bi ball replacing the ignition capsule. Since the ignition capsule radius only shrinks from shock compression by $\approx 2/(\gamma+1) \times 20~\mu$m/ns $\times 2$ ns $\approx 30~\mu$m out of 1 mm during the first 2 ns (for a specific heat ratio $\gamma = 5/3$ and a first shock design velocity of $\approx 20~\mu$m/ns), the geometric drive symmetry smoothing factor between hohlraum and sphere vs ignition capsule remain similar to a few %. Simulations have shown that the hohlraum gas-fill environment through which the beams are traversing is not affected for the required 2 ns by having Bi rather than ignition capsule ablation. Each point on the Bi sphere is locally radiatively heated, and the local re-emission flux is a measure of the local incident flux. Bi is chosen as it is a higher Z material than the Au hohlraum wall that the beams interact with during the foot, mitigating fluorescence concerns. In practice, the re-emission from the ball limb is imaged through a diagnostic hole or LEH, providing an instantaneous measure of
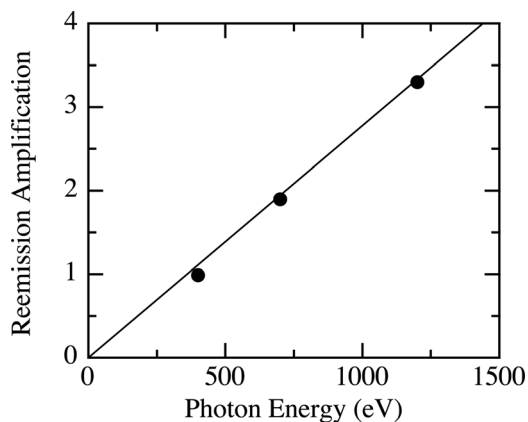
the flux incident on the ball vs. polar or azimuthal angle, respectively. After 2 ns, the Bi ablation smears out the limb and reduces accuracy. The accuracy of the flux asymmetry measurement is enhanced by choosing a re-emission photon energy $h\nu$ that is many times the thermal reemission temperature kT_{re} of the Bi sphere of albedo α_{Re}, where $T_{re} = \alpha_{re}^{1/4} T_r$. Specifically, in the limit of Planckian sources, an n% incident flux asymmetry should result in an $n \times (h\nu/4kT_{re})$% re-emission flux asymmetry. Figure 5 shows that the calculated asymmetry amplification factor at various reemission photon energies using a more realistic incident drive spectrum (corresponding to Tr = 97 eV at t = 3 ns, hence $T_{re} = 97\alpha^{1/4} = 90$ eV for calculated albedo $\alpha = 0.75$) also matches closely the analytic Planckian $h\nu/4kT_{re}$ formula. There is a practical limit however to the maximum usable $h\nu$ as the re-emission flux falls off exponentially with photon energy.

The first reemission experiments at Nova diagnosed early time symmetry at higher temperature drives (Tr = 100–200 eV) using 2 keV reemitted x-rays,[69] corresponding to values of $h\nu/4kT_{re} = 4$–8. Subsequently, viable reemission designs for measuring the foot symmetry of various 1 MJ ignition designs were documented.[76] Figure 6 shows the planned experimental set-up for the NIC tuning and the starting point truncated pulse powers for the first 2 ns. A $2\times$ magnification, 50 μm-resolution, 200 ps gated pinhole
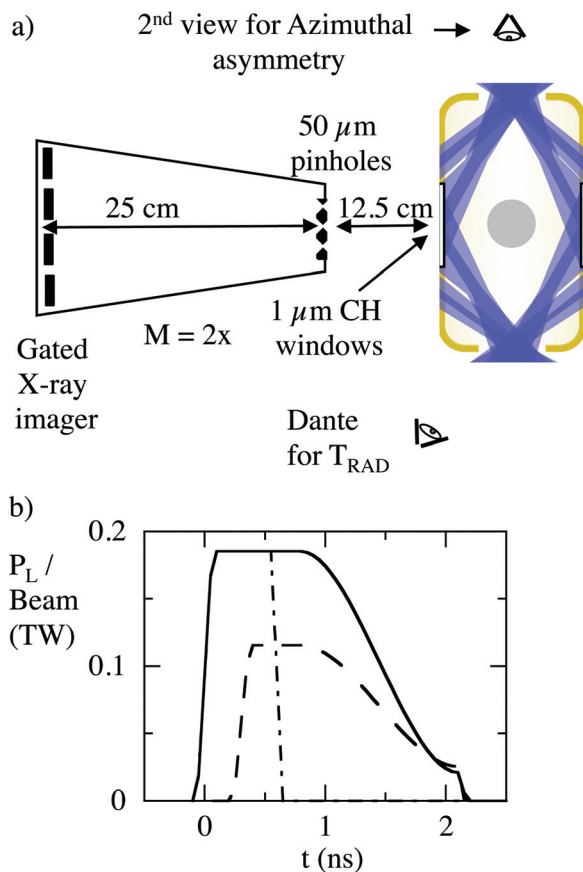
FIG. 6. (Color) (a) Re-emission sphere experimental set-up for NIF shots. (b) Power per beam for 48 inner cone beams (solid), 128 outer cone beams (dashed), and for 16 inner cone beams that would hit patches (dotted-dashed).

FIG. 5. Ratio of reemitted P_2/P_0 asymmetry at 400, 700, and 1200 eV photon energies to incident spectrally integrated P_2/P_0 asymmetry 3 ns into a calculated drive equivalent to a 97 eV Planckian. Solid line is analytic Planckian prediction.

imager with thin high-pass filtering (e.g., 6 μm of Al) appropriate for >900 eV x-rays is used. The spatial resolution is set by balancing providing sufficient signal throughput with avoiding too much radial smearing of the limb profile. No grazing incidence x-ray mirrors for better spectral definition[77] are planned since they would cut down signal significantly, and we expect the natural drop in the Planckian flux from the Bi sphere to provide the cut-off on the high energy side. The combination of filters and the Planckian spectrum leads to a 300–400 eV bandpass. Up to 16 images are recorded, in 4 adjustable time periods, with the possibility of recording at 2 different values of hν on the same shot for crosschecks of the reemission sensitivity.

Of note are the large 2.7 mm diameter low Z patches required to view the soft x-rays from the Bi sphere along the hohlraum equator and to avoid high Z background wall emission blending with the Bi limb emission. The patch sizes are chosen as 0.7 mm larger than the 2 mm reemission sphere to allow for 200 μm of view on all sides of the reemission sphere from all pinhole views subtending up to $\pm$50 mrad of parallax. To avoid adding further hohlraum background emission, the 4 inner 30° quads that would fully hit the patches are turned off [see Figure 6(b)] after they burn through the gas-fill (to maintain fidelity as long as possible for the laser heating at the gas-fill near the LEH where all beams cross) but before or soon after they reach the patches. The combination of having 25% of the inner beams turned off and the low Z patches leads to a deficit of drive at the equator and hence a positive P_2 offset at the reemission sphere compared to the ignition capsule. This is partially cancelled by the higher albedo of the reemission sphere that preferentially heats the more proximate equatorial wall regions.

3. Calculated sensitivity and accuracy

Figure 7 compares 3D Hydra[46] calculations including all the above-mentioned differences between the incident P_2/P_0 flux inferred from a reemission sphere and the incident P_2/P_0 flux on an ignition capsule averaged over the first 2 ns as a function of inner cone fraction. We note that the surro-
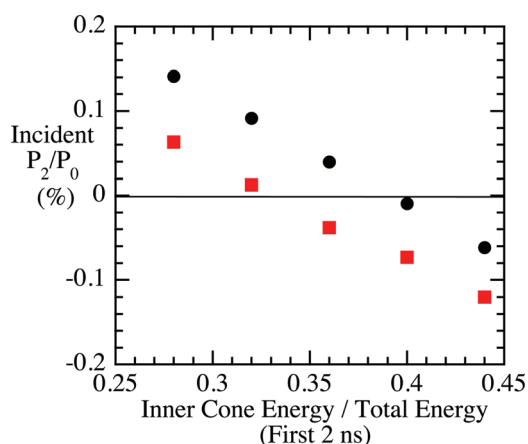

FIG. 7. (Color online) Calculated incident P_2/P_0 integrated over 1st 2 ns for re-emission sphere (black circles) versus ignition capsule (red squares) as a function of inner cone energy fraction.

gacy offset in P_2 is relatively small, +8%, because the view-factor[78] between the patch areas and the Bi sphere limb from which the equatorial view data is extracted is small. The error in this offset is estimated based on 10% uncertainties in 100 eV low[55] Z and high[61] Z albedoes at $\pm$2%, well within the requirement to tune to $\pm$5% in P_2. Moreover, a second identical imager viewing down the pole will check the azimuthal asymmetry expected from missing inner beams and patches. The starting point optimum reemission P_2/P_0 is hence = +24% $\pm$ 15% based on multiplying the +8% incident P_2/P_0 offset shown in Figure 7 and the required accuracy of $\pm$5% by the design asymmetry amplification value of hν/4kT_{re} = 3. This $\pm$15% required accuracy in the observable, accounting for all target, laser, and tuning systematic and random imperfections and errors, is listed in the last column in Table I. If the measured reemission P_2/P_0 on the first shot were outside these limits, we would vary the inner versus outer laser cone fraction while keeping the total power fixed by an amount set by the slope of Figure 7 to reach the offset goal of +24% reemission P_2/P_0. Further shots would be required if the Figure 7 slope were found to be sufficiently different than expected or if we found more scatter in the data than expected. The expected data scatter from existing 10% random shot-to-shot laser power imbalances among quads during the first 2 ns of the drive on the foot symmetry has been quantified using 3D Hydra simulations. The rms variation in the inferred incident P_2/P_0 along the reemission line-of-sight extracted from several 3D simulations with different realizations of this level of power imbalance is $\pm$2.4%, well below the $\pm$5% tuning requirement.

While the gated reemission sphere technique records P_n/P_0 averaged over 200 ps at 4 separate times on any given shot, we ultimately require control of P_2/P_0 averaged over 2 ns. Figure 2(c) shows that the P_0 drive varies strongly over the first 2 ns. Calculations show that the drive below 10% of the local maximum at 1.5 ns would not be visible for any practical measurement at hν > 600 eV. Fortunately, time-dependent simulations assuming a variety of cone fractions show that the P_2 asymmetry component seeded by the <10% P_0 drive phase is only 1%, well below the required tuning accuracy. At later times, we can use either or both the relative brightness of the reemission images to weight each image P_2/P_0 properly, or the soft x-ray foot drive measured through the LEH using the calibrated[79] Dante and correcting for unconverted light plasma emission.[80] For realistic 10% errors in relative P_0 between frames (due to residual uncertainties in relative gains between the gated camera MCP microstrips, reemission albedo, and pinhole sizes) and including the effect of a finite number of sampling times, we calculate that these sampling errors in inferring the incident time-integrated P_2 are no more than $\pm$2% for a realistic range of P_2 swings in time. Should target shrapnel and debris[81] prove to be too much of a threat to the fragile microchannel-plates in gated imagers, then the fallback option is to switch to time-integrating Image Plate[82] detection using Fuji BAS TR plates sensitive to soft x-rays.

The uncertainty in the Planckian approximation for the asymmetry amplification factor hν/4kT_{re} must be taken into account since we are tuning the drive on the reemission

sphere to an offset P_2 to ensure symmetry at the ignition capsule. To estimate this error, we use the 40% difference between calculated versus measured relative sensitivities of the reemission asymmetry [see later Figure 9(a)] at two different reemission photon energies, 900 and 1200 eV. Hence, a 5% P_2 offset with such a $\pm 20\%$ amplification uncertainty leads to a 1% P_2 uncertainty. Finally, we have considered the reemission technique as applied to the CH capsule ignition designs that use a lower temperature foot drive [per Fig. 1(c), 75 instead of 95 eV] since they do not need to ensure melting of a polycrystalline ablator[51] during the foot. The plan is to use a softer channel with its centroid at about 700 eV requiring thinner filtering (2.5 μm Al) to maintain the same signal levels and amplification factors $h\nu/4kT_{re}$.

4. Experimental validation of technique

Figure 8(a) shows a schematic of the experimental set-up at OMEGA used to validate the technique at NIC-relevant scale and Tr. Nearly identical diagnostic distances and parameters were used as for the planned NIC set-up. Also shown is an example of a $2 \times$ magnification, 100 μm by 70 ps resolution re-emission image at t = 0.7 ns, $h\nu = 900$ eV from a 1.4-mm diameter Bi sphere sampling a 100 eV, 1 ns drive in a 6.4-mm-long by 3.6-mm-diameter vacuum hohlraum irradiated by 21.4° and 59° OMEGA beams.[83] Figure 8(b) shows an example of the measured reemitted P_2 asymmetry versus time at $h\nu = 900$ eV for an inner cone

fraction = 0.12. P_2 decreases in time as the hohlraum heats up because the negative P_2 from the cold LEH becomes relatively more prominent as the Au wall albedo increases in time. Also shown are two 3D Hydra post-shot simulations that match the trend, the upper curve showing the effect of an assumed 10% reduction in the inner cone coupling. Figure 9(a) plots the extracted P_2 reemission asymmetry at t = 0.7 ns as a function of imposed inner cone fraction for both 900 and 1200 eV channels. It shows that both data and the four postshot 3D Hydra simulations connected by lines agree on the expected decrease in P_2 with increased inner beam fraction, higher sensitivity at the higher photon energy, and consistency between channels for the cone fraction of best symmetry. Since $h\nu/4kT_{re} \approx 3$ at 1200 eV, the typical $\pm 6\%$ P_2 reemission asymmetry error bar shown in Fig. 9 translates to $\pm 2\%$ accuracy in inferred instantaneous incident P_2 asymmetry. This accuracy is consistent with estimates based on shot noise and frame-to-frame variability and is well under the $\pm 5\%$ requirement. Figure 9(b) compares a reemit image at later times (t = 1 ns) vs simulations, in this case for the 1200 eV channel at an inner cone fraction = 0.12. We note the localized emission spike at the equator ($\theta = 90°$) not predicted by simulations where the thin (≈ 0.5 μm) polyimide sheets stretched between hohlraum halves that hold the reemission sphere in place leave a gap. Recent experiments successfully eliminated this equatorial non-uniformity by mounting the reemission sphere using a thin stalk rather than polyimide sheets. They also extended the technique to near full-scale (2.1 mm Bi ball in a 9 mm by 5 mm hohlraum)[84] and demonstrated the required accuracy for also inferring P_4/P_0.
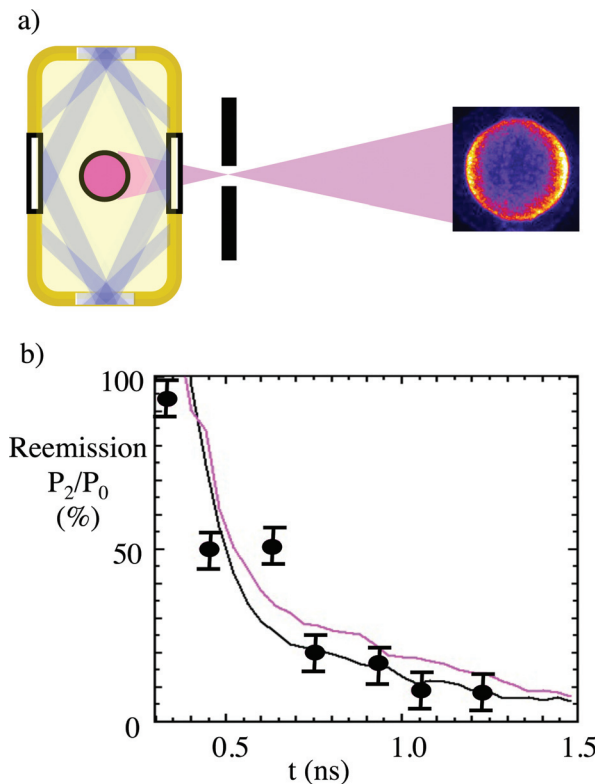
a)

b)

FIG. 8. (Color) (a) Re-emission sphere experimental set-up with example OMEGA data. (b) Instantaneous P_2/P_0 x-ray emission data at 900 eV for inner cone fraction = 0.12 from 1.4 mm diameter re-emission sphere using 6.4 mm long hohlraums and 100 eV peak drive. Solid curves are postprocessed results from 3D Hydra simulations assuming full coupling (black) and 90% coupling on the inner cone (purple).
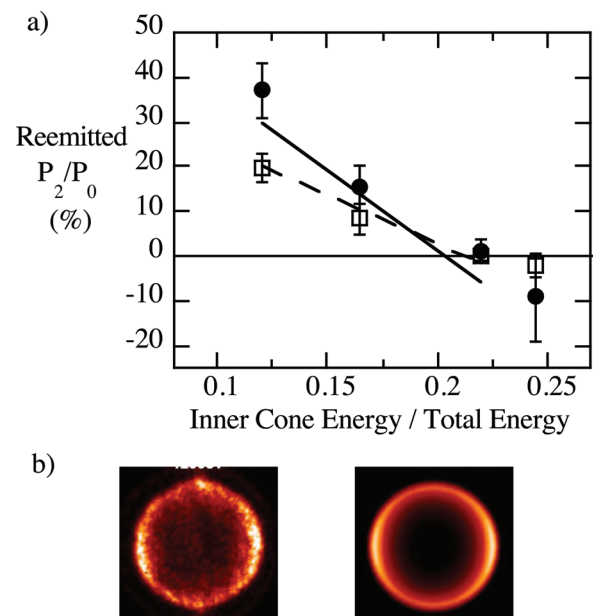
a)

b)

FIG. 9. (Color) (a) P_2/P_0 of 900 eV (open squares) and 1200 eV (closed circles) x-ray emission from 1.4 mm diameter re-emission sphere versus inner cone fraction at 0.7 ns using 6.4 mm long hohlraums and 100 eV drive. Solid and dashed lines are postprocessed results from 3D Hydra simulations for 1200 and 900 eV channels, respectively. (b) Comparison of measured vs calculated reemission sphere image at 1200 eV for inner cone fraction = 0.12 at t = 1 ns.

B. Timing and strength of first 3 shocks

1. Physics basis for requirements

Ignition requires a pulse shape with a low power foot designed to send a carefully timed series of shocks through the frozen DT shell such that they overtake each other soon after they travel into the enclosed DT gas. If the shocks are too closely spaced, they will coalesce within the DT ice leading to an increase in the adiabat (or entropy, $\sim \alpha^{0.4}$ for small ($<50\%$) excursions in adiabat) at the inside surface of the DT ice, reducing compressibility. If they are too widely spaced, the DT ice decompresses between shocks. Unless the first 3 shocks are spaced correctly (at the level of ± 50 ps when including all other sources of error and imperfections), the DT will fail to reach the required high fuel ρr at the end of the implosion. Since typical uncertainties in ablator and DT compressibility are at least 5%, even for those with measured first shock Hugoniots, the uncertainties in transit times of successive shocks scaling as $1/\sqrt{\rho}$ can be expected to be at least $\pm 2.5\%$ out of typical 4 ns transit times, hence $> \pm 100$ ps, with ± 200 ps quoted in Table I.

As discussed in Sec. A, setting the time-dependent strength of the first shock in the fuel (to 10% in pressure, 5% in shock velocity as the first shock traverses the fuel) is also important in setting 90% of the final fuel adiabat. This is achieved by using an independently adjustable first picket followed by a trough as shown in Fig. 1(c) or 2(c). In addition, the first shock pressure in the ablator must be kept high enough ($>2.6 \pm 0.1$ Mbar to promote complete melting)[85] in the case of polycrystalline Be. We note that the 5% uncertainty in the melt pressure and uncertainty in the shock steadiness across the ablator are consistent with setting a minimum first shock velocity to within 5% from fuel adiabat considerations. For the case of the lower melt point CH ablator, the first shock pressure is designed to be $\approx 2\times$ lower (≈ 1.5 Mbar), leading to a 15% lower first shock velocity and hence longer foot phase.

For the second and third shocks, a range[3] of launch times and compensating shock strengths can provide the optimum overtake distance[86] (a few μms inside of the DT solid–gas interface) with a small effect on the final adiabat. The ratios of shock pressures and hence velocities are constrained to avoid large entropy jumps between successive shocks without resorting to adding more intermediate shocks.[3] The initial uncertainties of 30%, 20%, 10%, and 10% in relating laser power to imposed shock pressure for the first shock, trough, second, and third shock in Table I are based on combining estimated uncertainties in hohlraum window and gas burnthrough energetics to existing 10%–15% albedo[61] Dante flux accuracies[79] at these low drive temperatures.

Based on these considerations, the goals listed in the final column of Table I are to set the first shock velocity to within 5% of its design value[22] near 20 μm/ns and to set the overtake point for the second and third shocks to within ± 6 μm of its design distance of about 10 μm past the DT fuel-gas interface. The latter goal will be accomplished by a combination of ensuting the repeatability of the 1st shock velocity to $\pm 2\%$, setting the second and third shock launch times to ± 50 ps, and setting their velocities after overtaking the prior shocks to $\pm 2\%$ of their design values near 37 and 60 μm/ns, respectively.

2. Tuning technique

Since radiographic methods of assessing shock front velocities to these accuracies would require unrealistic sub-μm accuracy after accounting for the fuel compression that occurs after each shock passage, we opted for a direct continuous measurement of the shock velocity. We achieve this by reflecting off the shock front[87] using a streaked 1D imaging laser-based interferometry system,[88] commonly known as VISAR, from which shock front velocities are extracted from fringe shifts and overtake distances extracted by integrating the velocity between the time of first shock break-out from the ablator-fuel interface and time of next shock overtake seen as a sudden jump in fringe shift. The initial design[86] proposed a planar liquid D_2 cell sandwiched between the ablator and a transparent quartz window and placed on the side of the hohlraum to approximately mimic the DT ice drive conditions inside a capsule at the center of the hohlraum. Since then, with the realization that a 1 mm radius capsule provides an adequately large (>100 μm diameter) reflecting surface collected by the f/3 optics of the VISAR, the experimental design has evolved to using a liquid D_2-filled Au cone reentrant inside the capsule, greatly increasing the fidelity[89] of the drive conditions.

A schematic of the experimental geometry is shown in Figure 10(a) with a simulated 659 nm VISAR streak showing the abrupt fringe shifts expected upon first shock breakout into the liquid D_2 and from the second shock overtaking it a few ns later. The re-entrant cone is made of Au to reduce its wall losses and kept sufficiently thick (100 μm) to avoid side shock breakout into the D_2 adding background self-emission. The tip of the cone is slightly oversized to allow for a reflecting endcap that will provide a spatial and intensity fiducial. The total return field-of-view will be 200 μm, magnified by $15\times$ onto two optical streak cameras.[90] The two cameras allow the VISAR to be run with simultaneous high and low sensitivity channels with non-commensurate values of ≈ 3.1 and 1.2 fringe shift/20 μm/ns to extract unique solutions to the velocities with high accuracy.

The tuning strategy is to first set the velocity of the first shock by adjusting the total power in the first pulse and in the trough, and then the overtake distance and coalesced second shock velocity by adjusting the second launch time and second pulse total power. Figure 10(b) shows the starting point laser powers for inner and outer cones, truncated to reduce laser fluence, debris energy and to avoid blanking of optics and windows by the much higher x-ray fluences from the peak of the pulse. The truncation strategy is based on simulations that show that any prompt preheat from the 4th pulse that would normally be present will have minimal effect on the transit times of earlier shocks at the accuracy required. Of note, the third pulse has been intentionally delayed by 1 ns to ensure the second shock velocity can be measured after it overtakes the first shock but before it is overtaken by the third shock. Figure 10(c) represents a simulated analyzed VISAR trace showing the three jumps in the
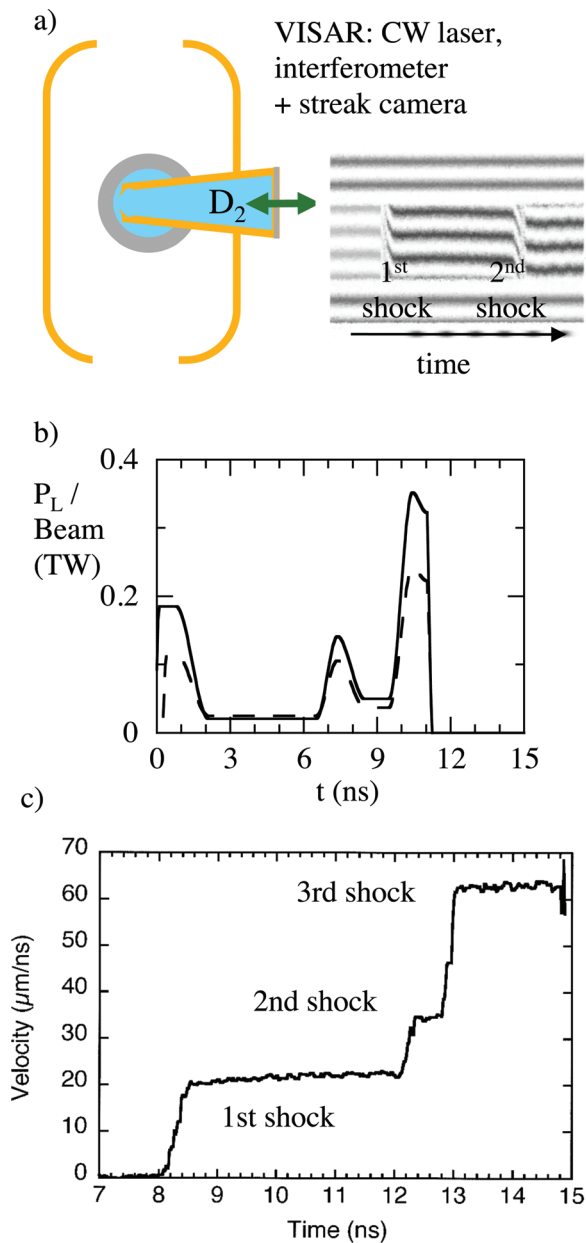
FIG. 10. (Color) (a) 1st three shock tuning experimental set-up for NIF shots and simulated VISAR fringe data. (b) Power per beam for 64 inner cone beams (solid), 128 outer cone beams (dashed). (c) Simulated output of leading shock velocity versus time that might be expected with third shock delayed intentionally.

leading shock velocity that might be expected in such a case. We have the option of truncating after the second pulse to reduce total fluence and debris. The final step is to bring the third shock forward at the correct strength by adjusting third pulse total power and launch time so all shocks coalesce at same time and place.

3. Calculated sensitivity

Figure 11 plots the radial derivative in the pressure in initial Lagrangian coordinates versus time to highlight the shock front trajectories. Figure 11 shows that the calculated tuned shock trajectories in liquid D_2 vs solid DT (scaled to the same size design) are well matched, with no more than a
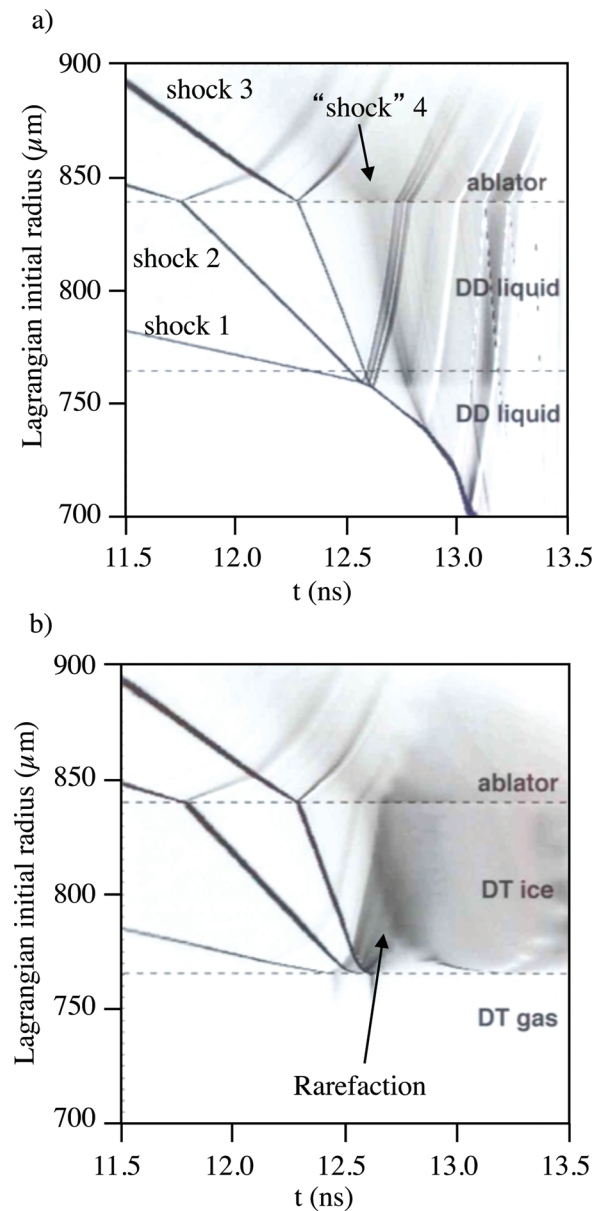

FIG. 11. (Color online) Calculated late time shock trajectories in ablator and fuel in initial Lagrangian coordinates for (a) surrogate capsule filled with liquid D_2 and (b) ignition capsule with DT solid and gas.

known 100 ps timing offset for the first shock. Because the shocks are designed to coalesce within a few μms of entering the DT gas, the rarefaction occurring at the solid–gas DT interface but absent in the liquid D_2 surrogate has insufficient time (<200 ps) to necessitate a correction of the offset in the desired coalescence point. The points in Figure 12 show three examples of the calculated sensitivity among key observables (the first and second shock velocity in the fuel and second shock overtake distance) and adjustable laser parameters (the trough power, and second pulse laser power P_L and launch time). By contrast, the laser power in the first pulse primarily sets the first shock velocity in the ablator, for which the observable is the shock breakout time into the D_2.

The calculated points of Figure 12 are fairly well matched by simple analytic scalings shown as the lines and described below. To a good approximation, the shock
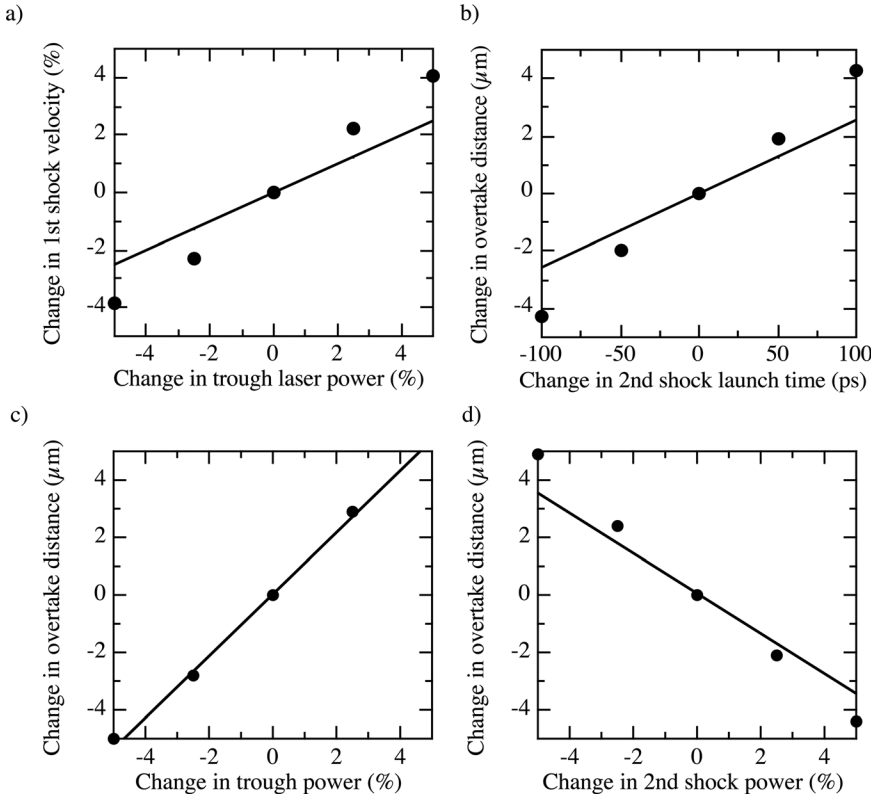
a)

b)

FIG. 12. Computed (symbols) and analytic (line) (a) change in first shock velocity versus change in power in trough of NIC pulse, (b) change in second shock overtake distance versus change in second shock launch time, (c) change in second shock overtake distance versus change in trough laser power, and (d) change in second shock overtake distance versus change in second shock laser power.

velocities in Figure 12(a) scale as $\sqrt{P_L}$, hence laser powers have to be set to $\pm 4\%$ repeatability to meet the $\pm 2\%$ shock velocity requirements as listed in Table I, well within the demonstrated capabilities of the NIF laser.[5] The overtake times and distances depend on both the relative and absolute shock velocities. The trough and second pulse ablation rates (per T_r^3 scaling[3] and Figure 2(c), calculable as <4 μm/ns in the initial uncompressed Lagrangian reference frame) can be neglected compared to the second and third shock velocities in the ablator [33 and 45 μm/ns in the same reference frame per Figure 11(a)]. For an nth shock, the change in either overtake time $\Delta\tau$ or overtake distance Δx as a function of change in shock launch time Δt_n or Δt_{n-1} is then given by simple kinematics as:

$$\Delta\tau = [c_n/(c_n - 1)]\Delta t_n \text{ and } \Delta x = u_{n-1}\Delta\tau, \quad (3a)$$

$$\Delta\tau = -[1/(c_n - 1)]\Delta t_{n-1} \text{ and } \Delta x = u_n\Delta\tau, \quad (3b)$$

where c_n is the ratio of the overtaking u_n to overtaken shock velocity u_{n-1} in the D_2. Extracting these velocity ratios from Figure 11(a) and other such detuned plots in the initial Lagrangian reference frame, $c_2 = 100/20 = 5$, and depending on whether the 3rd shock overtakes the second shock or the coalesced second shock, $c_3 = 240/100 = 2.4$ or $150/37 = 4$. Equations (3a) and (3b) represent sensitivity for changes in overtaking and overtaken shock launch time, respectively. As expected, a comparison of Eqs. (3a) and (3b) shows that delaying the nth trailing shock is equivalent to advancing the nth–1 leading shock (by setting $\Delta t_n = -\Delta t_{n-1}$) in determining Δx. Inserting the budgeted $\Delta t = \pm 50$ ps uncertainty in second or third shock launch time into Eq. (3) leads to $\Delta\tau$ spanning $+65$ to -85 ps, and Δx spanning $+2.5$ to -8.5

μm. A comparison of modeling results and Eq. (3a) for the Δx shock merge depth uncertainty in second shock launch time Δt_2 is shown in Fig. 12(b). Applying a similar analysis to first order for the sensitivity of coalescence time and distance to the variability in first, second, and third shock velocities $\Delta u_n/u_n$:

$$\Delta\tau/(\tau - t_n) \approx -[c_n/(c_n - 1)]\Delta u_n/u_n \text{ and } \Delta x = u_{n-1}\Delta\tau \quad (4a)$$

$$\Delta\tau/(\tau - t_{n-1}) \approx [1/(c_n - 1)]\Delta u_{n-1}/u_{n-1} \text{ and } \Delta x = u_n\Delta\tau \quad (4b)$$

where the optimum coalescence time τ is ≈ 12.5 ns per Figure 11 and the expected shock launch times t_2 and t_3 are ≈ 7 and 9 ns per Figure 2(c). Equations (4a) and (4b) represent sensitivity for changes in overtaking and overtaken shock velocity, respectively. In Eq. (4b), we ignore the small 2nd order correction for the change in overtaking shock velocity due to changes in the compression state left by an earlier shock, valid for the current cases approaching the strong shock limit. Inserting the budgeted $\pm 2\%$ variability in first, second, and third shock velocities into Eq. (4) leads to $\Delta\tau$ spanning -120 to $+110$ ps and Δx spanning $+6$ to -18 μm. A comparison of modeling results and applying Eq. (4a) for the Δx shock merge depth uncertainty given uncertainty in second shock velocity $\Delta u_2/u_2$ is shown in Fig. 12(d). The good agreement in Fig. 12(c) is obtained using Eq. (4b) by assuming, based on simulations, that the trough power only affects the first shock velocity after it has entered the fuel (i.e., during only $\approx 1/3$rd of its travel time). If we tune to avoid the kinematically sensitive $c_3 = 2.4$ case where an

early third shock merges first with the second shock, then Δx only spans ± 6 μm. We then note that the contributions to variations in τ and x due to the budgeted variability in launch times and shock velocities are comparable, as would be expected for requirements balancing risk. Moreover, since the first shock breakout time and velocity will be observable on every shot, we can apply a postshot correction for its variability to the measured shock coalescence distance.

4. Accuracy

The drive fidelity of the "keyhole" target relative to the ignition target has been evaluated using 3D Hydra simulations. The simulations show between 4% less (during the trough) and 0.5% more (during the third pulse) hohlraum x-ray flux at the ablator opposite the VISAR line-of-sight. This can be attributed to the extra 3% by area high albedo Au cone being unable to match, at all relevant T_r, the losses from the ≈ 1 sr section of low albedo ablator it replaced. Nevertheless, given the previously quoted high Z wall and low Z ablator albedo uncertainties of $\pm 10\%$, we would thus expect $< \pm 1\%$ errors after correcting for relative fluxes between the keyhole and ignition hohlraum, and hence negligible $\pm 0.5\%$ fidelity errors in shock velocities. In addition, the 10%, 6%, and 5% random shot-to-shot laser power imbalances among quads during the first, second, and third pulse drives is expected to yield $< 2\%$, 1%, and 1% flux variability at the capsule surface on the VISAR line-of-sight, small compared to the $\pm 4\%$ required accuracies in setting the drive, respectively. The combined effect of residual uncertainties in as-built 1D capsule parameters such as ablator dopant concentration (e.g., $\pm 0.1\%$) and ablator thickness (e.g., ± 1 μm) are expected to provide $< 1\%$ and 2 μm variability in observed first shock speed and shock coalescence distance, small contributors compared to the laser performance tolerances described above. Based on the simulations shown in Figure 11 and these analytic estimates, the accuracy required in setting coalescence depth is set at ± 6 μm in Table I.

The systematic error in VISAR traces is $\pm 5\%$ of a fringe shift,[88] with an additional random variability of $\pm 5\%$ per temporal resolution element. The temporal resolution is 30 ps, set by dividing the required 6 ns sweep (to cover from first shock break-out at about 8 ns to at least 1 ns after the 12.5 ns coalescence time) by the number of 100 μm resolution elements across the 2 cm central part of the sweep.[90] The second random component is hence negligible averaged over typical ns observation times. Hence, for the higher sensitivity channel set at 3.1 fringes/20μm/ns, the fractional accuracies of the inferred velocities for the 20 μm/ns first, 37 μm/ns second, and 65 μm/ns third shocks are $\approx 1.6\%$, 0.9%, and 0.5%, well within the tuning requirements. The accuracy in coalescence distance is the quadrature sum of velocity and timebase errors. The 1.6% systematic first shock velocity error that dominates represents ± 1.3 μm over an 80 μm travel distance in D_2. By contrast, the accuracy in defining the time between the first shock break-out and successive shock overtake will be a small fraction of the 30 ps temporal resolution, typically 10 ps, hence $\approx 0.2\%$ over the 4.5 ns first
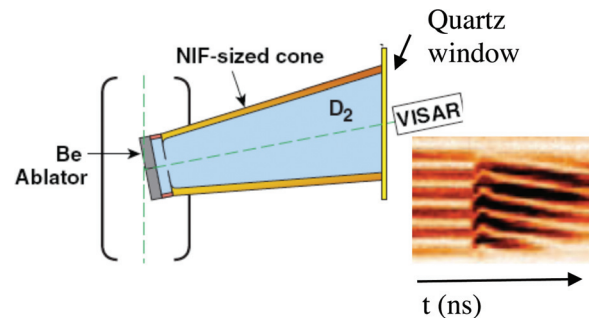

FIG. 13. (Color) OMEGA experimental set-up for testing 1st three shocks reentrant geometry, including example VISAR data.

shock transit time in the liquid D_2. The contribution from the residual uncertainty in the calibration of the sweep speed using an *in situ* optical comb fiducial[91] is expected to be 1% for both shock velocities and coalescence depths, as long as any non-reproducible sweep speed non-linearities occur over periods longer than the 330 ps fiducial comb spacing.

5. Experimental validation of technique

The viability of this tuning technique was successfully tested[70] in phases at OMEGA. First, we proved that the quartz window capping the liquid D_2 will not blank[92] due to ionization from NIC-relevant levels of hard x-rays (> 2 keV) emanating from Au laser plasmas that can be transmitted through a surrogate ablator BeCu sample. Second, we demonstrated strong reflection off shock fronts traversing a NIC-scale liquid-D_2 filled cone equipped with a planar (rather than spherical due to limitations on hohlraum size at OMEGA power levels) BeCu ablator of matched areal density (see Figure 13). The hohlraum conditions were designed to be a stringent test of window blanking by delivering up to $10\times$ more Au M-band radiation (> 2 keV) than expected during the third shock phase on NIF. We note that the other ignition capsule ablator designs, CH and HDC have about $2\times$ the optical depth to these > 2 keV x-rays, and will be even less at risk of window blanking. Third, we demonstrated VISAR measurements of overtaking shocks in the spherical converging geometry and shock strengths of interest by switching to mm-scale directly driven liquid D_2-filled CD capsules equipped with cones. Blanking of the D_2 was observed above third shock velocities (above 70 μm/ns), attributed to preheat from the shock front. This expected result has led to applying a different technique for monitoring the 4th shock as described in Sec. II C.

C. Timing of 4th shock

1. Physics basis for requirements

As for the second and third shocks, a correctly timed 4th shock (overtaking the first three shocks only after they have coalesced per Figure 10) is critical for keeping the fuel adiabat low for maximum compressibility. Too early a 4th shock will lead to an overtake in the fuel and an increase in fuel adiabat. In addition, too fast a 4th rise launches too strong a 4th shock and increases the fuel adiabat. Finally, too late or long a 4th rise delays the onset of peak power and leads to
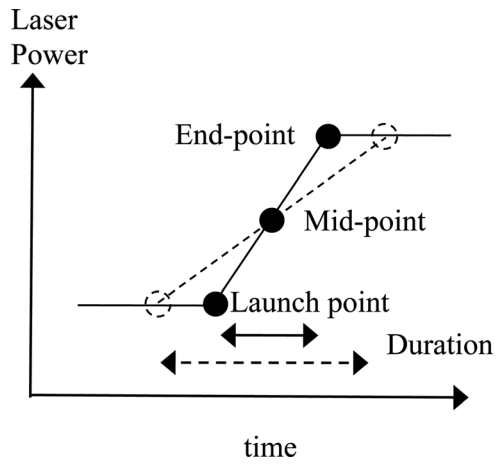
FIG. 14. Schematic showing important parts of 4th rise, with 2 examples (solid and dashed) yielding same shock coalescence time.

poorer coupling of the main drive to the capsule since its surface area is continually shrinking after the first three shocks' passage, resulting in reduced implosion velocity at fixed peak power. A convenient parameterization for the 4th rise is the mid-point time that sets the 4th shock coalescence time and its duration that sets the shock strength. This is schematically shown in Figure 14 where the dashed 4th rise laser power profile launches an earlier shock, but given a slower rise, a weaker hence slower shock leading to the same shock coalescence time as for the solid curve profile. Figure 15 quantifies the calculated sensitivities of average fuel adiabat and peak implosion velocity deviations from nominal as a function of changes in the laser pulse 4th rise mid-point time (for fixed duration) and 4th rise duration around the optimum values. Specifically, Figure 15(a) shows that adiabat increases by $\approx 10\%$ if either the midpoint time in the 4th rise is too early or if the 4th rise duration is too short by 200 ps. Conversely, Figure 15(b) shows that the implosion velocity decreases as the time to reach peak power (i.e., the sum of the 4th rise mid-point time and half the duration) is delayed. For example, a 200 ps delay in reaching peak power at a time when the first three shock induced particle velocity is $\approx 50\ \mu m/ns$ should lead to a 10 μm radius or 2% capsule surface area shrinkage, hence a 1% drop in peak implosion velocity, as shown in Figure 15(b). To maintain the adiabat and peak velocity to 6% and 1% of their design values and hence by Eq. (1) the ITF to 25% and 10% of its 1D design values requires ± 100 ps tuning accuracy on 4th rise mid-point time and duration. Applying the same kinematic analysis as for the first 3 shocks, with $c_4 \approx 4$ per Figure 11(a), the budgeted $\Delta t = \pm 100$ ps tolerance in 4th shock midpoint time leads to $\Delta \tau_4 \approx \pm 135$ ps, and the allowed variability in 4th shock velocity $\Delta u_4/u_4 = 2\%$ over a 3 ns transit time contributes an additional $\Delta \tau_4 \approx \pm 80$ ps.

2. Tuning technique

While the clear path to setting the 4th pulse timing was quickly recognized to be through measuring shock break-out time through an opaque witness plate,[93] several options have been considered for setting the 4th rise duration or slope. These include using a stepped witness plate to measure the
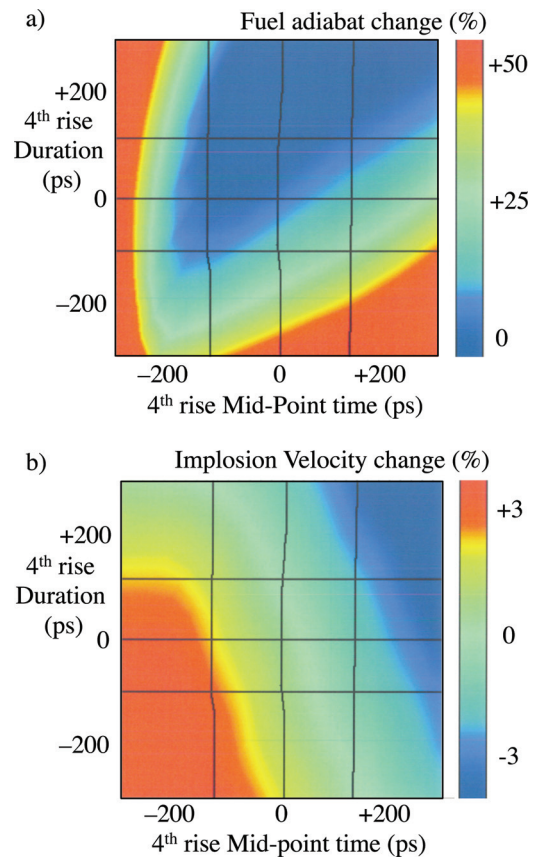

FIG. 15. (Color) Calculated (a) average fuel adiabat deviations and (b) peak shell velocity deviations from nominal vs. up to ± 300 ps changes in 4th rise duration and 4th rise mid-point time. The horizontal contours represent ± 3.5 eV/ns variability in 4th rise Tr slope and the vertical contours represent ± 90 ps in 4th shock breakout time.

coalesced 4th shock velocity from the differential shock break-out time, using an absolute measurement of the brightness of the shock break-out, and using Dante to measure the rate of 4th pulse hohlraum temperature rise. For the first option, a ± 100 ps shock transit time change over the ≈ 2.5 ns transit time of the 4th shock would appear to translate to an experimentally realizable[93] $\pm 4\%$ shock velocity accuracy from a stepped witness plate. However, it is the ± 50 ps tolerance between the 4th rise mid-point setting the shock breakout time and the 4th rise end-point setting the final shock strength that is relevant here (see Figure 14). This leads to a tighter $\pm 2\%$ shock velocity accuracy requirement, difficult to meet for a shock breakout technique for which both witness plate and streak timebase errors contribute. For the second option, the brightness temperature of the shock[65] scaling as the square of the shock velocity would have to be monitored to $\pm 4\%$ absolute accuracy in the optical Rayleigh-Jeans part of the blackbody spectrum, a difficult calibration proposition and subject to a systematic interpretation error due to any preheat taking it off the Hugoniot.[66] For the third option, the 4th rise laser power slope and hence duration can be directly related to the slope in T_r between ≈ 10 and 11.5 ns in Fig. 2(c). For a nominal 4th rise slope of 56 eV/ns averaged over the 1.6 ns 4th rise shown in Fig. 2(c), an uncertainty of ± 0.1 ns corresponds to $56 \times \pm 0.1/1.6 = \pm 3.5$ eV/ns in T_r slope. We have chosen the latter technique as it

a)

Streaked Optical
Pyrometer (SOP) +
VISAR

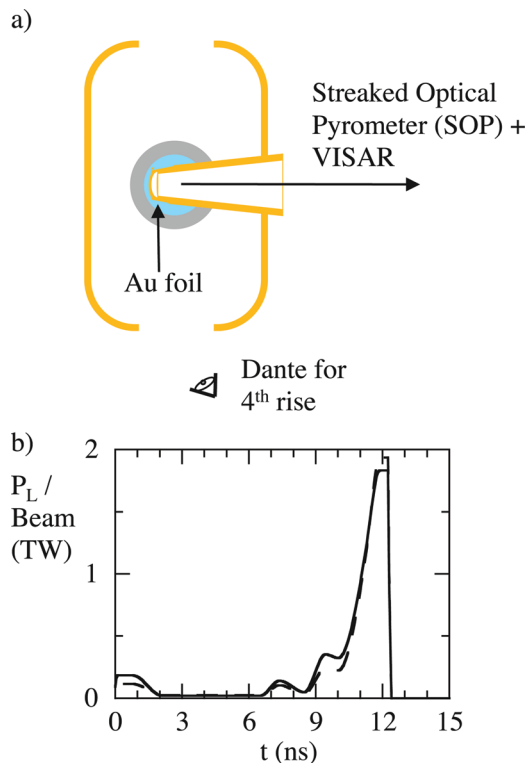Au foil

Dante for
4th rise

b)

FIG. 16. (Color) (a) 4th rise tuning experimental set-up for NIF shots. (b) Power per beam for 64 inner cone beams (solid) and 128 outer cone beams (dashed).

provides an achievable, orthogonal constraint in the parameter space of 4th rise duration and mid-point time as shown by the black contour lines in Figure 15.

Figure 16(a) shows the modified keyhole target design[94] that will be used for tuning the 4th shock characteristics using the VISAR, an associated streaked optical pyrometer (SOP),[95] and the Dante. The 4th shock geometry uses an identical re-entrant Au cone as for the first three shocks, but with a closed 20-μm-thick Au tip, spherically concentric with the ablator, with liquid D_2 only between ablator and cone tip. The distance between the inside of the ablator and the outside of the tip is set to measure the 4th shock ≈ 100 μm (≈ 1 ns) after it has coalesced with the prior 3 shocks. The Au end-piece serves as a witness plate that lights up in the optical regime when the 4th shock breaks-out, its high Z providing hard x-ray preheat shielding to avoid pre-expansion of its surface facing the SOP and potential temporal smearing of the shock break-out signature. The SOP uses the same line-of-sight, optics and cross-timing system as the VISAR, which will be essential for minimizing experimental timing offsets between these two diagnostics and for cross-timing to ± 50 ps with respect to the earlier first 3 shock timing campaign. The SOP is equipped with a 600 ± 40 nm bandpass filter, to avoid contamination from the 690 nm VISAR laser light and the 527 nm residual NIF laser second harmonic.

3. Accuracy

Based on Nova[93] and OMEGA[66] experience, the expected accuracy in defining the risetime of the shock breakout signal on the SOP is ± 25 ps. The contribution from

the residual uncertainty in the sweep speed timebase after *in situ* correction using the 3 GHz optical comb fiducial is expected to be ± 30 ps.

The Dante has a fixed view at $37°$ to the hohlraum axis through the bottom LEH, near optimum for spanning both the inner and outer cone plasmas but not the capsule. More importantly, the average azimuthal location of the Dante view is within $40°$ of the wall area facing the capsule surface diagnosed by VISAR and SOP. The principal errors in decreasing importance for the Dante Tr slope measurement are the uncertainty in the time-dependent LEH closure to soft x-rays, the uncertainty in the correspondence between the Dante measured wall flux and the average flux at the capsule, Dante component calibrations errors between 160 and 250 eV temperature spectra, residual scope timebase calibration errors, and residual errors in the 60 m signal cable dispersion compensation. A time-integrated multichannel 0.9 and >2 keV imager[96] with 100 and 50 μm-resolution viewing at $18°$ to the hohlraum axis will be used to infer the average LEH size[97] during the 4th rise. Based on simulations showing up to 10% LEH diameter closure by peak power (at Tr $= 250$ eV) representing an over-prediction of ≈ 25% on the estimated 3% accuracy measurements, there will likely remain a ± 5% uncertainty in LEH area closure rate translating to a ± 3 eV uncertainty over a 1.6 ns-long 4th rise, hence an error of ± 2 eV/ns. From simple viewfactor[78] arguments, the uncertainty in the ratio of x-ray flux measured by Dante to flux on the capsule is dominated by the uncertainty in relative fraction of laser illuminated solid angle to total wall solid angle Ω_W seen by Dante versus the capsule divided by the ratio,[3] F, of recirculating flux to laser spot flux. For a plausible 20% error in the ratio of illuminated wall fractions to account for uncertainties in relative brightness (i.e., due to cone-to-cone power transfer) between cones subtending different solid angle to Dante and to the capsule, and with $F = \alpha/[(1 - \alpha) + (\Omega_{LEH} + \Omega_{Caps})/\Omega_W] \approx 2$ for a typical 4th rise albedo $\alpha \approx 0.7$, this gives a 10% error in relative flux and hence ± 2.6 eV over 1.6 ns $= \pm 1.6$ eV/ns. The Dante calibration slope error is estimated as the absolute error[78,79] of $\sqrt{2} \times 4$ eV at these Tr multiplied by the 20% fraction of energy channels recording the bulk of the spectrum that are not common at 160 vs 250 eV, yielding ± 1 eV over 1.6 ns, hence ± 0.6 eV/ns. The Dante oscilloscope timebases that show up to 7% deviations from the nominal trace speed are correctable over the long term to 1% accuracy averaged over all significant channels and over the 1.6 ns 4th rise duration, hence representing a ± 0.6 eV/ns error. The uncertainty in the typical 20% signal cable risetime compensation is estimated at ± 3% error in flux rise based on variability in deconvolution technique results during the NEL campaign, hence ± 0.8% $\times 56$ eV/ns $= \pm 0.4$ eV/ns. These four uncertainties added in quadrature remain less than the ± 3 eV/ns budget.

3D Hydra simulations[89] predict <1% differences in hohlraum flux at the ignition capsule and at the ablator facing the SOP line-of-sight during the 4th rise, which translate to <0.5% uncertainty in shock velocity correction and hence negligible ± 10 ps uncertainty in shock breakout time. A plausible unmeasured 2% P_2/P_0 flux asymmetry due to uncertainties in the rising albedo and differential cone back-scatter losses during the 4th rise would lead to a ± 30 ps

break-out time error over the ≈ 3 ns transit time of the 4th shock. The uncertainty in 4th shock-relevant speeds between liquid D_2 and solid DT are estimated at $\pm 0.5\% = \pm 15$ ps over the 3 ns 4th shock transit time.

Figure 16(b) shows the starting point inner and outer pulse-shapes, truncated at peak power since simulations show the rest of the pulse has no impact on 4th shock arrival time or strength. Based on the measured shock break-out time and Dante 4th rise slope between about 160 and 250 eV, the midpoint on the 4th rise and rise duration would be varied between shots without changing the earlier pulse profile or the peak power.

4. Experimental validation of technique

The viability of using the VISAR and SOP for this re-entrant witness plate shock breakout measurement was successfully tested[70,94] at OMEGA using the experimental set-up shown in Figure 17(a). To test the system under the hard x-ray background expected at NIF at up to peak power, we drove the hohlraum to 230 eV over 1 ns, but with up to $12 \times$ more M-band x-rays because the OMEGA beams were at higher intensity than expected at peak power on NIF. A VISAR trace with superimposed self-emission typical of an SOP signature is shown in Figure 17(b). While the VISAR

signal is first lost due to hard x-ray preheat-induced expansion for the thinner ($< 35\ \mu m$) Au witness plates (at 4-5 ns), an abrupt rise in optical signal upon thermal shock break-out is observed at later times. These experiments showed that a sufficiently thick (40-μm) Au witness plate can delay significant preheat-induced expansion until after the thermal shock has broken out at a time in agreement with simulations. Calculations using the lower fraction of M-band preheat expected for NIF hohlraums due to lower beam intensities predict 20-μm-thick Au witness plates should be viable at NIF for ensuring the soft x-ray driven 4th shock breaks out before the preheat induced shock. Since the 4th shock transit time through such a Au witness plate is predicted to be 500 ps, a plausible $\pm 5\%$ uncertainty in shock velocity in Au would contribute a ± 25 ps error to 4th shock timing. Simulations show that preheat-induced expansion of the Au witness plate facing the capsule ablator leads to a ± 10 ps uncertainty in shock transit time for a maximum plausible 30% measurement error in M-band fraction during the 4th rise. The full roll-up of errors for all techniques will be tabulated later.

The fidelity and repeatability of the main part of the drive as measured by Dante [see Figure 18(a)] was evaluated
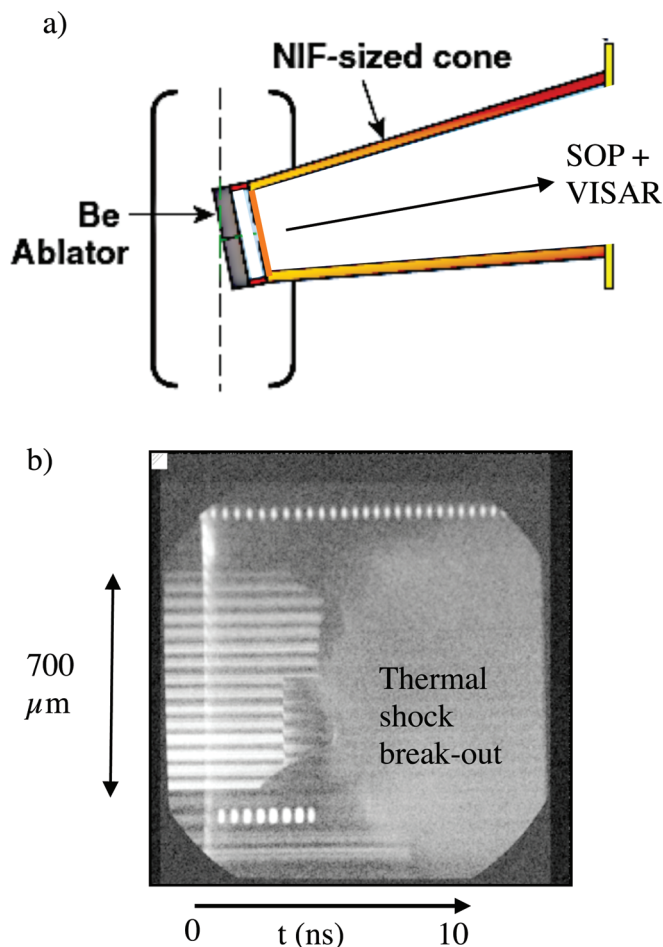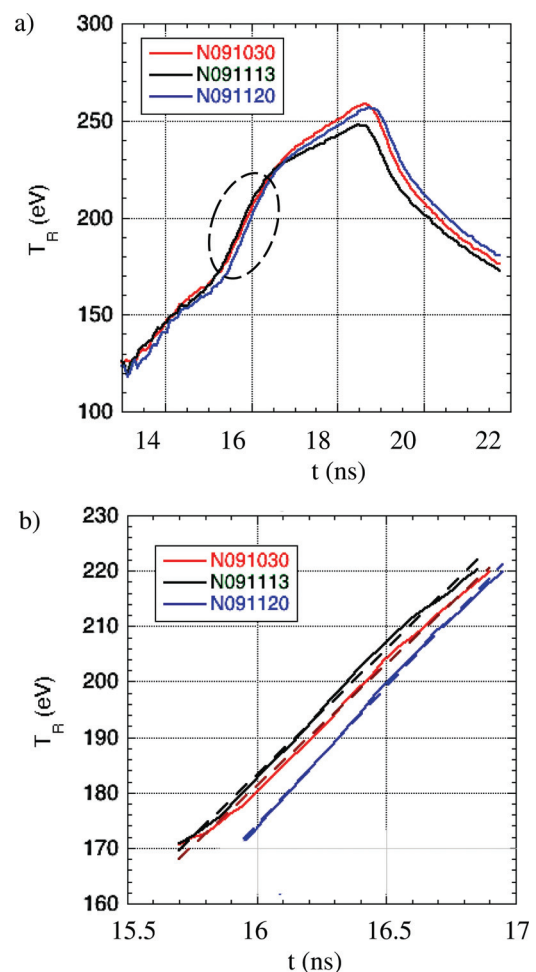

FIG. 17. (Color) (a) OMEGA experimental set-up for testing 4th rise tuning reentrant probing geometry. (b) Example VISAR streak showing signature of shock breakout of interest later in time.

FIG. 18. (Color) Measured Dante Tr during (a) last 5 ns and (b) zooming in on 4th rise of 19 ns long 840 kJ pulses driving 5.44 mm diameter hohlraums at NIF. Different colors represent three separate shots. Dashed lines are linear fits to the data. Shots had nominally identical pulseshapes but smaller wavelength separation (3 vs 8.5 Å) for shot N091030 (red curve) and 50% lower gas-fill for shot N091120 (blue curve).

for several NIF shots using 5.44 mm diameter hohlraums driven with 19 ns-long 840 kJ 300 eV CH design pulses. Figure 18(b) shows that a blow-up of the 4th rise portion between 170 and 220 eV between 15.5 and 17 ns met the expected slope of 48 eV/ns within ±4 eV/ns, close to the requirement of ±3 eV/ns, even though the drives at peak power varied, ascribed due to differential backscatter from the changing cone wavelength separation and gas-fill.

D. Ablator mass remaining and implosion velocity

1. Physics basis for requirements and sensitivity

For a given ignition design characterized by a peak laser power and laser energy, choice of hohlraum and capsule type and size, and initial assumptions on hohlraum and capsule coupling efficiency, there is an optimum setting for the combination of peak implosion velocity and amount of ablator mass remaining at implosion stagnation. An initially thin capsule can be driven to high implosion velocity in 1D, but per the rocket equation,[3] that leads to little residual ablator mass remaining, enhancing the feed-through of Rayleigh-Taylor instability growth and eventually to DT fuel preheating by x-rays. An initially thicker capsule will be more immune to shell break-up by hydroinstabilities, but reach insufficient peak implosion velocity to provide enough PdV work to ignite the hotspot. To maximize the product of the implosion velocity term and mix term of the ITF [Eq. (1)] that vary in opposite directions as the initial ablator mass is varied, we need to understand their dependencies on the remaining mass M_r. From the rocket equation $v_i = -v_{ex}ln(M_i/M_r)$, the sensitivity to M_r is given by:

$$\Delta M_r/M_r = -(v_i/v_{ex})[(\Delta v_i/v_i) - (\Delta v_{ex}/v_{ex})] \approx -3(\Delta v_i/v_i) \tag{5}$$

where the final approximation is for a typical peak implosion velocity v_i of 360 μm/ns, fixed ($\Delta v_{ex} = 0$) exhaust velocity $v_{ex} = \sqrt{(ZT_r/m_i)} \approx 120$ μm/ns, and hence fractional total mass remaining of $M_r/M_i = \exp(-v_i/v_{ex}) \approx \exp(-3) \approx 5\%$. Equation (5) suggests the scaling $v_i \sim M_r^{-1/3}$. Including the fact that the Be ignition design apportions about 60% of the final mass to DT fuel to balance the risk of feedthrough to the hot spot of hydroinstability growth seeded at the ablator–fuel interface[67,68] with the risk of preheating the fuel, we have the final ablator mass remaining M_a scaling locally as $M_r^{2.5}$, hence $v_i \sim M_a^{-1/7.5}$. If we first consider the case where the peak power P_L is varied, since $v_i \sim \sqrt{P_L}$ and $v_{ex} \sim \sqrt{T_r} \sim P_L^{1/7}$, there is partial cancellation per Eq. (5) leading to $v_i \sim M_a^{-1/5.4}$, close to the $v_i \sim M_a^{-1/5.2}$ scaling found in full radiation-hydrodynamic simulations. By contrast, capsule-only calculations typically show $v_i \sim M_a^{-1/12}$ and $\sim M_a^{-1/27}$ when we just choose to vary the thickness (hence initial mass) of the capsule by changing the inner or outer radius, respectively. The large difference in scalings is attributable to the nearly self-regulating dynamic[98] of a spherically converging system. For example, by increasing the initial outer radius, the absorbed energy is increased due to starting with a larger surface area, partly compensating for the extra payload mass. However, a larger capsule also repre-

TABLE II. Expected sensitivities of capsule implosion observables to 10% increase in key target, laser, and physics parameters.

Parameter increased by 10%	Change in observable		
	Ablator mass remaining (% of initial mass)	Peak velocity	Bangtime
Capsule thickness	+1.6%	−3%	+100 ps
Laser peak flux	−0.9%	+5%	−150 ps
Ablator opacity	+2.5%	−2%	+70 ps
M-band flux	−0.4%	+0.25%	−7 ps

sents a larger hohlraum energy sink, and hence we would expect the true v_i vs M_a power law with changing capsule thickness to be an admixture of the constant flux and constant thickness scalings. For example, a 10% thicker capsule equates to 2% larger diameter, hence 4% larger area and for typically 25% hohlraum drive coupling to the capsule, a 1% sink in drive fluence. By Table II, +10% in thickness compared to −1% in fluence equates to −3% vs −0.5% in v_i, and hence we expect the final power law to be 1/6th of −1/5.2 and 5/6th of −1/27 = −1/16, thus $v_i \sim M_a^{-1/16}$. This still leaves us the option of choosing the two adjustable laser and capsule parameters, in this case the peak power and the outer radius for changing thickness keeping the initial radius fixed, which are most different in their relative dependencies on v_i and M_a, for simultaneously controlling v_i and M_a. The choice of changing the outer versus the inner radius to change the ablator thickness is preferable from a target-coating process point of view.

To calculate the optimum mass remaining, we apply a power law fit curve to the results of hydrodynamic simulations plotted as squares for the Be(Cu) design in Figure 19 which shows that the $\Delta R_{mix}/\Delta R_{fuel}$ term in the ITF equation, representing the fraction of DT fuel mixed with hotter ablator making it less compressible and hence useful, varies as $0.001/(M_a/M_i)^{1.7}$ or $2.3/M_a^{1.7}$, with M_a now in units of % of initial mass M_i. Substituting the dependencies on M_a in the product of the implosion velocity and mix terms in Eq. (1), we are left with finding the maximum of $(1/M_a)^{0.5}[1-2.3/M_a^{1.7}]^{0.5}$ that occurs for $M_a = 2.9\%$ and a mix fraction = 37%. The starting point design value for the peak implosion velocity represented by the denominator
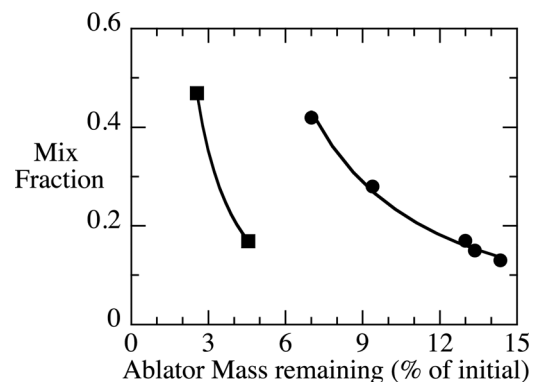

FIG. 19. Calculated ablator-fuel mix fraction versus ablator mass remaining for Be (squares) and CH (circles) designs, with analytic fits overplotted.

380 μm/ns in Eq. (1) is a result of such an optimization based on detailed hydrodynamics calculations allowing a mix fraction $\Delta R_{mix}/\Delta R_{fuel} = 30\%$ and a corresponding 3.5% ablator mass remaining. The uncertainty on the 30% value has been set conservatively based on the complexity of modeling mix[67,99] at $\pm 20\%$ mix fraction, corresponding to a possible 16% reduction in ITF. The $2.3/M_a^{1.7}$ mix fraction sensitivity dictates an acceptable uncertainty in ablator mass remaining at $\pm 1\%$ of the initial mass. Due to the self-regulating effect described above, that in turn translates to setting the initial ablator thickness to only $\pm 6\%$ or ± 10 μm precision. To ensure a balanced $\pm 16\%$ variability in ITF, the accuracy in setting the peak implosion velocity is $\pm 2\%$, representing a $\pm 4\%$ accuracy in setting peak flux as listed in Table I. Comparing the 300 eV CH(Ge) design with the 285 eV Be(Cu) design, the ratio v_i/v_{ex} is by design less (≈ 2.5 vs. 3 with $v_i = 360$ μm/ns) to leave more (10%) ablator mass remaining to counteract lower ablative stabilization of hydrodynamic instabilities due to the lower ablation rate[100] of the higher Z ablator. The calculated dots and associated power law fit also plotted on Figure 19 for various thickness CH(Ge) capsules show that a $\pm 1.5\%$ accuracy in ablator mass remaining will be required to keep the mix fraction within tolerable limits.

Table II summarizes the expected Be(Cu) design sensitivities of three observables (ablator mass remaining, peak implosion velocity, and bangtime) to 10% increases in the capsule thickness (for fixed inside radius), peak laser flux, ablator thermal opacity, and M-band fraction around the optimum point (380 μm/ns, 3.5% ablator mass remaining). Figure 20 shows the expected sensitivity of the two principal observables, mass remaining and implosion velocity to initial capsule thickness for varying outer radius (the red constant peak flux contours spaced by 10% in peak flux) and to peak flux (the black constant thickness contours spaced by 7% in
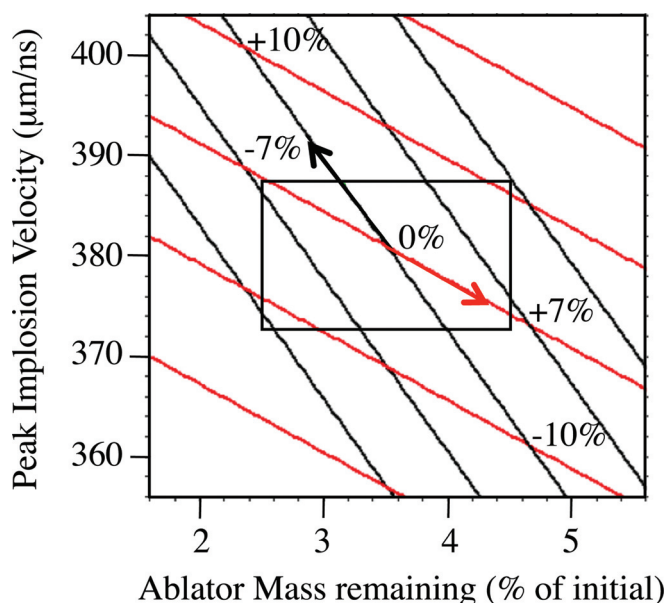

FIG. 20. (Color) Calculated peak implosion velocity and remaining ablator mass sensitivity to variations in peak laser power (along black contours spaced every 7% in thickness) and initial ablator mass (along red contours spaced every 10% in peak flux). The black and red arrows signify increasing flux and thickness, respectively.

thickness). In general, both parameters will have to be varied to reach the required regime in peak implosion vs. ablator mass remaining space shown as a box in Figure 20.

2. Tuning technique

We experimentally and computationally evaluated various approaches for measuring the ablated or remaining mass, including Cu dopant activation by DT burn neutrons,[11,73] shock-flash, or burn proton spectroscopy[101–103] using wedge-range filters in front of charged particle CR-39 foil detectors (WRF), tracer emission burnthrough spectroscopy,[104] x-ray burnthrough,[65] and x-ray gated or streaked radiography.[105] The nuclear activation technique's principal drawbacks are contamination from other sources of Cu in the chamber and interpretation of shell $\rho \Delta r$ in the face of difficult to calculate Cu mix between the last Cu-doped layer and the 5-μm-thick initially pure Be ablator inside layer [see Figure 2(b)] which is the principal source of remaining ablator mass. In addition, the technique does not port easily to the CH(Ge) and HDC(Mo) designs without adding special tracers.

The D-^{3}He 15 MeV protons are created both during shock coalescence at the center of the capsule gas-fill (occurring at a shell radius of about 250 μm, 400 ps before bangtime, and commonly denoted shock-flash) and at peak compression, commonly denoted bangtime. To use the peak compression protons would require a higher fill lower convergence implosion to keep the final shell $\rho \Delta r$ well below the ignition design value of 0.4 g/cm^2 to avoid protons ranging out after 0.2 g/cm^2. Such a higher fill leads to loss of trajectory fidelity due to earlier deceleration. By contrast, the expected total areal density during shock flash is only 0.06 g/cm^2, leading to an easily observable ≈ 2.5 MeV downshift of protons born at that time. The principal issue with the shock flash proton spectroscopy is that the unablated shell areal density we are interested in is only 50% of the measured total areal density for the optimum mass remaining. Specifically, calculations show that the total areal density only increases 20% for a $2 \times$ increase in ablator mass remaining, with 10% scatter in this correlation, hence leading to only a 25% accuracy in inferring the unablated areal density. This is in contrast to OMEGA implosions[106] for which the unablated areal density at shock flash dominates since the mass remaining is typically $3 \times$ greater due to the lower implosion velocities reached per Eq. (5). Moreover, the mass remaining $\sim r^2 \rho \Delta r$ will be most sensitive to the r^2 term, and hence the shell radius at shock flash, not a direct observable unless the protons bursts are time-resolved.[107] Both the activation and burn proton spectroscopy techniques would use the nuclear bangtime[108] (either from neutrons or gamma-rays) to infer peak implosion velocity for which $\pm 2\%$ in implosion velocity over the 3 ns peak drive phase shown in Figure 2(c) is equivalent to a measurable ± 60 ps in bangtime. However, both bangtime ρr and bangtime are more integrated measurements that can be directly affected by late time mix.

Burnthrough techniques are difficult to transpose from their usual planar geometry to a re-entrant keyhole-like geometry for better fidelity, because unlike shock timing, one

must follow the capsule for at least 2/3 of its trajectory before it is ballistic. However, a series of planar x-ray burn-through experiments[100] have been carried out at the OMEGA facility on all three ablator candidates at up to NIC-relevant peak radiation temperatures (Tr ≈ 270 eV). They have constrained our understanding of the ablation rates to ±5%–10%, corresponding to ±3% in remaining ablator mass when including uncertainties in transposing to a convergent system, = ±80% of the 3.5% optimum ablator mass remaining as listed as the initial uncertainty in Table I.

We elected to use time-resolved x-ray radiography that will extract the time-resolved ablator density profile through Abel inversion from which remaining mass, areal density, position, and velocity of the ablator as a function of time can be derived. Like the ρr measurements, it has the advantage of measuring the small fraction of the remaining mass for an ignition capsule design that has a much larger fractional tolerance than the ablated mass sensed by burnthrough techniques. Specifically, even accounting for adding 5% extra Be mass to these non-cryogenically layered implosions to match the DT fuel areal density, the required accuracy in the mass remaining observable is ±1% out of 8.5% (±1.5% out of 16% for the current 300 eV CH(Ge) design), a ±7%–12% relative error bar. In addition, we should be able to see an x-ray flash at bangtime for further corroboration of the implosion dynamics. The optimum point in the capsule trajectory for inferring mass remaining and peak implosion velocity is around r = 300 μm. The shell has not yet started to thicken at a rate comparable to its average implosion speed or reach a thickness comparable to its average radius due to convergence effects, which would impair accurate velocity and mass remaining measurements. Simulations show that 99% of all the ablator mass that will be ablated is gone by the time the capsule reaches a radius of 300 μm, with peak velocity occurring about 300 ps later. Moreover, from the results of many simulations using different realizations of laser and target residual shot-to-shot variations within specifications, we find that the extrapolation errors in ablator mass remaining and peak implosion velocity from measurements taken earlier at r = 300 μm are 2–3 × less than the ±1% and ±2% error budgets, respectively.

An example of a calculated 6.7 keV streaked radiograph across a Be capsule diameter and a transmission lineout across the image when the shell has reached the radius of interest is shown in Fig. 21. We note that the minimum limb transmission is designed to be 20%–30% by appropriate choice of backlighter energy. This value is chosen based on balancing desirable improved signal-to-noise with deleterious increased sensitivity to uncertainties in correcting for the instrument spatial modulation transfer function (typically 0.8 on limb spatial scales) as the limb contrast is increased. The backlighter energy is chosen to be below the K edge of the dopant material (9 keV for Cu and 11 keV for Ge) to minimize extra absorption from partially ionized ablated dopant material.

The experimental set-up for NIC is shown in Fig. 22(a). The capsule is identical to the ignition capsule except that the 75 μm of DT ice is replaced by an equivalent areal density of 10-μm thick Be on the inside, and a DT hot spot
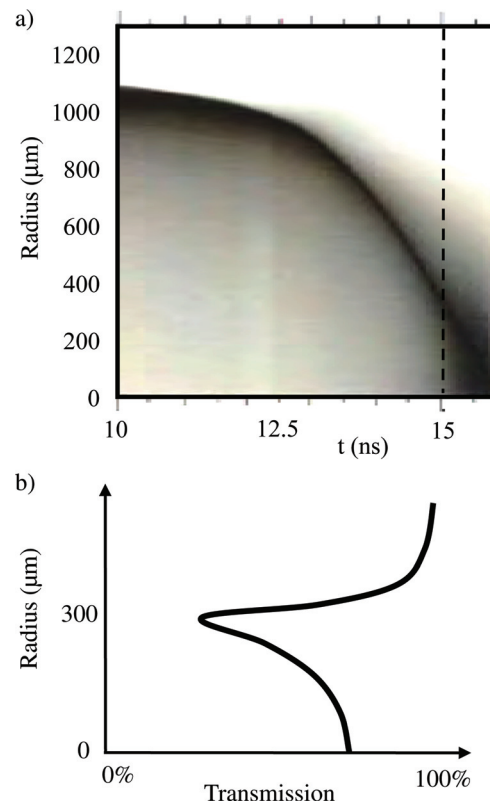

FIG. 21. (Color online) (a) Calculated streaked radiograph of BeCu target with 6.7 keV backlighter. (b) Extracted transmission lineout corresponding to r = 300 μm shell radius.

equivalent capsule fill density of ≈0.4 mg/cc is used to maintain fidelity in its trajectory. The radiography source is an area backlighter in transmission mode created using two 50° quads irradiating a 5- to 7-μm-thick Fe backlighter foil placed on the side of the hohlraum producing 6.7 keV Fe He-alpha (9 keV Zn He-alpha for the CH(Ge) and HDC designs). Slots, 110-μm tall by 1.2-mm long, are cut out of the hohlraum wall opposite each other to allow a fan of x-rays to backlight the capsule equator. They will be filled and encased in ≈150 μms of HDC to delay slot closure,[109] as already demonstrated. We choose to backlight around the equator rather than through the poles since by viewfactor considerations [see Figure 22(a)] the equator is least affected by the absence of the 2 missing outer beam quads. Viewfactor analyses suggest the presence of the modest sized slots (representing <0.5% of solid angle) and the 2 missing drive quads even if not compensated for will have negligible effect on the perceived trajectory or Abel inversion in the face of the small 1% drive asymmetry. The backlighter quads are equipped with phase plates creating elliptical 700 × 1200 μm spots to illuminate a 1.5 mm diameter of interest. The 110-μm slot width is chosen to maximize photon throughput while avoiding excessive sensitivity to 20-30 μm misalignments in position of capsule with respect to hohlraum, the far slot, parallax from residual few mrad hohlraum tilt, and residual capsule P_1 or m = 1 drive asymmetry. To avoid saturating the streak camera electron optics leading to space charge distortion effects by the self-emission flash expected to be 10 000 × brighter at bangtime on axis, we will use a high Z block over the central 50–100 μm of the field-of-
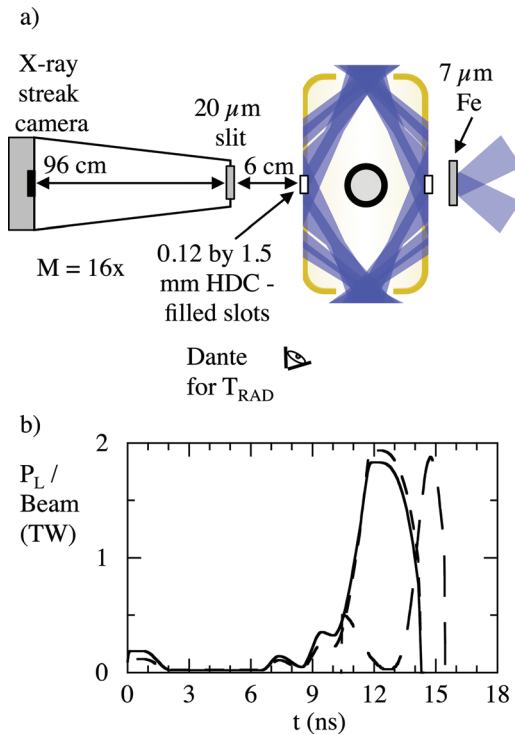
FIG. 22. (Color) (a) Streaked capsule radiography experimental set-up for NIF shots. (b) Power per beam for 64 inner cone beams (solid), 120 outer cone beams (dashed), and 8 50° beams used for backlighter (dotted-dashed).

sion of this in-flight capsule radiography technique as a final check of surrogacy.

Figure 22(b) shows that the hohlraum is driven with the full pulseshape for best fidelity. The baseline backlighter pulseshape is a $\approx$2 TW/beam pulse, kept short to maximize power given energy limits, but suitably delayed and long enough at 1.5 ns to cover the time-frame for capturing the r = 600 to r = 200 μm phase of a capsule imploding on average 300 μm/ns. We will use a prepulse shown to double the x-ray conversion efficiency of the main pulse.[112]

3. Accuracy

Simple photometrics estimate based on known backlighter efficiencies[113] suggest the shot noise-limited accuracy will be sufficient to provide $\pm$3 (2)% accuracy in relative mass remaining (vs. the $\pm$7%–12% required tuning accuracy) and $\pm$1 (2)% accuracy in velocity for the streaked (gated) radiography cases, respectively.

A host of other random errors and systematic errors have been evaluated. For the target, they include uncertainties in initial thickness ($\pm$1 μm, small compared to $\pm$10 μm required tuning accuracy) and in initial ablator areal density and dopant fractions ($\pm$1% and 0.1%, leading to $\pm$3% in relative mass remaining). The major uncertainty lies in the 0.25% Ar fraction by atom required for ensuring adequate Be coating uniformity (not present for CH or HDC designs). Since the Ar contributes about 45% to the remaining ablator opacity at 7–8 keV, the demonstrated Ar characterization accuracy[114] of $\pm$0.05% corresponds in $\pm$9% to the opacity and in the relative mass remaining. For the laser, an expected $\pm$1.5% uncertainty in peak power delivered corresponds to about $\pm$3% in the remaining mass, while the shot-to-shot variability will be 2 $\times$ larger.

For the physics, errors include uncertainties in unablated material opacities at the backlighter photon energy of interest and in the distribution of remaining Cu or Ge in the presence of hydroinstability growth for properly weighting the ablator opacity. The former contributes <5% to the uncertainty in inferring mass remaining which includes accounting for the uncertainty in the 5%–10% reduction from cold opacity of the unablated doped material preheated to a calculated but unmeasured 50-100 eV temperature. The latter contribution has been estimated based on highly resolved 2D and 3D hydrodynamic simulations[67] predicting up to 10% mixing of 0.5% Cu-doped Be (Ge-doped CH) into the inner pure Be (CH) remaining at the time of interest just before deceleration. Since the unablated opacity of 0.5% Cu-doped Be is 2.5 $\times$ higher than pure Be below the Cu K edge, this provides a 15% increase in perceived mass remaining if unaccounted for, matching the error budget. The dominant perturbation mode numbers are sufficiently high (100 corresponding to 20 μm spikes) that the sampling error along the 110-μm-wide line-of-sight will be negligible (<2%). Should the level of mixing between doped and pure Be or CH prove to be larger, the back-up plan is to switch to uniformly doped ablators of equivalent areal density over the inner 15 μm. Separate from the dopant mixing issue, hydroinstability growth will lead to an overestimate of the mass remaining in that the

view. We calculate that a bangtime flash of similar strength to the backlighter should still be seen from Compton scattering from the hohlraum fill and ablator plasmas. Calculations with simulated data show that the partial absence of radiography data should have negligible effect on the required accuracy of the Abel inversion for extraction of the various moments of the limb profile. A 16 $\times$ magnification 1D imaging system[110] equipped with a 20-μm-wide slit set orthogonal to the slots casts a 1D-resolved image onto an x-ray streak camera photocathode providing a 4-ns sweep with 30 ps resolution. The slit width is chosen to maximize throughput by matching the expected limb widths. A 4ω UV comb fiducial[111] has been designed to provide 100 ps pulses every 300 ps in a 2-ns train for correcting for any local sweep speed deviations and nonlinearities *in situ* at the required level of accuracy of $\pm$1% over a 300-ps measurement interval.

An alternate experimental design has been fielded recently using multiple short slit imaging onto an x-ray framing camera spanning $\approx$1 ns of the capsule trajectory. This has the advantage of a fixed gate propagation speed and interstrip timing that can be calibrated and shown to be repeatable to 1%–2% accuracy. It has poorer time resolution (70 ps currently, 35 ps possible in the future) leading to more motional blurring of the radiographed limb (25 μm at 350 μm/ns currently). The plan is to compare both the streaked and gated x-ray radiography results to increase confidence in both before choosing one for the remaining shots. The capsules will be filled with a mixture of D-^{3}He to gather an independent measure of total capsule areal density during shock flash from the proton slowing as measured by the WRFs. We are designing a suitably dudded cryogenically layered ver-

radiographed limb along its line-of-sight will not be able to separate out the opacity contribution of ablated material residing between unablated spikes. 3D simulations with realistic surface roughnesses show that the ablated mass between the spikes is similar to the spike mass with 3% of the unablated material residing in spikes at peak velocity. Hence, multiplying by the typical 2/3 ratio of residual opacity of the ablated material (dominated by the dopant) to the opacity of the unablated material, the overestimate in mass remaining is an insignificant 2%. We note that although the ablated material at even larger radii retains opacity due to the mid-Z dopant, its contribution to the radiograph appears as a long scale-length (typically 100 μm) absorption wing, easily separated from the sharp unablated limb feature as shown in Fig. 21.

4. Experimental validation of technique

An experimental demonstration[72] of the streaked radiography technique on 0.5-mm-diameter graded-doped Be(Cu.$_{03}$) capsules driven by 200 eV, 2.5 ns-long shaped drives was completed at the OMEGA facility using a similar set-up as planned for NIF. The experiments were designed to check backlighter uniformity, sensitivity to thickness and to position of the Cu dopant which was even a greater contributor to the optical depth due to the higher concentration of Cu required to approximate the same level of optical depth as for NIC with a smaller capsule. A typical streaked radiograph using the Vanadium He-alpha 5.2 keV line is shown in Figure 23(a). The Abel-inverted analyzed results plotted in terms of pairs of measured peak velocities versus inferred ablator mass remaining are shown in Figure 23(b) for two different initial thickness capsules. Overplotted as squares are the Lasnex postshot calculations. The statistical accuracy on its own met the $\pm 1\%$ of the initial mass requirement despite having 3–4 $\times$ larger fraction of the mass remaining than expected for NIC implosions. In addition, Figure 23(b) shows that the data with the lowest statistical inaccuracy just met the $\pm 2\%$ peak implosion velocity precision (no *in situ* fiducial was used). Despite the scatter in the data for the nominally identical shots, it is promising to see that all the points follow the expected trend of less mass remaining for higher velocity. Specifically, for the conditions of this experiment, $v_i/v_{ex} = 130/100 = 1.3$, hence expect $\exp(-1.3) \approx 30\%$ mass remaining as seen. Equation (5) then predicts a slope of $dM_r/M_r \approx -dv_i/v_i$ that is close to that observed.

E. Peak drive symmetry

1. Physics basis for requirements

The time-integrated imploded core symmetry is mainly set by the drive symmetry during the peak power phase of the pulse. For example, a 0.4% applied P_2 flux asymmetry will lead to a core asymmetry magnified[71] by the (convergence ratio (CR) − 1), yielding a 15% P_2 on the ignition capsule hot spot. The close to cubic power law in the symmetry term in the ITF reflects the fact that a $\Delta R/R$ relative distortion of the hotspot of radius R due to inward going fuel and ablator spikes will reduce the burnable spherical volume by $3\Delta R/R$, requiring $3\Delta R/R$ more energy to recover that vol-
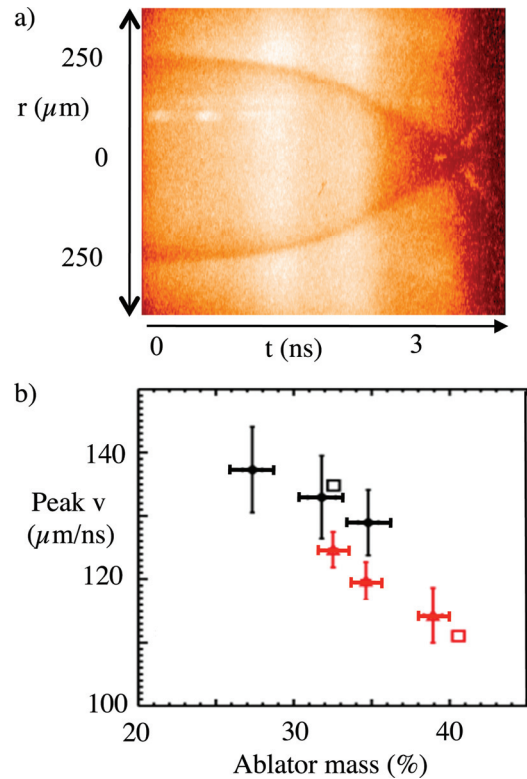

FIG. 23. (Color) (a) Example of streaked 5.2 keV radiograph of 0.5 mm initial diameter BeCu capsule driven by OMEGA 200 eV, 2.5 ns shaped drive hohlraum. (b) Solid points are extracted peak implosion velocity versus % ablator mass remaining from 6 shots using 30 μm (black) and 40 μm (red) initial thickness graded doped BeCu shells. Open squares are postshot Lasnex simulations.

ume by increasing the scale by $\Delta R/R$. The power law is quartic as ΔR is defined here as an rms perturbation, and hence $(1-1.2\sqrt{2\Delta R/R})^3$ approximates for small distortions as $(1-1.2\Delta R/R)^4$. The specification on the acceptable rms hotspot asymmetry listed in Table I is 16% making it the largest contributor to reducing the ITF, a factor of 2 from its nominal 1D value. The rms hotspot asymmetry is based on the quadrature sum of calculated growth of known residual low- and mid-mode imperfections of the shell and DT fuel[115] and from expected post-tune drive asymmetries. The drive asymmetry budget is further divided into 9% rms for intrinsic tuning errors and 7% for random asymmetries due to power imbalance. In terms of Legendre modes applicable to these cylindrical hohlraums (neglecting for the moment non m=0 modes), the intrinsic asymmetry budget further breaks down as $7\sqrt{5} \approx 15\%$ in P_2 and $5\sqrt{9} = 15\%$ in P_4 coefficient since an rms value = P_n coefficient / $\sqrt{(2n+1)}$.

We will control P_2 and P_4 independently by a combination of changing the peak power ratio between laser beam cones and by changing the hohlraum length and axial displacement of the cone pointing defined by the intersection point of all beams within a cone. Besides the traditional technique of changing the input laser power on a cone-by-cone basis, we have also shown sensitivity of core P_2 asymmetry to power transfer between cones due to three-wave mixing[116] where they cross in the flowing LEH plasmas that can be controlled by changing the relative wavelengths of the

cones.[6] Similarly, the choice of either changing the hohlraum length and pointing or just the pointing depends on the amount of clearance for the laser spots with respect to the LEH edges.

2. Calculated sensitivity

By the peak drive portion of the pulse, simulations predict that a combination of high Z inward blow-off from the hohlraum wall and fill-gas densification and refraction from the wall and capsule ablation moves the centroid laser absorption regions ≈1 mm back along the incoming beam paths. This is shown schematically in Figure 24 by the laser beam arrows ending at some radius r before reaching the hohlraum walls. Such simple spot motion analysis (based on either soft[117] or hard[118] x-ray imaging) was successfully used to explain time-integrated[119] and time-varying[120] P_2 asymmetry in vacuum Nova and OMEGA hohlraums. The spot motion in the NIC ignition hohlraums reduces the average angles subtended by the beam absorption locations such that they have moved from being near the P_3 nodes at 40° and 90° to being near the nodes of P_4 (30° and 70°). This gives simultaneous symmetry control for all modes through P_5 by in general applying a different inner to outer cone power fraction than used during the foot portion (close to 1:2, matching the number of beams per cone ratio).
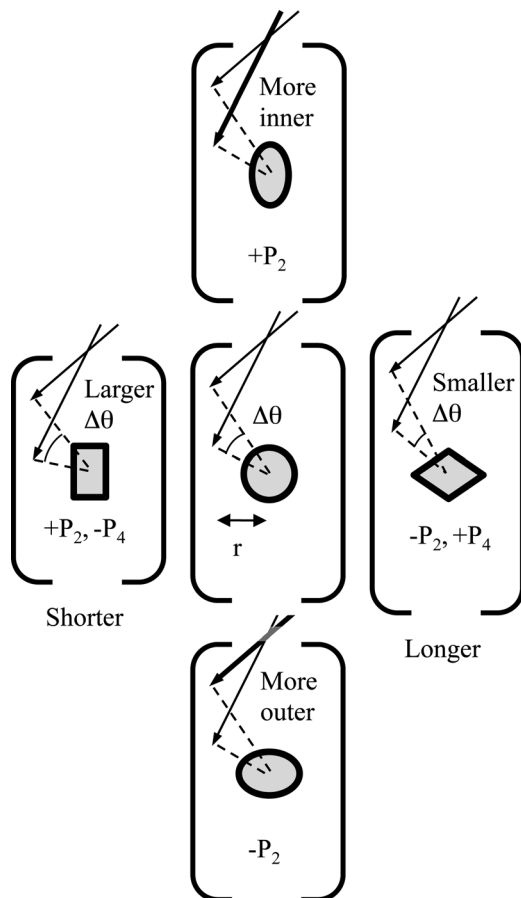
Figure 24 also shows how the core P_2 asymmetry can be varied on its own by changing the inner to outer cone power ratio at the nodes of P_4. Per the same analysis as for the early time asymmetry in Sec. II A, the change in P_2 at the wall around a value of zero due to a change in peak inner cone fraction at the wall $\Delta CF/CF$ is given by $2P_2(70°)(\Delta CF/CF)/(F+1)$. For $\Delta CF/CF = 5\%$, $F = 4$ for a typical peak power albedo $\alpha = 0.85$, and accounting for a cone averaged radiation transfer function[3] of 60% leaves 0.4% P_2 at the capsule magnified by 35 × convergence to 15% P_2 on the hotspot, the budgeted precision. The required accuracy in setting the peak $\Delta CF/CF$ is ±5%, listed in Table I.

To vary P_4, the key is to change the difference in angle $\Delta\theta$ subtended by the inner and outer cone spot centroids at the capsule. For example, if one reduces $\Delta\theta$, the part of the capsule at a polar angle of ≈50° subtending an angle in between the cones will experience greater drive than the parts outside the cones at 0° and 90° (for a spot-to-capsule radius ratio <4), leading to a diamond-shaped core as shown in the right-hand side in Figure 24. One could change $\Delta\theta$ by axially displacing inner and outer cones with respect to each other, but that would reduce clearance at the LEHs where cones cross, requiring a larger LEH size and reducing hohlraum efficiency, or requiring a smaller spot size increasing intensity and hence the susceptibility to LPI instabilities. Thus, we choose to change the hohlraum length by ΔL while keeping the beam locations fixed at the LEH. This moves the inner and outer cones together by $\pm\Delta L/2$ per side, maintaining their axial separation at the wall, but providing a cone-dependent angular change $= \Delta L\sin^2\theta/2r$. For example, for $\Delta L = 400$ μm, r = 2200 μm, $\theta = 70°$, and 30°, the change in $\Delta\theta$ is .057, ≈3°. Given $|dP_4/d\theta| = 2$ near nodes, the change in P_4 at the wall is 0.1/(F+1) = 2%. Accounting for a cone averaged geometric radiation transfer function[3] of 10% leaves 0.2% P_4 at the capsule magnified by convergence to 8% P_4 on the hotspot. Such a beam shift will change the core P_2, as schematically shown in Figure 24. In this case, $dP_2/d\theta$

FIG. 24. Schematics of qualitative variations in P_2 and P_4 core shapes as a function of changes in cone power balance and in hohlraum length, with pointing staying fixed with respect to LEH plane.
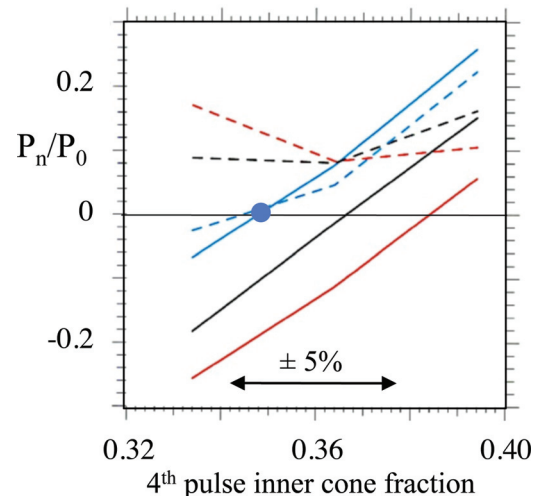

FIG. 25. (Color) Calculated symmetry capsule core P_2/P_0 (solid) and P_4/P_0 (dashed) as a function of 4th pulse inner cone fraction for three hohlraum lengths: nominal + 400 μm (red), nominal (black), and nominal − 400 μm (blue).

is less, ≈ 1, but the average transfer function is much greater at 60%, leading to a 20% change in core P_2.

Figure 25 shows Lasnex radiation hydrodynamics simulation results of the core P_2 and P_4 asymmetry for a typical $20 \times$ convergence symmetry capsule (in this case for a CH(Ge) 300 eV design) as a function of 4th pulse inner cone energy fraction for three hohlraum lengths differing by ± 400 μm. The optimum hohlraum length from this calculation is represented by the blue curve for which the cores P_2 and P_4 are both near zero (marked by the blue point) for the same inner cone fraction of 0.345. The change in dP_4/dCF slope sign versus hohlraum length in Figure 25 can be explained by the fact that the more beam centroids move off the nodes of P_4 through a hohlraum length change, the more the asymmetry becomes sensitive to the cone power balance. The simple analytic model predicts that dP_4/dCF should be zero when $P_4 = 0$, while Figure 25 shows that $dP_4/dCF = 0$ at a non-zero value of P_4, ascribed to neglecting mode coupling for a spherical capsule in a cylindrical hohlraum.[3] The analytic predictions corrected for a 40% reduction in symmetry capsule sensitivity due to $1.8 \times$ lower convergence and use of gold versus higher albedo U hohlraums (F = 3.5 instead of 4) compare well with other simulation sensitivities near the point of best symmetry: $\Delta P_2 = +9\%$ vs. $+10\%$ for $\Delta CF/CF = +5\%$, $\Delta P_2 = -12\%$ vs. -10% for $\Delta L = +400$ μm, and $\Delta P_4 = +5\%$ vs. $+8\%$ for $\Delta L = +400$ μm.

3. Tuning technique

The experimental set-up and pulse shape used for peak power core symmetry measurements on NIF are shown in Figures 26(a) and 26(b). Besides x-ray imaging, we will be simultaneously monitoring the hohlraum T_r profile with Dante, and the neutron bangtime and yield with nToF.[108] As for the convergent ablation radiography measurement, the DT fuel is replaced by an equivalent areal density of pure Be or CH to emulate the ignition capsule trajectory and hence drive symmetry history sampled (see Figure 27). As shown in Fig. 26(b), the full 1.2 MJ pulse is best for certifying that the symmetry is adequately tuned (to $0 \pm 7.5\%$ in hotspots P_2 and P_4 as listed in Table I) before proceeding to cryogenic-layered implosions and ignition attempts. Assuming late-time laser-plasma coupling physics has been assessed and can be accounted for computationally, simulations show that the P_2 and P_4 components vary by only $\pm 15\%$ for cases where the pulses have been either truncated by ≈ 0.5 ns in time or reduced in peak power to 1 MJ levels.

To avoid large core distortions when tuning starts (potentially $>40\%$ as listed in Table I based mainly on several 100 μm uncertainties in where the inner cone energy deposits its energy) that can lead to cross-coupling between modes complicating the inference to drive asymmetry, the capsule convergence ratio will be reduced by filling with 50 atm of He and H isotopes at room temperature. This corresponds to 8 mg/cc compared to the 0.3 mg/cc DT ignition gas fill that represents about 1/3 of the final hot spot fill after accounting for partial fuel inner surface ablation. Including the $2 \times$ higher temperatures expected of THD cores, we would hence expect for equivalent back pressure = nkT, a
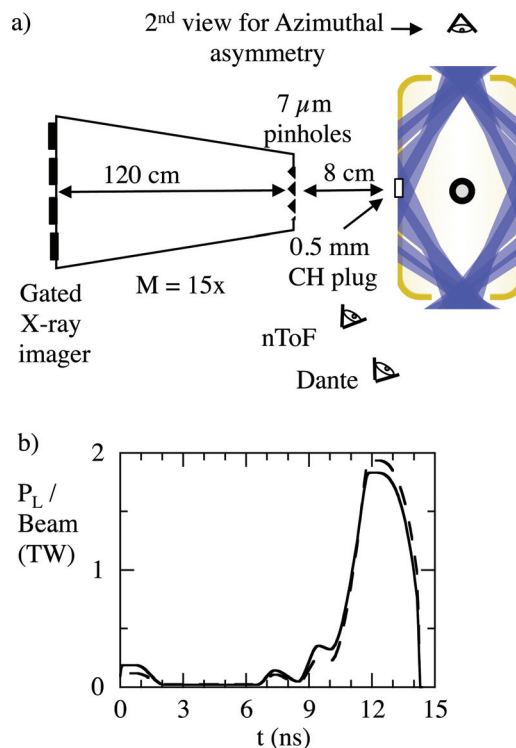

FIG. 26. (Color) (a) Symmetry capsule core x-ray imaging experimental set-up for NIF shots. (b) Power per beam for 64 inner cone beams (solid) and 128 outer cone beams (dashed).

reduced symmetry capsule convergence by $4^{1/3} \approx 1.6 \times$. The reduced convergence should have minimal effect on drive symmetry sampled since the capsule trajectories are ballistic a few 100 ps before onset of deceleration. A mixture of He and up to 25% D_2 that remains gaseous at the cryogenic hohlraum conditions will be used for maximizing Bremsstrahlung emission ($\sim Z^2$) and providing a nuclear bangtime at yields below 10^{12} to avoid damage to the CCDs[121] used as recording medium behind the gated x-ray framing cameras.[28]

The x-ray detection is filtered for >7 keV to provide a strong signal from the predicted 3 keV temperature core self-emission unobstructed by shell reabsorption. The imaging is
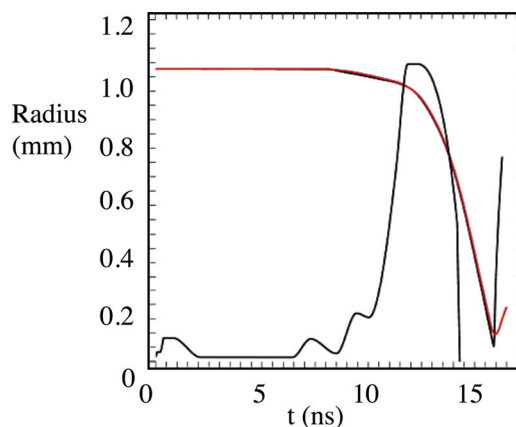

FIG. 27. (Color) Comparison of calculated trajectory of inner ablator of symmetry capsule (black) versus trajectory of DT fuel of ignition capsule (red). Also shown is total laser power profile.
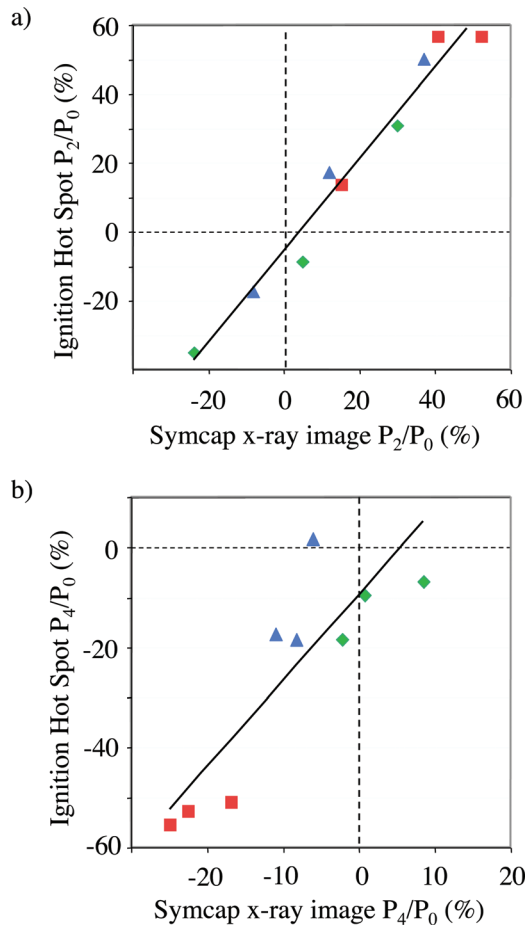
a)

b)

FIG. 28. (Color online) (a) Calculated (a) P_2/P_0 and (b) P_4/P_0 asymmetry for symmetry capsule versus ignition capsule core images for various imposed levels of flux asymmetry.

accomplished through a 500-μm diameter CH-tamped hole in the hohlraum by an array of 5–10 μm pinholes at 8–10 cm casting 12–15$\times$ magnification images onto a 4 stripline MCP providing 900 ps of continuous time coverage over 70 ps gate times. 3D Hydra simulations show that the hole is not expected to close appreciably before the bangtime at $\approx$16 ns, as witnessed experimentally during the 2009 hohlraum energetics campaign. Furthermore, representing 0.1% of the hohlraum wall area, it is a negligible source of asymmetry or loss. In addition, the bandpass is set by the filters at the back of the detector to avoid distortion of the images by potentially non-uniform transmission of the tamped CH that is subject to hydroinstability growth.

4. Accuracy

The expected core x-ray yields are of order a few J/sr over a few keV at 8 keV, which should provide 2%–3% statistical accuracy in decomposing core asymmetries/frame. Besides the equatorial view for assessing Legendre modes, Figure 26(a) shows that an axial imager will be fielded to check for azimuthal asymmetries such as an m = 4 on the capsule equator due to unexpected differential behavior between the 23.5° and 30° subcones in their absorption, x-ray conversion efficiency, or transmitted intensity, the latter for example due to cross-beam transfer.[116]

The data analysis consists of extracting contours from a set of images that span 200 (100) ps x-ray emission duration for convergence ratio 15 (30) implosions. The 20% emission contour appears best correlated to the shape of the hot spot-shell interface we are interested in and is at a sufficiently large perimeter and low contour level that higher modes such as P_6 could be resolved. In general, all contours will provide information. The extracted P_2 component can vary over the x-ray emission duration, but slowly enough that a 70 ps gate for the lower convergence implosions should be sufficient. In general, any P_2 swing means that the peak brightness image will have to be identified for a proper comparison to simulations. Accounting for a 20% variability in relative pinhole diameters and hence 40% in throughput, and in uncertainty in MCP gain profile corrections, we expect to be able to find the peak emission time to $\pm$15 ps, corresponding to a $\pm$3% uncertainty in core P_2 for a maximum plausible P_2 swing of 20%/100 ps. This is expected to be an upper limit as recent data [see later Fig. 30(b)] have shown far smaller P_2 swings. A typical tuning campaign would consist of varying the cone fraction by $\pm$10% and hohlraum length by $\pm$400 μm on separate shots to check sensitivities and interpolate to the optimal tuning. The goal of the symmetry capsule tuning campaign is to set the hohlraum length to $\pm$200 μm and the inner cone power ratio to $\pm$5% as listed in Table I. In addition, we will be able to confirm peak velocity from either the x-ray bangtime using the brightest gated x-ray camera image (to $\pm$50 ps when including cross-timing uncertainty) or nuclear bangtime. Finally, we will use these full-energy shots to assess the time-resolved >1.8 keV hard x-ray component using several dedicated high-energy Dante channels to an expected accuracy of $\pm$10%. This uncertainty translates to $\pm$8% in mix fraction. If the >1.8 keV fraction at peak power was measured to be say 30% greater than expected, then we would need to increase the ablator dopant concentration. In the recent experiments using CH(Ge) capsules driven by up to 290 eV hohlraums, the >1.8 keV fraction was indeed 30% larger than the 10.5% predicted using our baseline hohlraum models, leading to an 80% increase in Ge content designed into future targets.

We have computationally evaluated in 3D the fidelity in P_2 and P_4 core shape of symmetry capsules with respect to ignition capsules as shown in Figure 28 for a variety of intentionally mistuned drives. The simulation slopes show the expected higher sensitivity (1.5–2$\times$) for the higher convergence ratio ignition capsules. They also show that the correlation is typically 2$\times$ better than the $\pm$15% ignition core P_2 and P_4 required tuning accuracies and that there is no apparent systematic offset in P_2 but a potential +5% symmetry capsule offset in P_4 that Figure 25 and Table II equate to an $\approx$ +150 μm hohlraum length offset. In addition, 3D simulations show that the presence of random 3D drive asymmetries (usually at modes 1–4) dominated by residual quad-to-quad power imbalances (2% at peak power) only changes the perceived P_2 and P_4 asymmetries from the planned single equatorial line-of-sight by $\pm$3 and 2%, small compared to the $\pm$7.5% budgets (set by dividing the ignition capsule requirements of $\pm$15% by approximately the ratio of ignition to symmetry capsule convergences) shown in the last column in Table I.

5. Experimental validation of technique

The symmetry capsule became a robust technique for tuning both vacuum and gas-filled hohlraums[52] in Nova hohlraums where changing hohlraum length and/or beam pointing set the time-averaged single beam cone location near the P_2 node. At OMEGA, the NIC concept of setting symmetry by balancing opposite sign P_2 from different beam cones was first demonstrated,[122] followed by rudimentary beam cone phasing.[123] The expected simultaneous improvements in P_2 and P_4 control[124] and associated implosion performance[125] followed. Recently, symmetry tuning at OMEGA has been extended to demonstrating sensitivity to cone fraction using small NIC-relevant case-to-capsule ratios of <2.5 at radiation temperatures approaching 300 eV.[102,126] 1.2-mm-diameter OMEGA hohlraums illuminated with 260 eV, 1-ns-duration 21° and 59° cones imploded 560-μm-diameter 45-μm-thick CH(Ge$_{.02}$) capsules filled with a mixture of 36 atm D_2 + ^{3}He. Figure 29 displays the >4 keV 120-μm-diameter core images recorded and the core P_2 asymmetry extracted vs. 21.4° inner cone energy fraction for fixed total energy. The convergence ratio is small, $4\times$, attributed to the high level of penetrating preheat for these thickness capsules, leading to an inefficient exploding pusher compression mode for T_r above 220 eV[127] that will not exist for the thicker, NIC capsules driven by higher albedo, lower illumination intensity hohlraums. The symmetry goes to more positive P_2 as expected as the inner cone fraction is increased. Applying the same analysis for the P_2 variation versus cone fraction discussed earlier, for the $\Delta CF/CF = \pm.09/0.21$ applied here, diluted by F = 2 for a peak power albedo $\alpha = 0.75$ and amplified by the measured convergence -1 factor $= 3$, yields $\pm 16\%$ core P_2, close to the measured $\pm 10\%$. In addition, a $\pm 1\%$ statistical accuracy in P_2/P_0 was demonstrated as expected from photon counting statistics, similar to the measurement accuracy predictions for larger NIF capsules. These accuracies have been validated at NIF for 500–1000 kJ hohlraums driving convergence $15\times$ CH(Ge) symmetry capsules[128] imaged at 10 keV with 10 μm, 70 ps resolution [see Figure 30(a)]. Specifically, Figure 30(b) shows $\pm 1\%$ variability in core P_2 and P_4 symmetry between images taken within 50 ps of each other for a shot that met $\pm 5\%$ low mode symmetry requirements.

While the symmetry capsules for NIF are driven on a higher adiabat than ignition capsules due to shocks not being retimed when substituting 75 μm of DT fuel at 0.25 g/cc with 10 μm of Be at 1.85 g/cc, they are driven at lower adiabats than their counterparts at OMEGA. They have a higher in-flight aspect ratio (IFAR) and less mass remaining (comparing for example Figures 20 and 23), and hence will be prone to more feedthrough of hydroinstability growth from residual target imperfections.[129] The presence of a filltube and fillhole may lead to injection of a jet[130,131] of Cu-doped Be (or Ge-doped CH) deep in the He fill, locally increasing the x-ray Bremsstrahlung intensity and distorting the perceived core shape. Both jets traversing cores launched from surrogate fill-tubes and x-ray bright spots spatially correlated with known capsule surface imperfections were observed in 5 μm, 50 ps gated imaging OMEGA experiments using indirectly driven Ti-doped CH shells filled with D_2.[132] For the CH(Ge) design, we have already confirmed at NIF such signatures of penetration of the Ge dopant using a monochromatic version[133] of the gated imager designed for spectroscopic diagnosis[134,135] of Ge He-like and H-like lines at 10–12 keV. At the 1 MJ level,

a)

b)
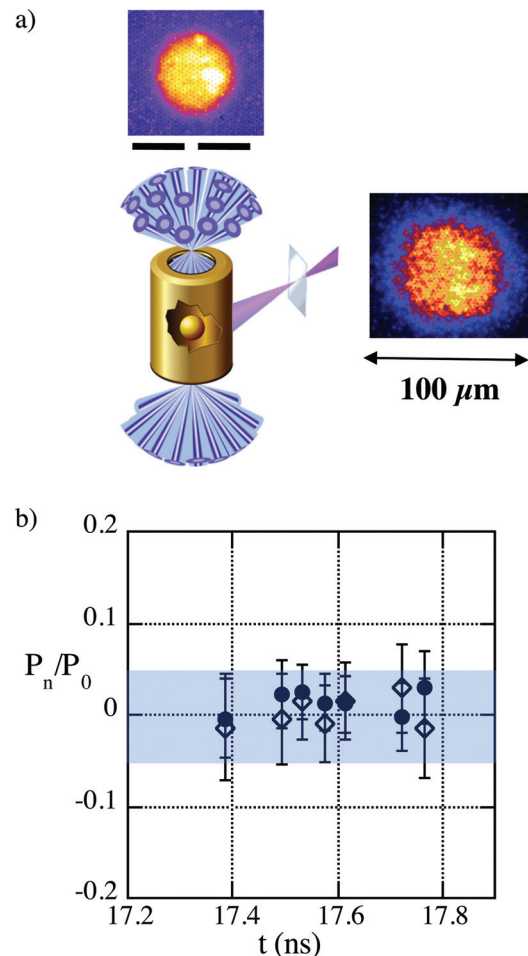
FIG. 30. (Color) (a) Gated 8-10 keV, 10 μm, 70 ps resolution x-ray images from pole and equator view of convergence ratio =15 CH capsules driven by 500 kJ 270 eV peak temperature NIF hohlraums. (b) Extracted P_2/P_0 (circles) and P_4/P_0 (diamonds) versus time.
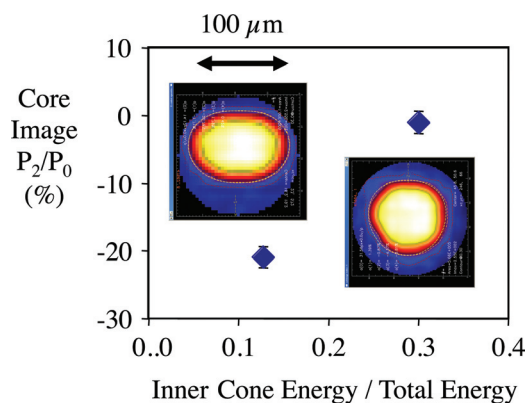

FIG. 29. (Color) OMEGA 5 keV core images and P_2/P_0 of emission shape versus inner cone fraction from imploded 50 atm fill CH capsule driven by 1 ns duration 270 eV peak hohlraum drive.

the bright spots caused by mixing of doped shell into the gas-fill penetrate ahead of the 20% contour used to infer core asymmetry and so provide an insignificant bias. If dopant penetration from target imperfections is problematic for core symmetry interpretation at higher drive levels, we will either thicken capsules or stay with reduced or truncated drives for symmetry measurements as mentioned earlier. The effect of mix between the inside of the Be and the He fill at stagnation on the perceived core asymmetry has been computationally investigated using different mix models. The simulations show different levels (5%–50%) of reduced sensitivity at 20% image contours to a given level of applied asymmetry when including plausible levels of mix, and only predict occasional systematic offsets for high levels of mix. Moreover, we will have indications of levels of mix from measured yields and core sizes (P_0).

III. SHOT PLAN

A. Shot goals

The goals of the capsule tuning campaign are to deliver the adjustable parameter value and uncertainty in that parameter, and to assess that shot-to-shot variability is as expected (look for unknown unknowns by repeating shots). An illustrative example output plot is shown in Figure 31 for the case of mass remaining vs. initial capsule thickness. A cluster of N shots at a nominal laser and target setting would be taken to assess the 1σ shot-to-shot variability and compare to expectations. The error bars on each data point are the 1σ random measurement error bars, which in the preceding sections have been shown to be less than or comparable to the expected data scatter. Since the standard error in the data scatter σ is $\approx \sigma/\sqrt{[2(N-1)]}$, we expect a 40% error in σ for a reasonable choice of N = 4, allowing us to detect scatter that is significantly greater or less than expected. The second step is to correct the data for known preshot shot-to-shot target variations and postshot shot-to-shot laser variations using precalculated sensitivities, examples of which were discussed in the prior sections. This should reduce the scatter in the data to just target and laser diagnostic metrology errors and errors in measuring the observable. In general, the mean

of this corrected data will be offset from the optimum value of the observable we are aiming for, precorrected for any known surrogacy offset. The second step is to gather another set of M data points, where in general M < N since data scatter has already been evaluated, for another value of the adjustable parameter that would bracket the optimum setting based on the precalculated slope sensitivity of the observable to the adjustable parameter. The optimum value of the adjustable parameter is then found by where the linear interpolation between the 2 datasets crosses the optimum value of the observable. The statistical accuracy in defining the optimum setting for the adjustable parameter will then be $= \sigma/\sqrt{(M+N)}$/mean slope. Finally, one will have to add in quadrature systematic errors due to uncertainty in surrogacy, physics of the technique, and calibrations, as detailed in the Appendix. The various contributions to the tuning accuracy for each of the adjustable laser and target parameters are shown in Figure 32 in terms of their variance normalized to the tuning budget listed in the last column in Table I. Many of these terms are themselves rms sums of various contributors outlined in Sec. II and in the Appendix, and some of them have already been validated or updated by the results of the 2009 hohlraum energetics campaign. We see that we meet the tuning accuracy budget for all parameters.

B. Shot sequence

The preferred tuning sequence follows closely the sequence of tuning techniques presented in Sec. II. The primary strategy is to first set early parameters in the laser pulse that are not affected by choices later in the pulse. This has the merit that truncated low environmental impact pulses can be used earlier in the life of the NIF laser. A proposed sequence is shown in Figure 33 as a matrix of rows of observables and columns of adjustable parameters. Green boxes on the principal diagonal designate the principal adjustable parameter set by a particular observable. Yellow boxes below the diagonal designate adjustable parameters set later that depend significantly on tuning performed earlier. Orange boxes above the diagonal designate adjustable parameters already set that can be affected significantly by the tuning performed later. If we understood those cross-couplings perfectly, then we could just correct as we proceed. However, there is uncertainty in the magnitude of these cross-couplings that will require looping back as shown schematically in Figure 33. The chronological tuning sequence has been tailored to minimize the ratio of cross-couplings above versus below the diagonal. The three principal reasons for looping back are as follows: A change in total foot laser power to set the first shock velocity will affect the relative inner vs. outer cone drive flux and hence the foot symmetry due to uncertainty in relative burn-through of the inner and outer beams. A change in hohlraum length to zero P_4 will affect P_2 and the total x-ray drive flux, and hence the shock velocity and by the connection above, the foot symmetry. A change in initial mass to set residual mass will affect the shock timing and the implosion velocity. We also tabulate in Figure 33 the calculated cross-coupling sensitivities normalized to the tuning
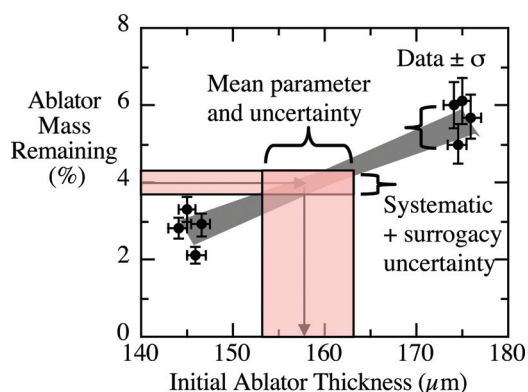

FIG. 31. (Color) Illustrative example of how a number of shots measuring ablator mass remaining will be used to check variability and to set the optimum associated target parameter, the initial ablator thickness, and its 1σ uncertainty.
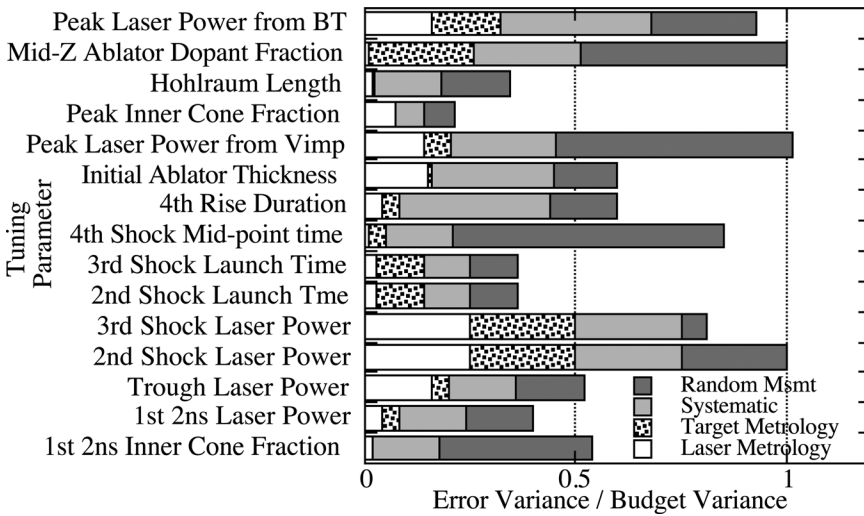
FIG. 32. Residual variances after tuning due to random measurement, systematic, target metrology, and laser diagnostic errors normalized to budget for each of the laser and target adjustable parameters.

accuracy budget. For example, $P_2/P_4 = -1$ means that changing the hohlraum length to change P_4 x% of its budgeted accuracy for P_4 will also change P_2 by x% of its budget. The fact that these cross-coupling terms are usually 1 or less is a reflection of the choice of target design and balancing of risk. A set of contingency shots has been identified. These include the following: increasing ablator dopant content to eliminate the VISAR window blanking by hard x-rays; testing if laser-plasma backscattering of the 30° beams hitting the keyhole cone are responsible for a measured change in drive at the capsule by using a dedicated shot to orient the cone towards the 30° quad equipped with a backscatter station; switching to uniform ablator doping if mix complicates the interpretation of the residual ablator mass; and using thinner symmetry capsules to tune out suspected P_2 symmetry swings during the 4th rise or earlier. Finally, a set of tuning shots are planned at larger

scale (i.e., 10% larger if we choose to go to a 1.7 MJ design) to eliminate as needed tuning extrapolation errors.

The chronological progress in increasing the mean ITF by tuning as shown schematically in Figure 3 has been quantified. A new figure-of-merit[7] that better characterizes the full ITF function with respect to the probability of ignition has been applied. The Margin over Uncertainty (M/U) is defined as the (Mean ITF − 1)/(1σ ITF + Rise in Prob. Ignition). For example, a final mean ITF of 2 with a 1σ in ITF distribution = 0.7 and a 15 to 85% rise in ignition probability = 0.2 ITF as shown in Figure 3 translates to an M/U = 1/0.9 = 1.1. To track the progression in M/U vs. shot number, we start with the initial 1σ uncertainties in the tuning parameters listed in column 5 of Table I which relate back to the ITF and uncertainty in ITF through column 2. We then update the uncertainties using the formulae in the Appendix as we follow the tuning strategy for each parameter as shown in Fig. 31 in the sequence shown in Figure 33. Finally, we include the impact of iterations, of checks of the surrogacy of shared observables such as core symmetry, bangtime, mass remaining, and peak implosion velocity using interleaved cryogenic-layered implosions,[48] and of scale-up checks. The first successful shot of a particular tuning campaign will eliminate the offset error, leaving measurement errors, data scatter, extrapolation, cross-coupling, and systematic errors due to uncertainties in surrogacy and scale-up. Successive shots taken under nominally the same conditions will reduce data scatter. The second set of shots varying the adjustable parameter will reduce extrapolation errors. Iterations will reduce cross-coupling errors, and cryogenically layered shots and scale-up shots eliminate some systematic errors. We can thus calculate the progression in Margin = ITF−1, uncertainty, M/U, and probability of ignition versus shot number for various scenarios. The first 40 shots have been largely dedicated to the hohlraum energetics campaign setting the go-forward hohlraum design after having evaluated and optimized the laser-plasma coupling efficiency; 40−60 shots is then deemed necessary for capsule tuning, followed by 15−20 shots for checking tuning fidelity and performance of cryogenically layered THD-filled capsules. Barring unexpected physics

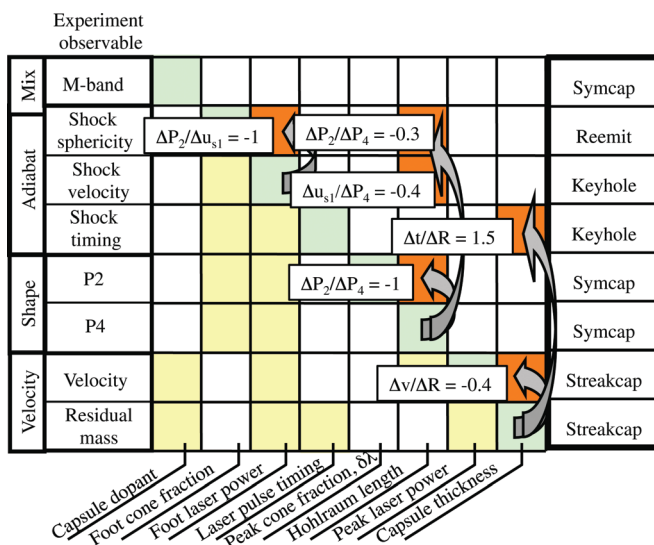FIG. 33. (Color) Matrix of shot tuning type displayed in chronological order from top to bottom versus laser or target parameter. Green boxes on diagonal mean that shot observable is affected by and sets that parameter, and of-diagonal yellow and orange boxes mean that shot is affected by that parameter but does not set it. Value in each orange box above diagonal is expected cross-coupling sensitivity normalized to error budget.

issues, this number of shots is predicted to reach an end point ITF > 1.7, M/U > 0.85 and probability of ignition on any given shot >85% as a necessary prelude to the first DT ignition experiment.

C. Contingency shots

A further set of shots are planned before or after the first ignition attempts if still required to isolate particular hohlraum or capsule physics not addressed directly by the tuning campaigns, principally fuel preheat and ablator mix into the fuel or hot spot. In the realm of preheat raising fuel adiabat, the 2009 results for 280 eV, 1 MJ drives infer up to 2% hot electron fractional preheat[136] from the Au wall Bremsstrahlung,[137] comparable to what is allowable depending on its exact timing with respect to shock break-out into the DT gas. A burst of suprahot electrons above a certain laser intensity threshold has been observed[138] during the initial laser-LEH window interaction on scaled OMEGA experiments, attributed to the two-plasmon decay instability.[139] The level of hot electrons during the foot of the pulse is principally a surrogacy issue for shock timing in liquid D_2 that would not mimic the solid DT shell pre-heat-induced expansion. It seems prudent to attempt a more direct measure of the level of hot electron preheat reaching the capsule fuel, especially since the hot electron production mechanisms can be directional. Prior results[140] have already demonstrated the feasibility of 30 keV x-ray imaging for viewing the hohlraum Bremsstrahlung as a measure of hot electron production. The new design will perform absolutely calibrated, moderate 300–400 μm spatial resolution (to discriminate capsule from hohlraum as seen through an LEH) $40-100$ keV imaging of the capsule Bremsstrahlung at discrete time periods in the pulse. This will be accomplished using a high energy calibrated[141] time-integrating Imaging Plate as detector and the truncated drives of the reemit capsule for the first 2 ns and the shock timing capsule for the 4th rise, culminating with the symmetry capsule for the full drive. A more advanced design would measure the in-flight fuel adiabat (essentially $1 +$ the ratio of T_e to the Fermi energy) by x-ray spectrally resolved Thomson scattering.[142] For the latter, recent x-ray scattering experiments[143] at OMEGA have demonstrated the feasibility of diagnosing imploding capsule conditions using the Compton downshifted feature from a 9 keV Zn He-alpha resonance probe line. In the realm of hydroinstability, the bright spots of CH(Ge) dopant material observed jetting into the symmetry capsule hot spots and recognition of increased sensitivity of CH (vs Be) to surface roughness or isolated defects have spurred designs to measure the ablation front Rayleigh-Taylor growth by in-flight x-ray face-on or side-on radiography.[144] In addition, preliminary designs exist for assessing the in-flight density differential between abla-tor and fuel (and hence the Atwood number and susceptibil-ity to ablator-fuel high-mode mix) using refraction-enhanced x-ray radiography.[145]

If a change in ablator material or hohlraum design is deemed necessary to either recover ignition margin from unfavorable physics or to optimize margin, then we would embark on a further capsule tuning campaign after having revalidated adequate hohlraum peak drive. The number of each type of tuning shot will be influenced by what we learn from the first campaign on reproducibility and level of surrogacy between the capsule tuning and cryogenically layered implosions.

IV. SUMMARY

A capsule performance optimization campaign has been presented with the goal of substantially increasing the proba-bility of ignition on NIF. The campaign will experimentally correct for residual uncertainties in the implosion and hohl-raum physics used in our radiation-hydrodynamic computa-tional models before proceeding to ignition experiments. The sensitivity to laser and target tuning parameters extracted from detailed hydrodynamic simulations have been derived quantitatively using simple analytic models. The chosen tuning techniques have been shown experimentally and computationally to meet the required sensitivity and ac-curacy. The tuning campaign plans include checks of repeat-ability, iterations to overcome residual cross-couplings and contingency shots. Finally, a set of experiments has been outlined for isolating if needed capsule implosion physics issues.

APPENDIX: ERROR BREAKDOWN

The total 1σ variability in either setting or getting the optimum value for any adjustable parameter for an ignition shot attempt is given by the following rms sum if we do not precompensate for known randomly distributed ignition tar-get variability $\sigma_{IgnTargetVar}$:

$$\sigma_{Total}^2 = \sigma_{Tuning}^2 + \sigma_{LaserVar}^2 + \sigma_{IgnTargetVar}^2 + \sigma_{IgnTargetMetr}^2,$$
(A1)

where $\sigma_{LaserVar}$ is the random rms variability in an ignition observable or parameter from the expected laser variability (e.g., power levels, cone balance) on any given ignition shot, $\sigma_{IgnTargetVar}$ is the random rms variability in an igni-tion observable or parameter expected from known ignition target variations (e.g., capsule thickness, hohlraum length), $\sigma_{IgnTargetMetr}$ is the random rms variability in an ignition observable or parameter expected from the residual ignition target metrology uncertainties (e.g., capsule thickness, dop-ant concentration), after precompensating for the known part of target variability, σ_{Tuning} is the 1σ uncertainty in an ignition observable or parameter based on residual errors in the experimental tuning. If we do precompensate, the $\sigma_{IgnTargetVar}$ term is removed.

The contribution discussed in this paper, the experimen-tal tuning portion of the variability in setting ignition param-eters, is itself the quadrature sum of the following:

$$\sigma_{Tuning}{}^2 = \sigma_{Random}{}^2 + \sigma_{Systematic}{}^2 + \sigma_{Sampling}{}^2 + \sigma_{Surrogacy}{}^2$$
$$+ \sigma_{Scaleup}{}^2, \tag{A2}$$

where $\sigma_{Systematic}$ is the estimated 1σ shot-to-shot repeatable errors in observables due to diagnostic and experimental uncertainties (e.g., calibration errors, LEH closure correction, cable compensation for Dante Tr), $\sigma_{Sampling}$ is the estimated systematic 1σ bias error due to limited FoV or sample size in time and space for observable (e.g., No 23° and 44° FABS, no symmetry tuning of 2nd and 3rd shock, wall vs capsule Tr sampling, the repeatable part of the azimuthal asymmetry), $\sigma_{Surrogacy}$ is the estimated 1σ shot-to-shot repeatable errors in the correction to an observable from known differences in hohlraum environment and/or surrogate capsule behavior (e.g., effect of patches and missing beams for re-emit), $\sigma_{Scaleup}$ is the estimated 1σ error in extrapolation correction to an observable if we choose to scale-up in laser energy and target size without checking tuning (e.g., transition from a tuned 1.3 MJ-scale to an $\approx 10\%$ larger 1.7 MJ-scale). σ_{Random} is the estimated 1σ shot-to-shot random variability in observables which breaks down further into

$$\sigma_{Random}{}^2 = \frac{\frac{\sigma_{Msmt}{}^2}{\#Chan.xView} + \sigma_{Statistical}{}^2 + \sigma_{LaserMetr}{}^2 + \sigma_{TargetMetr}{}^2}{\#Shots}, \tag{A3}$$

where the first term σ_{Msmt} is the random rms variability in observable per channel expected from the experimental measurement statistical uncertainties (e.g., shot noise/signal for one image (i.e., one channel) on GXD strip) that can be averaged over a number of equivalent channels and/or views. Of the remaining terms, $\sigma_{Statistical}$ is the random rms variability in observable per shot expected from having finite LoS (e.g., variability in P_2 observed due to 3D random power imbalances), $\sigma_{LaserMetr}$ is the random rms variability in observable expected from the residual laser diagnostic uncertainties (e.g., power and cone balance) after normalizing each data point postshot for the known part of laser variability, and $\sigma_{TargetMetr}$ is the random rms variability in observable expected from the residual tuning target metrology uncertainties (e.g., capsule thickness, hohlraum length), after normalizing each data point for the known part of the target variability.

[1] G. H. Miller, E. I. Moses, and C. R. Wuest, Nucl. Fusion **44**, 228 (2004).

[2] E. I. Moses, J. Phys.: Conf. Ser. **112**, 012003 (2008); J. D. Kilkenny, T. P. Bernat, B. A. Hammel, R. L. Kauffman, O. L. Landen, J. D. Lindl, B. J. Macgowan, J. A. Paisner, and H. T. Powell, Laser Part. Beams **17**, 159 (1999); J. D. Kilkenny, E. M. Campbell, J. D. Lindl, G. B. Logan, W. R. Meier, L. J. Perkins, J. A. Paisner, M. H. Key, H. T. Powell, R. L. McCrory, and W. Seka, Philos. Trans. R. Soc. London A **357**, 533 (1999).

[3] J. D. Lindl, Phys. Plasmas **2**, 3933 (1995); J. D. Lindl, P. Amendt, R. L. Berger, S. G. Glendinning, S. H. Glenzer, S. W. Haan, R. L. Kauffman, O. L. Landen, and L. J. Suter, Phys. Plasmas **11**, 339 (2004).

[4] L. J. Atherton, J. Phys.: Conf. **112**, 032063 (2008).

[5] C. A. Haynam, P. J. Wegner, J. M. Auerbach, M. W. Bowers, S. N. Dixit, G. V. Erbert, G. M. Heestand, M. A. Henesian, M. R. Hermann, K. S. Jancaitis, K. R. Manes, C. D. Marshall, N. C. Mehta, J. Menapace, E. Moses, J. R. Murray, M. C. Nostrand, C. D. Orth, R. Patterson, R. A. Sacks, M. J. Shaw, M. Spaeth, S. B. Sutton, W. H. Williams, C. C. Widmayer, R. K.

White, S. T. Yang, and B. M. Van Wonterghem, Appl. Opt. **46**, 3276 (2007).

[6] S. H. Glenzer, B. J. MacGowan, P. Michel, N. B. Meezan, L. J. Suter, S. N. Dixit, J. L. Kline, G. A. Kyrala, D. A. Callahan, E. L. Dewald, L. Divol, E. Dzenitis, M. J. Edwards, A. V. Hamza, C. A. Haynam, D. E. Hinkel, D. H. Kalantar, J. D. Kilkenny, O. L. Landen, J. D. Lindl, S. LePape, J. D. Moody, A. Nikroo, T. Parham, M. B. Schneider, R. P. J. Town, P. Wegner, K. Widmann, P. Whitman, B. K. F. Young, B. Van Wonterghem, J. E. Atherton, and E. I. Moses, Science **327**, 1228 (2010); N. B. Meezan, L. J. Atherton, D. A. Callahan, E. L. Dewald, S. Dixit, E. G. Dzenitis, M. J. Edwards, C. A. Haynam, D. E. Hinkel, O. S. Jones, O. Landen, R. A. London, P. A. Michel, J. D. Moody, J. L. Milovich, M. B. Schneider, C. A. Thomas, R. P. J. Town, A. L. Warrick, S. V. Weber, K. Widmann, S. H. Glenzer, L. J. Suter, B. J. MacGowan, J. L. Kline, G. A. Kyrala, and A. Nikroo, Phys. Plasmas **18**, 056304 (2010); S. H. Glenzer, B. J. MacGowan, N. B. Meezan, P. Adams, J. Alfonso, E. Alger, Z. Alherz, L. Alvarez, S. Alvarez, P. Amick, Phys. Rev. Lett. **106**, 085004 (2011).

[7] S. W. Haan, J. D. Lindl, D. A. Callahan, D. S. Clark, J. D. Salmonson, B. A. Hammel, L. J. Atherton, R. C. Cook, M. J. Edwards, S. Glenzer, A. V. Hamza, S. P. Hatchett, D. E. Hinkel, D. D. Ho, O. S. Jones, O. L. Landen, B. J. MacGowan, M. M. Marinak, J. L. Milovich, E. I. Moses, D. H. Munro, S. M. Pollaine, J. E. Ralph, H. F. Robey, B. K. Spears, P. T. Springer, L. J. Suter, C. A. Thomas, R. P. Town, S. V. Weber, D.C Wilson, G. Kyrala, M. C. Herrmann, R. E. Olson, K. Peterson, R. Vesey, D. D. Meyerhofer, A. Nikroo, H. L. Wilkens, H. Huang, and K. A. Moreno, Phys. Plasmas **18**, 051001 (2011).

[8] D. S. Clark, S. W. Haan, B. A. Hammel, J. D. Salmonson, D. A. Callahan, and R. P. J. Town, Phys. Plasmas **17**, 052703 (2010).

[9] S. W. Haan, M. C. Herrmann, T. R. Dittrich, A. J. Fetterman, M. M. Marinak, D. H. Munro, S. M. Pollaine, J. D. Salmonson, G. L. Strobel, and L. J. Suter, Phys. Plasmas **12**, 056316 (2005).

[10] T. C. Sangster, R. Betti, R. S. Craxton, J. A. Delettrez, D. H. Edgell, L. M. Elasky, V. Yu. Glebov, V. N. Goncharov, D. R. Harding, D. Jacobs-Perkins, R. Janezic, R. L. Keck, J. P. Knauer, S. J. Loucks, L. D. Lund, F. J. Marshall, R. L. McCrory, P. W. McKenty, D. D. Meyerhofer, P. B. Radha, S. P. Regan, W. Seka, W. T. Shmayda, S. Skupsky, V. A. Smalyuk, J. M. Soures, C. Stoeckl, B. Yaakobi, J. A. Frenje, C. K. Li, R. D. Petrasso, F. H. Séguin, J. D. Moody, J. A. Atherton, B. D. MacGowan, J. D. Kilkenny, T. P. Bernat, and D. S. Montgomery Phys. Plasmas **14**, 058101 (2007).

[11] D. C. Wilson, P. A. Bradley, N. M. Hoffman, F. J. Swenson, D. P. Smitherman, R. E. Chrien, R. W. Margevicius, D. J. Thoma, L. R. Foreman, J. K. Hoffer, S. R. Goldman, S. E. Caldwell, T. R. Dittrich, S. W. Haan, M. M. Marinak, S. M. Pollaine, and J. J. Sanchez, Phys. Plasmas **5**, 1953 (1998).

[12] T. R. Dittrich, S. W. Haan, M. M. Marinak, S. M. Pollaine, D. E. Hinkel, D. H. Munro, C. P. Verdon, G. L. Strobel, R. McEachern, R. C. Cook, C. C. Roberts, D. C. Wilson, P. A. Bradley, L. R. Foreman, and W. S. Varnum, Phys. Plasmas **6**, 2164 (1999).

[13] D. A. Callahan, D. E. Hinkel, R. L. Berger, L. Divol, S. N. Dixit, M. J. Edwards, S. W. Haan, O. S. Jones, J. D. Lindl, N. B. Meezan, P. A. Michel, S. M. Pollaine, L. J. Suter, R. P. J. Town, and P. A. Bradley, J. Phys.: Conf. Ser. **112**, 022021 (2008).

[14] A. Nikroo, K. C. Chen, M. L. Hoppe, H. Huang, J. R. Wall, H. Xu, M. W. McElfresh, C. S. Alford, R. C. Cook, J. C. Cooley, R. Fields, R. Hackenberg, R. P. Doerner, and M. Baldwin, Phys. Plasmas **13**, 056302 (2006).

[15] K. C. Chen, R. C. Cook, H. Huang, S. A. Letts, and A. Nikroo, Fusion Sci. Technol. **49**, 750 (2006).

[16] J. Biener, P. Mirkarimi, J. Tringe, S. Baker, Y. Wang, S. Kucheyev, N. Teslich, K. Wu, A. Hamza, C. Wild, E. Woerner, P. Koidl, K. Bruelne, and H. Fecht, Fusion Sci. Technol. **49**, 737 (2006).

[17] M. M. Marinak, S. W. Haan, T. R. Dittrich, R. E. Tipton, and G. B. Zimmerman, Phys. Plasmas **5**, 1125 (1998).

[18] S. W. Haan, M. C. Herrmann, P. A. Amendt, D. A. Callahan, T. R. Dittrich, M. J. Edwards, O. S. Jones, M. M. Marinak, D. H. Munro, S. M. Pollaine, J. D. Salmonson, B. K. Spears, and L. J. Suter, Fusion Sci. Technol. **49**, 553 (2006).

[19] S. W. Haan, P. A. Amendt, D. A. Callahan, T. R. Dittrich, M. J. Edwards, B. A. Hammel, D. D. Ho, O. S. Jones, J. D. Lindl, M. M. Marinak, D. H. Munro, S. M. Pollaine, J. D. Salmonson, B. K. Spears, and L. J. Suter, Fusion Sci. Technol. **51**, 509 (2007).

[20] S. W. Haan, M. C. Herrmann J. D. Salmonson, P. A. Amendt, D. A. Callahan, T. R. Dittrich, M. J. Edwards, O. S. Jones, M. M. Marinak, D. H.

Munro, S. M. Pollaine, B. K. Spears, and L. J. Suter, Eur. Phys. J. D **44**, 249 (2007).

[21] D. S. Clark, S. W. Haan, and J. D. Salmonson, Phys. Plasmas **15**, 056305 (2008).

[22] S. W. Haan, D. A. Callahan, M. J. Edwards, B. A. Hammel, D. D. Ho, O. S. Jones, J. D. Lindl, B. J. MacGowan, M. M. Marinak, D. H. Munro, S. M. Pollaine, J. D. Salmonson, B. K. Spears, and L. J. Suter, Fusion Sci. Technol. **55**, 227 (2009).

[23] N. B. Meezan, S. H. Glenzer, and L. J. Suter, J. Phys.: Conf. Ser. **112**, 022022 (2008).

[24] D. H. Froula, D. Bower, M. Chrisp, S. Grace, J. H. Kamperschroer, T. M. Kelleher, R. K. Kirkwood, B. MacGowan, T. McCarville, N. Sewall, F. Y. Shimamoto, S. J. Shiromizu, B. Young, and S. H. Glenzer, Rev. Sci. Instrum. **75**, 4168 (2004).

[25] A. J. Mackinnon, T. McCarville, K. Piston, C. Niemann, G. Jones, I. Reinbachs, R. Costa, J. Celeste, G. Holtmeier, R. Griffith, R. Kirkwood, B. MacGowan, S. H. Glenzer, and M. R. Latta, Rev. Sci. Instrum. **75**, 4183 (2004).

[26] J. W. McDonald, R. L. Kauffman, J. R. Celeste, M. A. Rhodes, F. D. Lee, L. J. Suter, A. P. Lee, J. M. Foster, and G. Slark, Rev. Sci. Instrum. **75**, 3753 (2004).

[27] E. L. Dewald, K. M. Campbell, R. E. Turner, J. P. Holder, O. L. Landen, S. H. Glenzer, R. L. Kauffman, L. J. Suter, M. Landon, M. Rhodes, and D. Lee, Rev. Sci. Instrum. **75**, 3759 (2004).

[28] J. A. Oertel, R. Aragonez, T. Archuleta, C. Barnes, L. Casper, V. Fatherley, T. Heinrichs, R. King, D. Landers, F. Lopez, P. Sanchez, G. Sandoval, L. Schrank, P. Walsh, P. Bell, M. Brown, R. Costa, J. Holder, S. Montelongo, and N. Pederson, Rev. Sci. Instrum. **77**, 10E308 (2006).

[29] E. L. Dewald, L. J. Suter, O. L. Landen, J. P. Holder, J. Schein, F. D. Lee, K. M. Campbell, F. A. Weber, D. G. Pellinen, M. B. Schneider, J. R. Celeste, J. W. McDonald, J. M. Foster, C. Niemann, A. J. Mackinnon, S. H. Glenzer, B. K. Young, C. A. Haynam, M. J. Shaw, R. E. Turner, D. Froula, R. L. Kauffman, B. R. Thomas, L. J. Atherton, R. E. Bonanno, S. N. Dixit, D. C. Eder, G. Holtmeier, D. H. Kalantar, A. E. Koniges, B. J. MacGowan, K. R. Manes, D. H. Munro, J. R. Murray, T. G. Parham, K. Piston, B. M. Van Wonterghem, R. J. Wallace, P. J. Wegner, P. K. Whitman, B. A. Hammel, and E. I. Moses, Phys. Rev. Lett. **95**, 215004 (2005); E. L. Dewald, O. L. Landen, L. J. Suter, J. Schein, J. Holder, K. Campbell, S. H. Glenzer, J. W. McDonald, C. Niemann, A. J. Mackinnon, M. S. Schneider, C. Haynam, D. Hinkel, and B. A. Hammel, Phys. Plasmas **13**, 056315 (2006).

[30] O. L. Landen, S. H. Glenzer, D. H. Froula, E. L. Dewald, L. J. Suter, M. B. Schneider, D. E. Hinkel, J. C. Fernandez, J. L. Kline, S. R. Goldman, *et al.*, Eur. Phys. J. D **44**, 273 (2007).

[31] E. M. Campbell, J. T. Hunt, E. S. Bliss, D. R. Speck, and R. P. Drake, Rev. Sci. Instrum. **57**, 2101 (1986).

[32] J. M. Soures, R. L. McCrory, C. P. Verdon, A. Babushkin, R. E. Bahr, T. R. Boehly, R. Boni, D. K. Bradley, D. L. Brown, R. S. Craxton, J. A. Delettrez, W. R. Donaldson, R. Epstein, P. A. Jaanimagi, S. D. Jacobs, K. Kearney, R. L. Keck, J. H. Kelly, T. J. Kessler, R. L. Kremens, J. P. Knauer, S. A. Kumpan, S. A. Letzring, D. J. Lonobile, S. J. Loucks, L. D. Lund, F. J. Marshall, P. W. McKenty, D. D. Meyerhofer, S. F. B. Morse, A. Okishev, S. Papernov, G. Pien, W. Seka, R. Short, M. J. Shoup III, M. Skeldon, S. Skupsky, A. W. Schmid, D. J. Smith, S. Swales, M. Wittman, and B. Yaakobi, Phys. Plasmas **3**, 2108 (1996); T. R. Boehly, D. L. Brown, R. S. Craxton, R. L. Keck, J. P. Knauer, J. H. Kelly, T. J. Kessler, S. A. Kumpan, S. J. Bucks, S. A. Letzring, F. J. Marshall, R. L. McCrory, S. F. B. Morse, W. Seka, J. M. Sowes, and C. P. Verdon, Opt. Commun. **133**, 495 (1997).

[33] E. Dattolo, L. Suter, M. C. Monteil, J. P. Jadaud, N. Dague, S. Glenzer, R. Turner, D. Juraszek, B. Lasinski, C. Decker, O. Landen, and B. MacGowan, Phys. Plasmas **8**, 260 (2001).

[34] J. L. Bourgade, P. Stemmler, G. Oudot, V. Tassin, G. Pien, O. L. Landen, C. Sorce, V. Tran, and K. Widmann, "Survey of the active components of the x-Ray broad band spectrometer DMX," J. Instrum. (submitted).

[35] D. Besnard, J. Phys.: Conf. Ser. **112**, 012004 (2008).

[36] J. L. Bourgade, B. Villette, J. L. Bocher, J. Y. Boutin, S. Chiche, N. Dague, D. Gontier, J. P. Jadaud, B. Savale, R. Wrobel, and R. Turner, Rev. Sci. Instrum. **72**, 1173 (2001).

[37] J. L. Kline, K. Widmann, A. Warrick, R. E. Olson, C. A. Thomas, A. S. Moore, L. J. Suter, O. Landen, D. Callahan, S. Azevedo, J. Liebman, S. H. Glenzer, A. Conder, S. N. Dixit, P. Torres III, V. Tran, E. L. Dewald, J. Kamperschroer, L. J. Atherton, R. Beeler Jr., L. Berzins, J. Celeste,

C. Haynam, W. Hsing, D. Larson, B. J. MacGowan, D. Hinkel, D. Kalantar, R. Kauffman, J. Kilkenny, N. Meezan, M. D. Rosen, M. Schneider, E. A. Williams, S. Vernon, R. J. Wallace, B. Van Wonterghem, and B. K. Young, Rev. Sci. Instrum. **81**, 10E 321 (2010).

[38] J. L. Kline, S. H. Glenzer, R. E. Olson, L. J. Suter, K. Widmann, D. A. Callahan, S. N. Dixit, C. A. Thomas, D. E. Hinkel, E. A. Williams, A. Moore, J. Celeste, E. Dewald, W. W. Hsing, A. Warrick, J. Atherton, S. Azevedo, R. Beeler, R. Berger, A. Conder, L. Divol, C. A. Haynam, D. H. Kalantar, R. Kauffman, G. A. Kyrala, J. Kilkenny, J. Liebman, S. LePape, D. Larson, N. B. Meezan, P. Michel, J. Moody, M. D. Rosen, M. B. Schneider, B. Van Wonterghem, R. J. Wallace, B. K. Young, O. L. Landen, and B. J. MacGowan, Phys. Rev. Lett. **106**, 085003 (2011).

[39] J. C. Fernández, S. R. Goldman, J. L. Kline, E. S. Dodd, C. Gautier, G. P. Grim, B. M. Hegelich, D. S. Montgomery, N. E. Lanier, H. Rose, D. W. Schmidt, J. B. Workman, D. G. Braun, E. L. Dewald, O. L. Landen, K. M. Campbell, J. P. Holder, A. J. MacKinnon, C. Niemann, J. Schein, B. K. Young, J. R. Celeste, S. N. Dixit, D. C. Eder, S. H. Glenzer, C. A. Haynam, D. Hinkel, D. Kalantar, J. Kamperschroer, R. L. Kauffman, R. Kirkwood, A. E. Koniges, F. D. Lee, B. J. MacGowan, K. R. Manes, J. W. McDonald, M. B. Schneider, M. J. Shaw, L. J. Suter, R. J. Wallace, F. A. Weber, and J. L. Kaae, Phys. Plasmas **13**, 056319 (2006).

[40] S. P. Regan, T. C. Sangster, D. D. Meyerhofer, W. Seka, R. Epstein, S. J. Loucks, R. L. McCrory, C. Stoeckl, V. Yu. Glebov, O. S. Jones, D. A. Callahan, O. A. Amendt, N. B. Meezan, L. J. Suter, M. D. Rosen, O. L. Landen, E. L. Dewald, S. H. Glenzer, C. Sorce, S. Dixit, R. E. Turner, and B. J. MacGowan, J. Phys.: Conf. **112**, 022077 (2008).

[41] S. H. Glenzer, P. Arnold, G. Bardsley, R. L. Berger, G. Bonanno, T. Borger, M. Bowers, R. Bryant, S. Buckman, S. C. Burkhart, K. Campbell, M. P. Chrisp, B. I. Cohen, C. Constantin, F. Cooper, J. Cox, E. Dewald, L. Divol, S. Dixit, J. Duncan, D. Eder, J. Edwards, G. Erbert, B. Felker, J. Fornes, G. Frieders, D. H. Froula, S. D. Gardner, C. Gates, M. Gonzalez, S. Grace, G. Gregori, A. Greenwood, R. Griffith, T. Hall, B. A. Hammel, C. Haynam, G. Heestand, M. Henesian, G. Hermes, D. Hinkel, J. Holder, F. Holdner, G. Holtmeier, W. Hsing, S. Huber, T. James, S. Johnson, O. S. Jones, D. Kalantar, J. H. Kamperschroer, R. Kauffman, T. Kelleher, J. Knight, R. K. Kirkwood, W. L. Kruer, W. Labiak, O. L. Landen, A. B. Langdon, S. Langer, D. Latray, A. Lee, F. D. Lee, D. Lund, B. MacGowan, S. Marshall, J. McBride, T. McCarville, L. McGrew, A. J. Mackinnon, S. Mahavandi, K. Manes, C. Marshall, J. Menapace, E. Mertens, N. Meezan, G. Miller, S. Montelongo, J. D. Moody, E. Moses, D. Munro, J. Murray, J. Neumann, M. Newton, E. Ng, C. Niemann, A. Nikitin, P. Opsahl, E. Padilla, T. Parham, G. Parrish, C. Petty, M. Polk, C. Powell, I. Reinbachs, V. Rekow, R. Rinnert, B. Riordan, M. Rhodes, V. Roberts, H. Robey, G. Ross, S. Sailors, R. Saunders, M. Schmitt, M. B. Schneider, S. Shiromizu, M. Spaeth, A. Stephens, B. Still, L. J. Suter, G. Tietbohl, M. Tobin, J. Tuck, B. M. Van Wonterghem, R. Vidal, D. Voloshin, R. Wallace, P. Wegner, P. Whitman, E. A. Williams, K. Williams, K. Winward, K. Work, B. Young, P. E. Young, P. Zapata, R. E. Bahr, W. Seka, J. Fernandez, D. Montgomery, and H. Rose, Nucl. Fusion **44**, S185 (2004); S. H. Glenzer, D. H. Froula, L. Divol, M. Dorr, R. L. Berger, S. Dixit, B. A. Hammel, C. Haynam, J. A. Hittinger, J. P. Holder, O. S. Jones, D. H. Kalantar, O. L. Landen, A. B. Langdon, S. Langer, B. J. MacGowan, A. J. Mackinnon, N. Meezan, E. I. Moses, C. Niemann, C. H. Still, L. J. Suter, R. J. Wallace, E. A. Williams, and B. K. F. Young, Nat. Phys. **3**, 709 (2007).

[42] S. N. Dixit, M. D. Feit, M. D. Perry, and H. T. Powell, Opt. Lett. **21**, 1715 (1996).

[43] S. N. Dixit, D. Munro, J. R. Murray, M. Nostrand, P. J. Wegner, D. Froula, C. A. Haynam, and B. J. MacGowan, J. Phys. **133**, 717 (2006).

[44] O. L. Landen, T. R. Boehly, D. K. Bradley, D. G. Braun, D. A. Callahan, P. M. Celliers, G. W. Collins, E. L. Dewald, L. Divol, S. H. Glenzer, A. Hamza, D. G. Hicks, N. Hoffman, N. Izumi, O. S. Jones, R. K. Kirkwood, G. A. Kyrala, P. Michel, J. Milovich, D. H. Munro, A. Nikroo, R. E. Olson, H. F. Robey, B. K. Spears, C. A. Thomas, S. V. Weber, D. C. Wilson, M. M. Marinak, L. J. Suter, B. A. Hammel, D. D. Meyerhofer, J. Atherton, J. Edwards, S. W. Haan, J. D. Lindl, B. J. MacGowan, and E. I. Moses, Phys. Plasmas **17**, 05631 (2010).

[45] G. B. Zimmerman and W. L. Kruer, Comments Plasma Phys. Controlled Fusion **2**, 51 (1975).

[46] M. M. Marinak, G. D. Kerbel, N. A. Gentile, O. Jones, D. Munro, S. Pollaine, T. R. Dittrich, and S. W. Haan, Phys. Plasmas **8**, 2275 (2001).

[47] T. C. Sangster, R. L. McCrory, V. N. Goncharov, D. R. Harding, S. J. Loucks, P. W. McKenty, D. D. Meyerhofer, S. Skupsky, B. Yaakobi, B.

J. MacGowan, L. J. Atherton, B. A. Hammel, J. D. Lindl, E. I. Moses, J. L. Porter, M. E. Cuneo, M. K. Matzen, C. W. Barnes, J. C. Fernandez, D. C. Wilson, J. D. Kilkenny, T. P. Bernat, A. Nikroo, B. G. Logan, S. Yu, R. D. Petrasso, J. D. Sethian, and S. Obenschain Nucl. Fusion **47**, S686 (2007).,

[48]M. J. Edwards, L. J. Atherton, D. L. Bleuel, D. K. Bradley, D. A. Callahan, C. J. Cerjan, D. Clark, G. W. Collins, J. E. Fair, R. J. Fortner, S. H. Glenzer, S. W. Haan, A. V. Hamza, S. P. Hatchett, B. Jacoby, O. S. Jones, J. A. Koch, B. J. Kozioziemski, O. L. Landen, R. Lerche, J. D. Lindl, B. J. MacGowan, A. J. MacKinnon, E. R. Mapoles, M. M. Marinak, M. Moran, E. I. Moses, D. H. Munro, D. H. Schneider, S. M. Sepke, D. A. Shaughnessy, B. K. Spears, P. T. Springer, R. Tommasini, R. Betti, T. R. Boehly, T. C. Sangster, V. Yu. Glebov, P. W. McKenty, S. P. Regan, D. H. Edgell, J. P. Knauer, C. Stoeckl, D. R. Harding, G. Grim, H. W. Herrman, G. Kyrala, M. Wilke, D. C. Wilson, J. Frenje, R. Petrasso, K. Moreno, H. Huang, K. C. Chen, E. Giraldez, J. D. Kilkenny, M. Mauldin, N. Hein, M. Hoppe, A. Nikroo, and R. Leeper, Phys. Plasmas **18**, 051003 (2011).

[49]L. J. Suter, A. A. Hauer, L. V. Powers, D. B. Ress, N. Delamater, W. W. Hsing, O. L. Landen, A. R. Thiessen, and R. E. Turner, Phys. Rev. Lett. **73**, 2328 (1994); S. H. Glenzer, L. J. Suter, R. E. Turner, B. J. MacGowan, K. G. Estabrook, M. A. Blain, S. N. Dixit, B. A. Hammel, R. L. Kauffman, R. K. Kirkwood, O. L. Landen, M.-C. Monteil, J. D. Moody, T. J. Orzechowski, D. M. Pennington, G. F. Stone, and T. L. Weiland, Phys. Rev. Lett. **80**, 2845 (1998).

[50]D. K. Bradley, D. G. Braun, S. G. Glendinning, M. J. Edwards, J. L. Milovich, C. M. Sorce, G. W. Collins, S. W. Haan, R. H. Page, R. J. Wallace, and J. L. Kaae, Phys. Plasmas **14**, 056313 (2007).

[51]O. L. Landen, D. K. Bradley, D. G. Braun, V. A. Smalyuk, D. G. Hicks, P. M. Celliers, S. Prisbrey, R. Page, T. R. Boehly, S. W. Haan, D. H. Munro, R. G. Wallace, A. Nikroo, A. Hamza, J. Biener, C. Wild, E. Woerner, R. E. Olson, G. A. Rochau, M. Knudson, D. C. Wilson, H. F. Robey, G. W. Collins, D. Ho, J. Edwards, M. M. Marinak, B. A. Hammel, D. D. Meyerhofer, and B. J. MacGowan, J. Phys.: Conf. **112**, 022004 (2008).

[52]N. D. Delamater, E. L. Lindman, G. R. Magelssen, B. H. Failor, T. J. Murphy, A. A. Hauer, P. Gobby, J. B. Moore, V. Gomez, K. Gifford, R. L. Kauffman, O. L. Landen, B. A. Hammel, G. Glendinning, L. V. Powers, L. J. Suter, S. Dixit, R. R. Peterson, and A. L. Richard, Phys. Plasmas **7**, 1609 (2000).

[53]M. D. Knudson, D. L. Hanson, J. E. Bailey, C. A. Hall, J. R. Asay, and W. W. Anderson, Phys. Rev. Lett. **87**, 225501 (2001); D. G. Hicks, T. R. Boehly, P. M. Celliers, J. H. Eggert, S. J. Moon, D. D. Meyerhofer, and G. W. Collins, Phys Rev. B **79**, 014112 (2009).

[54]F. J. Rogers, Phys. Plasmas **7**, 51 (2000).

[55]K. Eidmann, I. B. Foldes, Th. Lower, J. Massen, R. Sigel, G. D. Tsakiris, S. Witkowski, H. Nishimura, Y. Kato, T. Endo, H. Shiraga, M. Takagi, and S. Nakai, Phys. Rev. E **52**, 6703 (1995); I. B. Foldes, K. Eidmann, Th. Lower, J. Massen, R. Sigel, G. D. Tsakiris, S. Witkowski, H. Nishimura, T. Endo, H. Shiraga, M. Takagi, Y. Kato, and S. Nakai, Phys. Rev E **50**, R690 (1994).

[56]M. D. Rosen, Phys. Plasmas **5**, 1803 (1996).

[57]Y. T. Lee and R. M. More, Phys. Fluids **27**, 1273 (1984).

[58]P. A. Sterne, S. B. Hansen, B. G. Wilson, and W. A. Isaacs, High Energy Density Phys. **3**, 278 (2007); B. Wilson, V. Sonnad, P. Sterne, W. Isaacs, J. Quant. Spectrosc. Radiat. Transf. **99**, 658 (2006).

[59]R. E. Olson, R. J. Leeper, S. C. Dropinski, L. P. Mix, G. A. Rochau, S. H. Glenzer, O. S. Jones, L. J. Suter, J. L. Kaae, C. H. Shearer, and J. N. Smith, Rev. Sci. Instrum. **74**, 2186 (2003).

[60]E. L. Dewald, M. Rosen, S. H. Glenzer, L. J. Suter, F. Girard, J. P. Jadaud, J. Schein, C. Constantin, F. Wagon, G. Huser, P. Neumayer, and O. L. Landen, Phys. Plasmas **15**, 072706 (2008); F. Ze, S. H. Langer, R. L. Kauffman, J. D. Kilkenny, O. Landen, D. Ress, M. D. Rosen, L. J. Suter, R. J. Wallace, and J. D. Wiedwald, Phys. Plasmas **4**, 778 (1997).

[61]O. S. Jones, S. H. Glenzer, L. J. Suter, R. E. Turner, K. M. Campbell, E. L. Dewald, B. A. Hammel, R. L. Kauffman, O. L. Landen, M. D. Rosen, R. J. Wallace, and F. A. Weber, Phys. Rev. Lett. **93**, 065002 (2004).

[62]J. Schein, O. Jones, M. Rosen, E. Dewald, S. Glenzer, J. Gunther, B. Hammel, O. Landen, L. Suter, and R. Wallace, Phys. Rev. Lett. **98**, 175003 (2007); O. S. Jones, J. Schein, M. D. Rosen, L. J. Suter, R. J. Wallace, E. L. Dewald, S. H. Glenzer, K. M. Campbell, J. Gunther, B. A. Hammel, O. L. Landen, C. M. Sorce, R. E. Olson, G. A. Rochau, H. L. Wilkens, J. L. Kaae, J. D. Kilkenny, A. Nikroo, and S. P. Regan, Phys. Plasmas **14**, 056311 (2007).

[63]N. B. Meezan, R. L. Berger, L. Divol, D. H. Froula, D. E. Hinkel, O. S. Jones, R. A. London, J. D. Moody, M. M. Marinak, C. Niemann, C. P. B. Neumayer, S. T. Prisbrey, J. S. Ross, E. A. Williams, S. H. Glenzer, and L. J. Suter, Phys. Plasmas **14**, 056304 (2007).

[64]H. F. Robey, T. S. Perry, H.-S. Park, P. Amendt, C. M. Sorce, S. M. Compton, K. M. Campbell, and J. P. Knauer, Phys. Plasmas **12**, 072701 (2005).

[65]R. E. Olson, R. J. Leeper, A. Nobile, J. A. Oertel, G. A. Chandler, K. Cochrane, S. C. Dropinski, S. Evans, S. W. Haan, J. L. Kaae, J. P. Knauer, K. Lash, L. P. Mix, A. Nikroo, G. A. Rochau, G. Rivera, C. Russell, D. Schroen, R. J. Sebring, D. L. Tanner, R. E. Turner, and R. J. Wallace, Phys. Plasmas **11**, 2778 (2004).

[66]R. E. Olson, R. J. Leeper, A. Nobile, and J. A. Oertel, Phys. Rev. Lett. **91**, 235002 (2003).

[67]B. A. Hammel, S.W. Haan, D. S. Clark, M. J. Edwards, S. H. Langer, M. M. Marinak, M. V. Patel, J. D. Salmonson, and H. A. Scott, High Energy Density Phys. **6**, 171 (2010).

[68]B. A. Hammel, M. J. Edwards, S. W. Haan, M. M. Marinak, M. Patel, H. Robey, and J. Salmonson, J. Phys.: Conf. **112**, 022007 (2008).

[69]N. D. Delamater, G. R. Magelssen, and A. A. Hauer, Phys. Rev. E **53**, 5240 (1996); G. R. Magelssen, N. D. Delamater, E. L. Lindman, and A. A. Hauer, Phys. Rev. E **57**, 4663 (1998).

[70]T. R. Boehly, D. Munro, P. M. Celliers, R. E. Olson, D. G. Hicks, V. N. Goncharov, G. W. Collins, H. F. Robey, S. X. Hu, J. A. Morozas, T. C. Sangster, O. L. Landen, and D. D. Meyerhofer, Phys. Plasmas **16**, 056302 (2009).

[71]A. A. Hauer, L. Suter, N. Delamater, D. Ress, L. Powers, G. Magelssen, D. Harris, O. Landen, E. Lindman, W. Hsing, D. Wilson, and P. Amendt, Phys. Plasmas **2**, 672 (1995).

[72]D. G. Hicks, B. K. Spears, D. G. Braun, R. E. Olson, C. M. Sorce, P. M. Celliers, G. W. Collins, and O. L. Landen, Rev. Sci. Instrum. **81**, 10E304 (2010); D. G. Hicks, B. K. Spears, D. G. Braun, R. E. Olson, C. M. Sorce, P. M. Celliers, G. W. Collins, and O. L. Landen, Phys. Plasmas **17**, 102703 (2010).

[73]B. Spears, D. Hicks, C. Velsko, M. Stoyer, H. Robey, D. Munro, S. Haan, O. Landen, A. Nikroo, and H. Huang, J. Phys.: Conf. Ser. **112**, 022003 (2008).

[74]N. M. Hoffman, D. C. Wilson, and G. A. Kyrala, Rev. Sci. Instrum. **77**, 10E705 (2006); N. M. Hoffman, D. C. Wilson, M. J. Edwards, D. H. Kalantar, G. A. Kyrala, S. R. Goldman, S. V. Weber, N. Izumi, D. A. Callahan, N. Meezan, N. D. Delamater, I. L. Tregillis, M. J. Schmitt, P. A. Bradley, A. Seifter, O. S. Jones, J. L. Milovich, and C. A. Thomas, J. Phys.: Conf. Ser. **112**, 022075 (2008).

[75]S. M. Pollaine, D. K. Bradley, O. L. Landen, R. J. Wallace, O. S. Jones, P. A. Amendt, L. J. Suter, and R. E. Turner, Phys. Plasmas **8**, 2357 (2001); R. K. Kirkwood, J. Milovich, D. K. Bradley, M. Schmitt, S. R. Goldman, D. H. Kalantar, D. Meeker, O. S. Jones, S. M. Pollaine, P. A. Amendt, E. Dewald, J. Edwards, O. L. Landen, and A. Nikroo, Phys. Plasmas **16**, 012702 (2009).

[76]N. Delamater, P. Bradley, G. Magelssen, and D. Wilson, Rev. Sci. Instrum. **77**, 10E 302 (2006).

[77]F. Ze, R. L. Kauffman, J. D. Kilkenny, J. Wiedwald, P. M. Bell, R. Hanks, J. Stewart, D. Dean, J. Bower, and R. Wallace, Rev. Sci. Instrum. **63**, 5124 (1992).

[78]D. H. Cohen, O. L. Landen, and J. J. MacFarlane, Phys. Plasmas **12**, 122703 (2005).

[79]K. M. Campbell, F. A. Weber, E. L. Dewald, S. H. Glenzer, O. L. Landen, R. E. Turner, and P. A. Waide, Rev. Sci. Instrum. **75**, 3768 (2004).

[80]F. Girard, L. Suter, O. Landen, D. Munro, S. Regan, and J. Kline, Rev. Sci. Instrum. **80**, 063104 (2009).

[81]D. C. Eder, A. E. Koniges, O. L. Landen, N. D. Masters, A. C. Fisher, O. S. Jones, T. I. Suratwala, and L. J. Suter, J. Phys.: Conf. Ser. **112**, 032023 (2008).

[82]A. L. Meadowcroft, C. D. Bentley, and E. N. Stott, Rev. Sci. Instrum. **79**, 113102 (2008).

[83]E. L. Dewald, J. Milovich, J. Edwards, C. Thomas, R. Kirkwood, D. Meeker, O. Jones, N. Izumi, and O. L. Landen, Rev. Sci. Instrum. **79**, 10E903 (2008).

[84]E. Dewald, J. Milovich, C. Thomas, S. Glenn, J. Kline, R. Prasad, and O. L. Landen, Bull. Am. Phys. Soc. **54**, 28 (2009); E. Dewald, J. Milovich, C. Thomas, J. Kline, C. Sorce, S. Glenn, and O. L. Landen, "Experimental demonstration of early time, hohlraum radiation symmetry tuning for indirect drive ignition experiments," Phys. Plasmas (submitted).

[85]M. A. Knudson, Bull. Am. Phys. Soc. **51**, 340 (2006).

[86] D. H. Munro, P. M. Celliers, G. W. Collins, D. M. Gold, L. B. D. Silva, S. W. Haan, R. C. Cauble, B. A. Hammel, and W. W. Hsing, Phys. Plasmas **8**, 2245 (2001).

[87] T. R. Boehly, D. G. Hicks, P. M. Celliers, T. J. B. Collins, R. Earley, J. H. Eggert, D. Jacobs-Perkins, S. J. Moon, E. Vianello, D. D. Meyerhofer, and G. W. Collins, Phys. Plasmas **11**, L49 (2004).

[88] P. M. Celliers, D. K. Bradley, G. W. Collins, D. G. Hicks, T. R. Boehly, and W. J. Armstrong, Rev. Sci. Instrum. **75**, 4916 (2004); R. M. Malone, J. R. Bower, G. A. Capelle, J. R. Celeste, P. M. Celliers, B. C. Frogget, R. L. Guyton, M. I. Kaufman, G. A. Lare, T. L. Lee, B. J. MacGowan, S. Montelongo, E. W. Ng, T. L. Thomas, Jr., T. W. Tunnell, and P. W. Watts, Proc. SPIE **5523**, 148 (2004).

[89] H. F. Robey, D. H. Munro, B. K. Spears, M. M. Marinak, O. S. Jones, M. V. Patel, S. W. Haan, J. D. Salmonson, O. L. Landen, T. R. Boehly, and A. Nikroo, J. Phys.: Conf. **112**, 022078 (2008).

[90] P. A. Jaanimagi, R. Boni, D. Butler, S. Ghosh, W. R. Donaldson, and R. L. Keck, Proc. SPIE **5580**, 408 (2005).

[91] P. A. Jaanimagi, L. DaSilva, G. G. Gregory, C. Hestdalen, C. D. Kiikka, R. Kotmel, and M. C. Richardson, Rev. Sci. Instrum. **57**, 2189 (1986).

[92] W. Theobald, J. E. Miller, T. R. Boehly, E. Vianello, D. D. Meyerhofer, T. C. Sangster, J. Eggert, and P. M. Celliers, Phys. Plasmas **13**, 122702 (2006).

[93] R. L. Kauffman, L. J. Suter, C. B. Darrow, J. D. Kilkenny, H. N. Kornblum, D. S. Montgomery, D. W. Phillion, M. D. Rosen, A. R. Theissen, R. J. Wallace, and F. Ze, Phys. Rev. Lett. **73**, 2320 (1994).

[94] H. F. Robey, T. R. Boehly, R. E. Olson, A. Nikroo, P. Celliers, O. L. Landen, and D. D. Meyerhofer, Phys. Plasmas **17**, 012703 (2009).

[95] R. J. Trainor, J. W. Shaner, J. M. Auerbach, and N. C. Holmes, Phys. Rev. Lett. **42**, 1154 (1979).

[96] M. D. Landon, J. A. Koch, S. S. Alvarez, P. M. Bell, F. D. Lee, and J. D. Moody, Rev. Sci. Instrum. **72**, 698 (2001).

[97] M. B. Schneider, O. S. Jones, N. B. Meezan, J. L. Milovich, R. P. Town, S. S. Alvarez, R. G. Beeler, D. K. Bradley, J. R. Celeste, S. N. Dixit, M. J. Edwards, M. J. Haugh, D. H. Kalantar, J. L. Kline, G. A. Kyrala, O. L. Landen, B. J. MacGowan, P. Michel, J. D. Moody, S. K. Oberhelman, K. W. Piston, M. J. Pivovaroff, L. J. Suter, A. T. Teruya, C. A. Thomas, S. P. Vernon, A. L. Warrick, K. Widmann, R. D. Wood, and B. K. Young, Rev. Sci. Instrum. **81**, 10E538 (2010).

[98] P. Amendt, A. I. Shestakov, O. L. Landen, D. K. Bradley, S. M. Pollaine, L. J. Suter, and R. E. Turner, Phys. Plasmas **8**, 2908 (2001).

[99] D. C. Wilson, A. J. Scannapieco, C. W. Cranfill, M. R. Clover, N. M. Hoffman, and J. Collins, Phys. Plasmas **10**, 4427 (2003).

[100] R. E. Olson, G. A. Rochau, R. J. Leeper, and O. L. Landen, Phys. Plasmas. **18**, 032706 (2011).

[101] D. C. Wilson, R. L. SingletonJr., J. P. Grondalski, N. M. Hoffman, A. NobileJr., F. H. Séguin, J. A. Frenje, C. K. Li, and R. D. Petrasso, Rev. Sci. Instrum. **77**, 10E711 (2006).

[102] N. D. Delamater, D. C. Wilson, G. A. Kyrala, A. Seifter, N. M. Hoffman, E. Dodd, R. Singleton, V. Glebov, C. Stoeckl, C. K. Li, R. Petrasso, and J. Frenje, Rev. Sci. Instrum. **79**, 10E526 (2008).

[103] J. A. Frenje, C. K. Li, J. R. Rygg, F. H. Séguin, D. T. Casey, R. D. Petrasso, J. Delettrez, V.Yu. Glebov, T. C. Sangster, O. Landen, and S. Hatchett, Phys. Plasmas **16**, 022702 (2009).

[104] D. H. Cohen, J. J. MacFarlane, P. Jaanimagi, O. L. Landen, D. A. Haynes, D. S. Conners, K. L. Penrose, and N. S. Shupe, Phys. Plasmas **11**, 2702 (2004).

[105] B. A. Remington, B. A. Hammel, O. L. Landen, and R. A. Pasha, Rev. Sci. Instrum. **63**, 5083 (1992); B. A. Hammel, D. Griswold, O. L. Landen, T. S. Perry, B, A. Remington, P. L. Miller, T. A. Peyser, and J. D. Kilkenny, Phys. Fluids B **5**, 2259 (1993).

[106] J. A. Frenje, C. K. Li, F. H. Séguin, D. T. Casey, R. D. Petrasso, T. C. Sangster, R. Betti, V. Yu. Glebov, and D. D. Meyerhofer, Phys. Plasmas **16**, 042704 (2009).

[107] J. A. Frenje, C. K. Li, F. H. Seguin, J. Deciantis, S. Kurebayashi, J. R. Rygg, R. D. Petrasso, J. Delettrez, V. Yu. Glebov, C. Stoeckl, F. J. Marshall, D. D. Meyerhofer, T. C. Sangster, V. A. Smalyuk, and J. M. Soures, Phys. Plasmas **11**, 2798 (2004).

[108] V. Yu. Glebov, D. D. Meyerhofer, T. C. Sangster, C. Stoeckl, S. Roberts C. A. Barrera, J. R. Celeste, C. J. Cerjan, L. S. Dauffy, D. C. Eder, R. L. Griffith, S. W. Haan, B. A. Hammel, S. P. Hatchett, N. Izumi, J. R. Kimbrough, J. A. Koch, O. L. Landen, R. A. Lerche, B. J. MacGowan, M. J. Moran, E. W. Ng, T. W. Phillips, P. M. Song, R. Tommasini, B. K. Young, S. E. Caldwell, G. P. Grim, S. C. Evans, J. M. Mack, T. J. Sedillo, M. D. Wilke, D. C. Wilson, C. S. Young, D. Casey, J. A. Frenje, C. K. Li,

R. D. Petrasso, F. H. Séguin, J. L. Bourgade, L. Disdier, M. Houry, I. Lantejoul, O. Landoas, G. A. Chandler, G. W. Cooper, R. J. Leeper, R. E. Olson, C. L. Ruiz, and M. A. Sweeney, S. P. Padalino, C. Horsfield, and B. A. Davis, Rev. Sci. Instrum. **77**, 10E715 (2006).

[109] A. B. Bullock, O. L. Landen, B. E. Blue, J. Edwards, and D. K. Bradley, J. Appl. Phys. **100**, 043301 (2006).

[110] R. E. Olson, M. Geissel, J. W. Kellogg, D. G. Hicks, B. K. Spears, J. P. Holder, O. L. Landen, G. R. Bennett, A. D. Edens, B. W. Atherton, and R. J. Leeper, Rev. Sci. Instrum. **79**, 10E913 (2008).

[111] A. V. Okishev, R. G. Roides, I. A. Begishev, and J. D. Zuegel, Proc. SPIE **6053**, 60530J (2006).

[112] F. Girard, J. P. Jadaud, M. Naudy, B. Villette, D. Babonneau, M. Primout, M. C. Miller, R. L. Kauffman, L. J. Suter, J. Grun, and J. Davis, Phys. Plasmas **12**, 092705 (2005); D. Babonneau, M. Primout, F. Girard, J.-P. Jadaud, M. Naudy, B. Villette, S. Depierreux, C. Blancard, G. Faussurier, K. B. Fournier, L. Suter, R. Kauffman, S. Glenzer, M. C. Miller, J. Grun, and J. Davis, Phys. Plasmas **15**, 092702 (2008).

[113] J. Workman and G. A. Kyrala, Proc. SPIE **4504**, 168 (2001).

[114] H. Huang, A. Nikroo, R. B. Stephens, S. A. Eddinger, D. R. Wall, K. A. Moreno, and H. W. Xu, Fusion Sci. Technol. **55**, 536 (2009).

[115] B. J. Kozioziemski, D. S. Montgomery, J. D. Sater, J. D. Moody, C. Gautier, and J. W. Pipes, Nucl. Fusion **47**, 1 (2007).

[116] P. Michel, L. Divol, E. A. Williams, S. Weber, C. A. Thomas, D. A. Callahan, S. W. Haan, J. D. Salmonson, S. Dixit, D. E. Hinkel, M. J. Edwards, B. J. MacGowan, J. D. Lindl, S. H. Glenzer, and L. J. Suter, Phys. Rev. Lett. **102**, 025004 (2009); P. Michel, L. Divol, E. A. Williams, C. A. Thomas, D. A. Callahan, S. Weber, S. W. Haan, J. D. Salmonson, N. B. Meezan, O. L. Landen, S. Dixit, D. E. Hinkel, M. J. Edwards, B. J. MacGowan, J. D. Lindl, S. H. Glenzer, and L. J. Suter, Phys. Plasmas **16**, 042702 (2009); P. Michel, L. Divol, R. P. J. Town, M. D. Rosen, D. A. Callahan, N. B. Meezan, M. B. Schneider, G. A. Kyrala, J. D. Moody, E. L. Dewald, K. Widmann, E. Bond, J. L. Kline, C. A. Thomas, S. Dixit, E. A. Williams, D. E. Hinkel, R. L. Berger, O. L. Landen, M. J. Edwards, B. J. MacGowan, J. D. Lindl, C. Haynam, L. J. Suter, S. H. Glenzer, and E. Moses, Phys. Rev. E **83**, 046409 (2011).

[117] R. L. Kauffman, L. V. Powers, S. N. Dixit, S. G. Glendinning, S. H. Glenzer, R. K. Kirkwood, O. L. Landen, B. J. MacGowan, J. D. Moody, T. J. Orzechowski, D. M. Pennington, G. F. Stone, L. J. Suter, R. E. Turner, T. L. Weiland, A. L. Richard, and M. A. Blain, Phys. Plasmas **5**, 1927 (1998).

[118] E. L. Dewald, O. S. Jones, O. L. Landen, L. Suter, P. Amendt, R. E. Turner, and S. Regan, Rev. Sci. Instrum. **77**, 10E 310 (2006).

[119] L. J. Suter, A. A. Hauer, L. V. Powers, D. B. Ress, N. Delameter, W. W. Hsing, O. L. Landen, A. R. Thiessen, and R. E. Turner, Phys. Rev. Lett. **73**, 2328 (1994).

[120] O. L. Landen, P. A. Amendt, L. J. Suter, R. E. Turner, S. G. Glendinning, S. W. Haan, S. M. Pollaine, B. A. Hammel, M. Tabak, M. D. Rosen, and J. D. Lindl, Phys. Plasmas **6**, 2137 (1999).

[121] J. Kimbrough, J. D. Moody, P. M. Bell, and O. L. Landen, Rev. Sci. Instrum. **75**, 4060 (2004).

[122] T. J. Murphy, J. M. Wallace, N. D. Delamater, C. W. Barnes, P. Gobby, A. A. Hauer, E. Lindman, G. Magelssen, J. B. Moore, J. A. Oertel, R. Watt, O. L. Landen, P. Amendt, M. Cable, C. Decker, B. A. Hammel, J. A. Koch, L. J. Suter, R. E. Turner, R. J. Wallace, F. J. Marshall, D. Bradley, R. S. Craxton, R. Keck, J. P. Knauer, R. Kremens, and J. D. Schnittman, Phys. Rev. Lett. **81**, 108 (1998).

[123] R. E. Turner, P. Amendt, O. L. Landen, S. G. Glendinning, P. Bell, C. Decker, B. A. Hammel, D. Kalantar, D. Lee, R. Wallace, D. Bradley, M. Cable, R. S. Craxton, R. Kremens, W. Seka, J. Schnittman, K. Thorp, T. J. Murphy, N. Delamater, C. W. Barnes, A. Hauer, G. Magelssen, and J. Wallace, Phys. Plasmas **7**, 333 (2000).

[124] R. E. Turner, P. A. Amendt, O. L. Landen, L. J. Suter, R. J. Wallace, and B. A. Hammel, Phys. Plasmas **10**, 2429 (2003).

[125] P. A. Amendt, R. E. Turner, and O. L. Landen, Phys. Rev. Lett. **89**, 165001 (2002).

[126] G. A. Kyrala, A. Seifter, J. Kline, N. Hoffman, and S. R. Goldman, Bull. Am. Phys. Soc. **53**, 247 (2008).

[127] P. Amendt, C. Cerjan, D. E. Hinkel, J. L. Milovich, H.-S. Park, and H. F. Robey, Phys. Plasmas **15**, 012702 (2008).

[128] G. A. Kyrala, S. Dixit, S. Glenzer, D. Kalantar, D. Bradley, N. Izumi, N. Meezan, O. L. Landen, D. Callahan, S. V. Weber, J. P. Holder, S. Glenn, M. J. Edwards, P. Bell, J. Kimbrough, J. Koch, R. Prasad, L. Suter, J. L. Kline, and J. Kilkenny, Rev. Sci. Instrum. **81**, 10E316 (2010).

[129] K. C. Chen, Y. T. Lee, H. Huang, J. B. Gibson, A. Nikroo, M. A. Johnson, and E. Mapoles, Fusion Sci. Technol. **51**, 593 (2007).

[130]J. Edwards, M. Marinak, T. Dittrich, S. Haan, J. Sanchez, J. Klingmann, and J. Moody, Phys. Plasmas **12**, 056318 (2005); G. R. Bennett, M. C. Herrmann, M. J. Edwards, B. K. Spears, C. A. Back, E. W. Breden, P. J. Christenson, M. E. Cuneo, K. L. Dannenburg, C. Frederick, K. L. Keller, T. D. Mulville, A. Nikroo, K. Peterson, J. L. Porter, C. O. Russell, D. B. Sinars, I. C. Smith, R. M. Stamm, and R. A. Vesey, Phys. Rev. Lett. **99**, 205003 (2007).

[131]P. A. Keiter, J. B. Elliott, B. E. Blue, J. H. Cooley, J. Edwards, G. A. Kyrala, H. F. Robey, B. Spears, and D. C. Wilson, Phys. Plasmas **17**, 062704 (2010).

[132]S. Langer, N. Izumi, T. R. Dittrich, and S. W. Haan, High Energy Density Phys. **3**, 169 (2007).

[133]J. A. Koch, T. W. BarbeeJr., N. Izumi, R. Tommasini, R. C. Mancini, L. A. Welser, and F. J. Marshall, Rev. Sci. Instrum. **76**, 073708 (2005).

[134]S. H. Langer, H. A. Scott, M. M. Marinak, and O. L. Landen, J. Quant. Spectrosc. Radiat. Transf. **71**, 479 (2001).

[135]B. A. Hammel, C. J. Keane, M. D. Cable, D. R. Kania, J. D. Kilkenny, R. W. Lee, and R. Pasha, Phys. Rev. Lett. **70**, 1263 (1993).

[136]E. L. Dewald, C. Thomas, S. Hunter, L. Divol, N. Meezan, S. H. Glenzer, L. J. Suter, E. Bond, J. Kline, J. Celeste, R. L. Kauffman, J. Kilkenny, and O. L. Landen, Rev. Sci. Instrum. **81**, 10D938 (2010).

[137]C. A. Thomas, Phys. Rev. E **81**, 036413 (2010).

[138]S. P. Regan, N. B. Meezan, L. J. Suter, D. J. Strozzi, W. L. Kruer, D. Meeker, S. H. Glenzer, W. Seka, C. Stoeckl, V. Yu. Glebov, T. C. Sangster, D. D. Meyerhofer, R. L. McCrory, E. A. Williams, O. S. Jones, D. A. Callahan, M. D. Rosen, O. L. Landen, C. Sorce, and B. J. MacGowan, Phys. Plasmas **17**, 020703 (2010).

[139]A. Simon, R. W. Short, E. A. Williams, and T. Dewandre, Phys. Fluids **26**, 3107 (1983).

[140]H.-S. Park, E. D. Dewald, S. Glenzer, D. H. Kalantar, J. D. Kilkenny, B. J. MacGowan, B. R. Maddox, J. L. Milovich, R. R. Prasad, B. A. Remington, H. F. Robey, and C. A. Thomas, Rev. Sci. Instrum. **81**, 10E 519 (2010).

[141]B. R. Maddox, H.-S. Park, B. A. Remington, N. Izumi, S. Chen, C. Chen, G. Kimminau, Z. A. Ali, M. J. Haugh, and Q. Ma, Rev. Sci. Instrum. **82**, 023111 (2011).

[142]H. Sawada, S. P. Regan, D. D. Meyerhofer, I. V. Igumenshchev, V. N. Goncharov, T. R. Boehly, R. Epstein, T. C. Sangster, V. A. Smalyuk, B. Yaakobi, G. Gregori, S. H. Glenzer, and O. L. Landen, Phys. Plasmas **14**, 122703 (2007); A. L. Kritcher, P. Neumayer, J. Castor, T. Döppner, R. W. Falcone, O. L. Landen, H. J. Lee, R. W. Lee, E. C. Morse, A. Ng, S. Pollaine, D. Price, S. H. Glenzer, Science **322**, 69 (2008); H. J. Lee, P. Neumayer, J. Castor, T. Döppner, R. W. Falcone, C. Fortmann, B. A. Hammel, A. L. Kritcher, O. L. Landen, R. W. Lee, D. D. Meyerhofer, D. H. Munro, R. Redmer, S. P. Regan, S. Weber, and S. H. Glenzer, Phys. Rev. Lett. **102**, 115001 (2009).

[143]A. Kritcher, T. Doeppner, H. J. Lee, P. Davis, O. Landen, and S. Glenzer, Bull. Am. Phys. Soc. **54**, 354 (2009); A. L. Kritcher, T. Doeppner, C. Fortmann, O. L. Landen, R. Wallace, and S. H. Glenzer, "Development of x-ray Thomson scattering for implosion target characterization," High Energy Density Phys. (accepted); A. L. Kritcher, T. Doeppner, C. Fortmann, T. Ma, O. L. Landen, R. Wallace, and S. H. Glenzer, "In-flight measurements of capsule shell adiabats in laser driven implosions," Phys. Rev. Lett. (submitted).

[144]G. R. Bennett, D. B. Sinars, D. F. Wenger, M. E. Cuneo, R. G. Adams, W. J. Barnard, D. E. Beutler, R. A. Burr, D. V. Campbell, L. D. Claus, J. S. Foresi, D. W. Johnson, K. L. Keller, C. Lackey, G. T. Leifeste, L. A. McPherson, T. D. Mulville, K. A. Neely, P. K. Rambo, D. C. Rovang, L. E. Ruggles, J. L. Porter, W. W. Simpson, I. C. Smith, and C. S. Speas, Rev. Sci. Instrum. **77**, 10E322 (2006).

[145]J. A. Koch, O. L. Landen, B. J. Kozioziemski, N. Izumi, E. L. Dewald, J. D. Salmonson, and B. A. Hammel, J. Appl. Phys. **105**, 1 (2009).